

# **Design and Optimization of High-Speed Silicon Linear Optical Modulators**

**LO, Ming Gai Stanley**

A Thesis Submitted in Partial Fulfillment  
of the Requirements for the Degree of  
Master of Philosophy  
in  
Electronic Engineering

The Chinese University of Hong Kong

August 2011



**Abstract of the thesis entitled:**

**Design and Optimization of High-Speed Silicon Linear Optical Modulators**

**Submitted by Lo Ming Gai Stanley**

**for the degree of Master of Philosophy**

**at The Chinese University of Hong Kong in July, 2011**

Silicon photonics refers to the discipline of applying microelectronics integrated circuit fabrication technologies to make silicon-based photonic integrated circuits on a silicon-based material platform. Silicon photonic integrated circuits are fabricated using complementary metal-oxide-semiconductor (CMOS)-like fabrication processes and have potential for integration with silicon-based electronic devices. Because of these advantages, silicon photonics provides a promising approach for a number of applications including active optical cables, signal processing, distribution of radio-frequency signals over optical fibers and optical transceivers for optical telecommunications.

Optical modulators are a crucial element for optical communications. They transfer the electrical signal to the optical carrier. Although recent publications have been reported with silicon-based optical modulators operating as fast as 40 Gb/s, this remains a scope to optimize the modulator performance in terms of its linearity, footprint, electrical bandwidth and extinction ratio.

In this thesis, silicon modulators using free-carrier plasma dispersion effect are described. The design, fabrication and characterization of the silicon modulators are

carried out. Optical structure of Mach-Zehnder interferometer (MZI) based, microring resonators and microring resonator-coupled MZI based are investigated. Both modulation mechanisms of carrier injection-based on p-i-n diodes and carrier depletion-based on p-n diodes are implemented to the devices. In order to investigate the potential applications of silicon modulators in radio-over-fiber optical links, the linearity of the depletion-based silicon modulators was analyzed. An experiment of signal transmission in analog optical links by a silicon modulator is described. In order to improve the modulation efficiency, insertion loss and fabrication tolerance, a novel vertical-junction p-n diode design is proposed and fabricated. In order to enhance the electrical bandwidth and extinction ratio of the modulator, the T-rail capacitance loaded travelling-wave electrode design is described.



## 摘要

矽光子學是指應用微電子集成電路製造技術，使用矽作為光子集成電路為基礎平台的一門學科。矽光子集成電路採用金屬氧化物半導體製造工藝制以矽為集成基礎的光電子器件。由於種種成本上的優勢，矽光子學能有效解決現時電子電路上的互連問題。

電光調製器是光波通訊中不可或缺的重要元件。它的作用是將電信號調制到光載波上。儘管現時矽基電光調製器運行速度已展示到 40 Gb/s，矽基電光調製器的性能仍有其優化空間，例如線性度，集成密度，帶寬和消光比。

在這篇論文中，我們對使用自由載流子等離子體色散效應的矽調製器進行了詳細的闡述。我們設計，製造和測試了不同的矽調製器。其光學結構包括馬赫 - 曾德爾干涉儀，微環諧振器和微環諧振器耦合馬赫 - 曾德爾干涉儀進行了深入的研究。兩種主要的調節機制包括把載流子注入到 PIN 二極管和把載流子從 PN 二極管中耗盡。而為了深入研究矽調製器在模擬光鏈路上的潛在應用，我們亦對矽調製器的線性度進行了全面的分析。同時我們亦進行了由矽光調製器生成類比信號的實驗。為了進一步改善矽基電光調製器的調製效率，插入損耗和工藝容限，我們設計並製造了一種新型的垂直 PN 結二極管。最後，為了提高帶寬和消光比的調製器，我們對 T 型導軌電容加載行波電極的設計加以說明。

## Acknowledgements

First and foremost, I would like to express my appreciation to my supervisor Professor Hon-Ki Tsang for his continuing guidance, help and encouragement. During the years of my graduate studies, Professor Tsang's insights and knowledge on silicon photonics eventually help my research project to success.

I like to say thank you to Dr. Chao Li, for his guidance and encouragement during the time I work with him in CUHK. I entirely appreciate that I can work with Dr. Li and the opportunity to acquire so many of techniques and knowledge from him.

Thanks for the short term visit opportunity given by Professor Chi-Wai Chow from National Chiao Tung University in Taiwan.

I also like to thank my colleagues: Dr. Xia Chen, Dr. Lin Xu, Mr. Chris Wong, Miss Christy Fung, Mr. Zhen-Zhou Cheng, Mr. Ke Xu, Mr. Yi-Min Chen, Ms. Barbara Ho and Mr. Gordon Lei. The friendly and inspiring research environment in the optoelectronic group in CUHK provides me a great opportunity to perform research during these years.

Thanks for the helps from all the staffs in MNF/CUHK and NFF/HKUST in helping me during the fabrication process of the photonic devices.

Furthermore, thanks are given to Professor Kam-Tai Chan, Professor Lian-Kuan Chen and Professor Chester Shu for their advice and suggestion on my research. I thank Professor Andrew Poon for being my external examiner.

Finally, I have to thank my family, grandma, mum, dad, June and Rita for their support and love for last two years. Especially for Rita, I certainly know that I

cannot be as strength as now without your encouragements, thank you so much for your love and patience.

Title Page	1
Abstract	ii
Acknowledgements	7
Table of Contents	10
List of Figures	34
List of Table	40
Chapter 1: Introduction	1
1.1 Optical Communication Systems	1
1.2 System Description	2
1.3 Optical Modulators	10
1.4 Acousto-optic Modulators in Silicon	17
1.5 SAW Devices	27
1.6 Surface Acoustic Wave	28
Chapter 2: Use of Silicon-based Modulators in Radio-over-Fiber Optical Links	29
2.1 Modeling of Capacity of Silicon-based Depletion-based Modulators	31
2.2 Application of Depletion-based Modulators in Various Optical Structures	43
2.2.1 Application of Radio-over-Fiber and Transposition to a Carrier Frequency	43
2.2.2 Silicon-based Modulators	44
2.2.3 Silicon-based Modulators	44
2.3 Summary	44
Chapter 3: Novel Radio Modulators and Traveling-Wave Structures to Enhance the Performance of Frequency-based Modulators	50
3.1 Requirements of Traveling-Wave Depletion-based Optical Modulators	50
3.2 Mode Design Example	52
3.3 Modeling Results of Traveling-Wave Depletion-based Modulators	59

# Table of Contents

Title Page .....	i
Abstract.....	ii
Acknowledgements .....	v
Table of Contents .....	vii
List of Figures.....	ix
List of Table.....	xiv
<b>Chapter 1: Introduction .....</b>	<b>1</b>
1.1 Photonic Integrated Circuits.....	1
1.2 Silicon Photonics.....	7
1.3 Optical Modulators.....	15
1.4 Modulation Mechanisms in Silicon .....	19
1.5 Motivation .....	27
1.6 Thesis Outline .....	28
<b>Chapter 2: Use of Silicon-based Modulators in Radio-over-fiber Optical Links</b>	<b>29</b>
2.1 Modeling of Linearity of Silicon Carrier Depletion-based Modulators.....	31
2.2 Modeling of Dependence of Linearity on Various Diode Structures.....	45
2.3 Experiment of Radio-over-Fiber Signal Transmission by a Carrier-Injection Silicon Microring Modulator .....	52
2.3.1 Device Fabrication.....	53
2.3.2 Experimental Setups .....	59
2.3.3 Experimental Results .....	61
2.4 Summary .....	66
<b>Chapter 3: Novel Diode Structures and T-Rail Travelling-Wave Electrodes to Enhance the Performance of Depletion-based Modulators .....</b>	<b>67</b>
3.1 Requirements of Diode Design for Depletion-based Optical Modulators .....	70
3.2 Diode Design Principle .....	72
3.3 Modeling Results of Vertical-Junction p-n Diodes.....	79



3.4 Fabrication Process of the Silicon Modulator .....	88
3.5 Experimental Results of the Fabricated Devices.....	92
3.6 T-Rail Travelling-Wave Electrodes .....	102
3.6.1 <i>The Limiting Factors to the Speed of Depletion-based Modulators</i> .....	102
3.6.2 <i>The Design Principle of T-Rail Travelling-Wave Electrodes</i> .....	104
3.6.3 <i>The Fabricated Devices</i> .....	111
3.7 Summary .....	112
<b>Chapter 4: Conclusion and Future Work.....</b>	<b>113</b>
4.1 Conclusion.....	113
4.1.1 <i>Use of Silicon-based Modulators in Radio-over-fiber Optical Links</i> .....	113
4.1.2 <i>Novel Diode Structures and T-Rail Travelling-Wave Electrodes to Enhance the Performance of Depletion-based Modulators</i> .....	114
4.2 Future Work .....	116
<b>Appendix-A List of Symbols .....</b>	<b>118</b>
<b>Appendix-B List of Abbreviations.....</b>	<b>120</b>
<b>Appendix-C Principles of Various Optical Structures of Modulators.....</b>	<b>123</b>
<b>Appendix-D Modeling of Refractive Index Change by Free-Carrier Plasma Dispersion Effect .....</b>	<b>127</b>
<b>Reference .....</b>	<b>131</b>
<b>Publication List .....</b>	<b>136</b>

## List of Figures

- 1.1.1 A tunable optical transmitter integrated in a hybrid polymer optical bench platform
- 1.1.2 Historical trend and timeline for monolithic, photonic integration on InP [3]. The vertical axis represents the number of photonic components to be integrated.
- 1.2.1 Silicon-based optoelectronic IC (OEIC) “superchip” proposed by Soref in 1993 [12]
- 1.2.2 Overview of Luxtera’s silicon PIC fabricated by CMOS-compatible processes [16]
- 1.2.3 Summary of advantages and limitations in silicon photonics
- 1.3.1 Schematic of the operation of an optical modulator
- 1.4.1 Schematic diagram showing the cross-sectional view of a MOS capacitor waveguide phase shifter using ‘silicon-on-insulator’ technology. The n-type doped crystalline silicon layer thickness is  $\sim 1.4\ \mu\text{m}$ , and the p-type doped polysilicon thickness at the centre of waveguide is  $\sim 0.9\ \mu\text{m}$ . The gate oxide thickness is  $120\ \text{\AA}$ . The polysilicon rib and the gate oxide widths are both  $\sim 2.5\ \mu\text{m}$ . The n-type silicon has an active doping concentration of  $\sim 1.7 \times 10^{16}\ \text{cm}^{-3}$  and the p-type poly-silicon has an active doping concentration of  $\sim 3 \times 10^{16}\ \text{cm}^{-3}$ . These doping concentrations were chosen to produce a modulation speed of the phase shifter of above 1 GHz, as the speed of the device depends on silicon and polysilicon resistance. A surface doping density of  $1 \times 10^{19}\ \text{cm}^{-3}$  was designed to minimize the metal-semiconductor contact resistance.
- 1.4.2 Schematic layout of the ring resonator-based modulator. The inset shows the cross-section of the ring. R, radius of ring.  $V_F$ , voltage applied on the modulator.
- 1.4.3 Cross-sectional view of a pn junction waveguide phase shifter in silicon-on-insulator. The coplanar waveguide electrode has a signal metal width of  $\sim 6\ \mu\text{m}$  and a signal-ground metal separation of  $\sim 3\ \mu\text{m}$ . The metal thickness is  $\sim 1.5\ \mu\text{m}$ . The high-frequency characteristic impedance of the travelling wave electrode is  $\sim 20\ \Omega$ .
- 2.1.1 (top) Cross-sectional schematic of the waveguide and the TE optical mode field distribution. (down) Cross-sectional schematic of the p-i-p-i-n diode
- 2.1.2 Calculated effective refractive index and absorption coefficient changes as a function of drive reverse bias voltage.
- 2.1.3 Schematics of the configurations of ring(s)-assisted MZI and conventional MZI-based modulator structures.
- 2.1.4 Calculated transfer functions of the LEO-based modulator employ MZI and ring(s)-

assisted MZI optical structures at a voltage bias of 2.5V.

- 2.1.5 Calculated RF output signal power and 3<sup>rd</sup> IMD power of LEO based modulators as a function of RF input signal power.
- 2.1.6 Calculated transfer functions of the silicon depletion-based modulators MZI and ring(s)-assisted MZI at a voltage bias of 2.5V.
- 2.1.7 Calculated RF output signal power and 3<sup>rd</sup> IMD power of both LEO- and silicon-based MZI modulator as a function of RF input signal power. The modulators are reverse-bias at 2.5V. From the simulation results, the SFDR of Silicon based MZI have 4.6 dB improvement than LEO based MZI.
- 2.1.8 Calculated RF output signal power and 3<sup>rd</sup> IMD power of silicon-based MZI and 2RAMZI modulator as a function of RF input signal power. The modulators are reverse biased at 7.5V.
- 2.1.9 Calculated SFDR of the silicon based MZI and 2RAMZI with various bias voltages.
- 2.2.1 (top) Cross-sectional schematic of the waveguide and TE mode field distribution (down) Cross-sectional schematic of the  $p^+-p(i)-n-n^+$  diode
- 2.2.2 Calculated effective refractive index changes as a function of drive voltage for diode designs A-G. Inset shows the plot of square of refractive index changes as a function of drive voltage, the refractive index change responses behave a square-root-like dependence of drive voltage.
- 2.2.3 Calculated absorption coefficient changes as a function of drive voltage for diode design A-G.
- 2.2.4 Calculated SFDRs of diode design A-G at various bias voltages
- 2.3.1 Schematic of the fabrication process flow for silicon modulator based on carrier-injection in a microring resonator structure.
- 2.3.2 (a) Cross sectional schematic of the optical waveguide, the simulated optical transverse-electric (TE) mode field distribution and the schematic of the embedded  $p^+-i-n^+$  diode. (b) Top-view microscope image of the fabricated silicon carrier injection-based modulator. Inset: zoom-in microscope image of the ring resonator (c) Cross sectional scanning electronic microscope (SEM) image of our fabricated optical waveguide on SOI. The upper oxide cladding is removed by BOE.



- 2.3.3 Experimental setup in the testing of ROF signal transmission by using a silicon microring modulator. We employ LR signal testing of (1) B2B (0km), (2) 50km and (3) 100km long SMF.
- 2.3.4 Photograph of the optical coupling setup by grating couplers used in the experiment.
- 2.3.5 Measured IV characteristic of the fabricated silicon microring modulator embedded with a  $p^+-i-n^+$  diode
- 2.3.6 Measured transmission spectra of the silicon microring modulator under various forward bias DC voltages
- 2.3.7 Measured  $2^7-1$  PRBS at 1 Gbps NRZ BER measurement of the output signal for B2B, 50km and 100km SMF transmissions. Insets: corresponding eye diagrams for B2B, 50km and 100km SMF.
- 2.3.8 Measured wavelength spectrum of the SSB-ROF signal
- 3.2.1 (a) Calculated refractive index changes of free-holes and free-electrons. Inset: the ratio of  $\Delta n_h / \Delta n_e$  (b) Calculated loss coefficient changes of free holes and free electrons, with unit of (dB/mm)
- 3.2.2 Calculated depletion widths as a function of doping concentrations
- 3.2.3 (a) Cross-sectional schematic of the optical waveguide and optical-TE mode field distribution. (b) Cross-sectional schematic of the horizontal junction p-n diode in the waveguide. (c-e) Cross-sectional schematics of the dimensions of depletion width inside an optical waveguide with various doping concentrations. The doping concentrations are  $N_A, N_D = 5 \times 10^{17} / \text{cm}^3$ ,  $N_A, N_D = 1 \times 10^{18} / \text{cm}^3$  and  $N_A, N_D = 2 \times 10^{18} / \text{cm}^3$ . The calculated depletion width under 5V reverse-bias are 180 nm, 125 nm and 90 nm. (f-h) Lateral-direction TE-mode field profiles of the waveguide in the core region at 110 nm high above the oxide cladding and the depletion width.
- 3.2.4 (a) Cross-sectional schematic of the vertical-junction p-n diode in the waveguide. (b) Cross-sectional schematics of the dimension of depletion region inside the optical waveguide.  $N_A, N_D = 1 \times 10^{18} / \text{cm}^3$ . (c) Vertical direction TE mode field profile at the center of the waveguide
- 3.3.1 Simulated doping profiles of the (a) horizontal-junction and (b) vertical-junction p-n diodes embedded into the optical waveguide. The profiles are simulated by Athena.
- 3.3.2 (a) Calculated effective refractive index changes and (b) absorption coefficient changes for the horizontal junction and vertical-junction p-n diodes.

- 3.3.3 Cross-sectional schematics of the ion implantation windows for (a) p-doping and (b) n-doping. The center of the waveguide is defined as  $X = 2.00 \mu\text{m}$ . The doping windows are  $0.15 \mu\text{m}$  apart from the center. The center of edge of p-doping window on the waveguide is defined as  $X = 1.85 \mu\text{m}$ . The center of edge of n-doping window on the waveguide is defined as  $X = 2.15 \mu\text{m}$ .
- 3.3.4 Calculated  $V_{\pi}L$  as a function of (a) p- and (b) n- doping window variations.
- 3.3.5 (a) Cross-sectional schematic of an optical waveguide on SOI substrates and the corresponding calculated TE-mode field profile. The waveguide is 340 nm high, 500 nm wide with a 140 nm thick slab. (b-c) Simulated (b) hole and (c) electron concentration changes in the waveguide core region upon 5 V reverse bias in a 340 nm high waveguide.
- 3.4.1 Schematics of the fabrication process flow for the silicon depletion-based modulator embedded with a vertical junction  $p^+ - p - n - n^+$  diode.
- 3.5.1 Top-view microscope image of the fabricated silicon depletion-based modulator with an asymmetric MZI structure on SOI.
- 3.5.2 (a) Cross-sectional SEM image of the fabricated waveguide. (b) Cross-sectional SEM image of the fabricated diode embedded waveguide.
- 3.5.3 Measured IV characteristic of the fabricated silicon depletion-based modulator embedded with a  $p^+ - p - n - n^+$  diode
- 3.5.4 Measured transmission spectrum of the diode-embedded AMZI with 1.5 mm phase shifter in waveguide with height of 340 nm without applied DC voltage (0V).
- 3.5.5 Measured transmission spectra of the fabricated depletion-based modulator embedded with a  $p^+ - p - n - n^+$  diode in waveguide with height of 340 nm under various forward bias DC voltages.
- 3.5.6 Measured transmission spectra of the fabricated depletion-based modulator embedded with a  $p^+ - p - n - n^+$  diode in waveguide with height of 340 nm under various reverse-bias DC voltages.
- 3.5.7 Measured transmission spectra of the fabricated depletion-based modulator embedded with a  $p^+ - p - n - n^+$  diode in waveguide with height of 220 nm under various reverse-bias DC voltages.
- 3.6.1 Schematic of the limiting factors on the speed of depletion-based modulators.
- 3.6.2 Top-view schematic of the T-rail TWE design

- 3.6.3 (a) Top-view schematic of the unloaded CPS.  $W$  is the width of the strips,  $S$  is the gap separation between the two strips. (b) Cross-sectional schematic of the unloaded CPS.  $H$  is the height of the substrate,  $T$  is the height of metal strips,  $\epsilon_r$  is the relative permittivity of the substrate. (c) Cross-sectional schematic of the E-field distribution of the CPS. (d) Equivalent transmission line circuit model of the unloaded CPS.
- 3.6.4 Calculated characteristic impedance as a function of the gap separation of CPS by the empirical relation. The substrate is assumed to be silicon with 525  $\mu\text{m}$  thick. The strip widths are set to be 120  $\mu\text{m}$ .
- 3.6.5 Calculated required  $l_{\text{eff}}$  to achieve group velocity and impedance matching as a function of microwave index with various diode capacitance
- 3.6.6 Top-view microscope image of the fabricated T-rail TWE on SOI
- C.1 Schematics of Mach-Zehnder interferometer (MZI), Fabry-Perot (FP) resonator and ring resonator.
- C.2 Schematics of the operation principle of resonator based modulators. In the Fabry-Perot resonator, refractive index inside the resonant cavity has been decrease, leads to a blue shift of resonance spectrum. In the ring resonator, refractive index inside the ring cavity has been increase, leads to a red shift of resonance spectrum.  $\lambda_r$  is the resonant wavelength,  $\lambda_{r2}$  is the resonant wavelength under modulation.
- D.1 Schematic of flow chart of the methodology in simulation the refractive index changes in free carrier effect based silicon modulator. The 2D array profile of free carrier distributions is obtained by Athena and Atlas. The 2D array profile of optical mode field is obtained by BeamPROB. The final refractive index and loss coefficient changes under modulation are calculated by finite element method in MATLAB. Atlas also provides the small signal characteristics of the electrical structures.

## List of Table

- 1.1 Comparison between photonic and microelectronic industry
- 1.2 Summary on materials of various discrete photonic devices
- 1.3 Comparison among various PIC material platforms
- 1.4 Comparison between various costs of semiconductor wafers
- 1.5 Comparison among SOI and III-V semiconductor PIC platform
- 1.6 Comparison between the direct modulation of laser sources and external modulation
- 1.7 State-of-the-art of silicon modulators based on plasma effect
- 1.8 State-of-the-art of optical modulators on silicon other than free-carrier effect
- 2.1 Simulation parameters of various silicon depletion-based modulator designs
- 2.2 Calculation results of the required modulator length, insertion loss due to the free-carrier absorption and SFDR at bias voltage of 2.5 V of various silicon depletion-based modulator designs



## Chapter 1: Introduction

### 1.1 Photonic Integrated Circuits

Photonic integrated circuit (PIC) is a device that integrates multiple photonic functions, which is analogous to an electronic integrated circuit (IC) in microelectronic industry. The major difference between a PIC and an electronic IC is that a PIC provides functionality on optical signals rather than electrical signals in an electronic IC. PIC integrates various discrete optical devices such as the lasers, amplifiers, photodetectors, optical modulators, optical filters etc., while electronic IC primary integrates millions to billions of transistors in a tiny chip. Table 1.1 shows the technology comparison between photonic (including PIC) and microelectronic industry.

Table 1.1 Comparison between photonic and microelectronic industry

	Photonic components	Electronic IC
Repeatable building blocks	None (laser, photodetector, modulator, filter, etc.)	Transistors
Dominant material platforms	None (InP, GaAs, polymer, Si, etc.)	Silicon
Dominant manufacturing processes	None (Hybrid, monolithic, active, passive, etc.)	CMOS <sup>†</sup>

<sup>†</sup>complementary metal-oxide-semiconductor

In current photonic industry, a variety of materials have been employed in each commercial discrete device: indium phosphide (InP) as a substrate for the lasers emitting in 1550 nm, lithium niobate (LiNbO<sub>3</sub>) for optical modulators, silica for

optical fiber, silica-on-silicon for passive devices etc. Table 1.2 shows the summary on materials of different discrete photonic devices.

Table 1.2 Summary on materials of various discrete photonic devices

	Lasers	Detectors	Modulators	Amplifiers	Passive devices
III-V semiconductors	Dominant	Dominant	Available	Dominant	Available
Lithium niobate			Dominant		Available
Polymers			Available		Available
Silica-on-silicon					Available
Erbium-doped materials	Available			Dominant	Available

From table 1.2, most of the materials used in commercial discrete photonic devices are not compatible to achieve other functionalities. For example, lithium niobate is superb for making optical modulators, however, it is not capable for making the lasers. On the other hand, even the III-V semiconductors fulfill all the required functions, the fabrication processes of making different components are different, and it results in big challenges of integration. Due to these limitations, the development of PIC over the last 20 years was relatively slow compare with electronic IC industry. So it is commonly accepted that the development and implementation of photonics will be strongly enhanced if the industrial model of electronic IC can be applied to PIC [1], as microelectronic industry already has a dominant material platform and standardized fabrication process.

Figure 1.1.1 shows the schematics of a PIC on a polymer platform by hybrid integration [2]. This tunable optical transmitter contains at least seven different materials for different functions include the laser, an external tunable cavity, an

isolator and a modulator. This polymer-based PIC was fabricated by a hybrid fabrication process. Although it provided a lower fabrication cost and better functionality than discrete components, a PIC fabricated by monolithic process would provide even better functionality and lower cost.

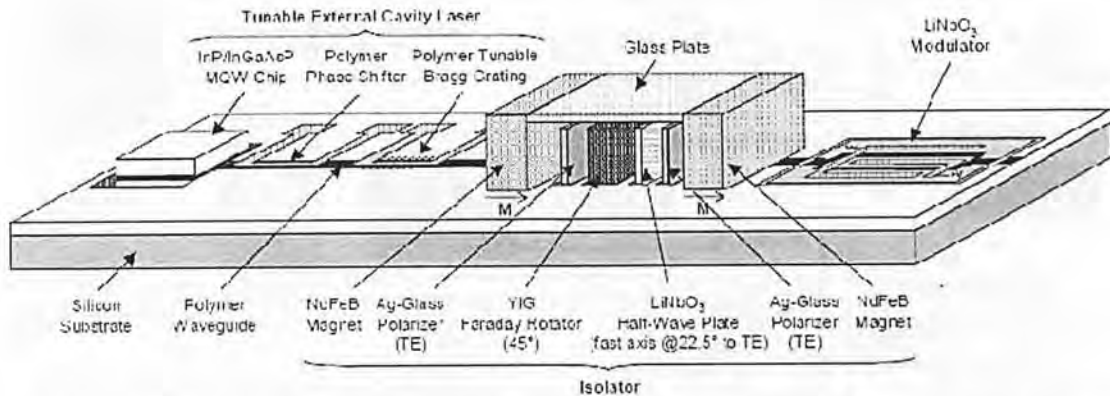


Fig. 1.1.1 A tunable optical transmitter integrated in a hybrid polymer optical bench platform [2]

In the early 2000s some convergence appeared to use InP as the substrate material for monolithic PIC. Figure 1.1.2 shows the historical trend and timeline for monolithic, photonic integration on InP [3]. The PIC on InP started in 1980s, with the integration of electronic devices with laser diodes and photodetectors as so-called optoelectronic ICs (OEICs). The famous three-section tunable distributed Bragg reflector (DBR) laser were introduced in late 1980s. Later on the electroabsorption modulator (EAM) integrated to a distributed feedback (DFB) laser was also demonstrated. More components started to be integrated into the InP-based PIC including the semiconductor optical amplifier (SOA) and arrayed waveguide grating (AWG). Recently [3], the research team in University of California, Santa Barbara (UCSB) reported an  $8 \times 8$  monolithic tunable router with about 200 components in one PIC chip. It is no doubt that InP-based PIC platform is an ideal candidate for telecommunications usage in 1.3-1.6  $\mu\text{m}$  wavelength. However, it has certain



limitations, which not only limit the development of PICs, but also become a roadblock of photonic industry.

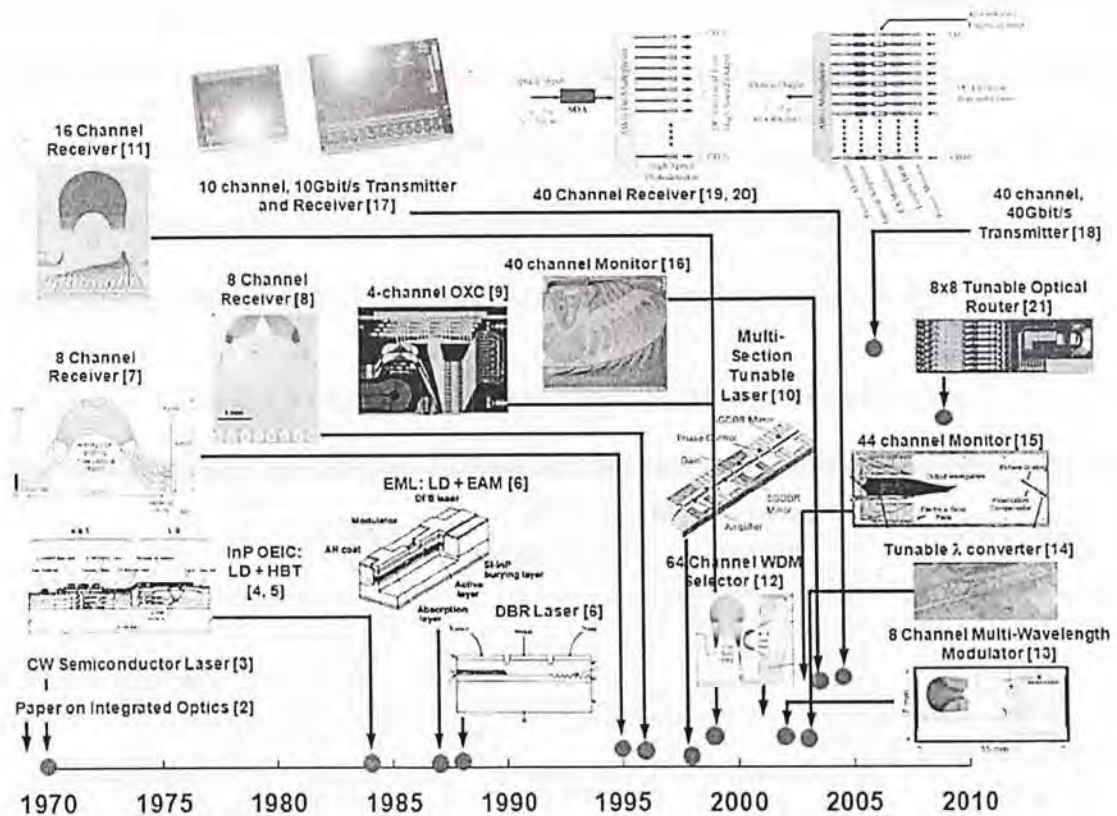


Fig. 1.1.2 Historical trend and timeline for monolithic, photonic integration on InP [3]. The vertical axis represents the number of photonic components to be integrated.

Other material platforms such as silica have also been widely used as different photonic functional devices such as AWG for wavelength division multiplexing (WDM) applications. Since 2000 [1], another material platform – silicon-on-insulator (SOI) has attracted lots of attention on its potential as a substrate for PIC because of low cost and high-density integration. The details on PIC developed on SOI and related research field, called silicon photonics, will be discussed in section 1.2.

Unlike in electronic IC, where silicon is a dominant material accounting for over 95% of the whole market of semiconductor chips [1], today's PICs use a variety of materials such as silica (on silicon substrates), III-V-based semiconductor materials

such as gallium arsenide (GaAs) and indium phosphide (InP), polymers, lithium niobate and SOI. Different materials have different advantages and limitations on the functions to be integrated. For example, the InP platform enable monolithic integration of the lasers, modulators, photodetectors and other passive components. However, the relatively high fabrication cost limits the potential usage of these devices in telecommunications and computer interconnect regime. Table 1.3 lists the comparison among various PIC material platforms (modified from [4]).

Table 1.3 Comparison among various PIC material platforms

	Cost	CMOS-compatible	Integration density	Primary Usage
III-V semiconductors	High	No	High	Integrated WDM transceiver
Silica-on-silicon	Low	Yes	Low	Passive devices (e.g. AWG)
Polymers	Low	No	Low	Modulators and hybrid integration platforms
Lithium niobate	Extremely High	No	Low	High speed modulators (for advanced formats)
Silicon-on-insulator (SOI)	Low	Yes	High	Low-cost optical interconnects

InP-based PICs dominant today's market in high-end optical communications systems. However, there are suggestions [1, 5-7] that photonics can be further employed in computing systems as interconnects to solve the existing signal latency problems in microelectronic industry. The scale of optical interconnects decrease from rack-to-rack, computer-to-computer, board-to-board (inside computer), chip-to-chip and finally on-chip interconnects. When the scale of optical interconnect

decreases, the number of required interconnects exponentially increases. Therefore, cost becomes a primary concern in interconnect applications. The secondary concern is the compatibility with existing electronic platform if the on-chip interconnects is to be achieved.

For the first concern, InP based PIC does not fulfill as the wafer and fabrication costs are inevitably high. For the second concern, as mentioned above, silicon dominates the microelectronic industry of over 95% of the whole market. Although III-V semiconductors are compatible for electronic device integration in PICs, to integrate with existing electronic ICs is still a big challenge. To solve these problems and to achieve an eventual success of on-chip interconnects, recent research pay more attention on silicon-based PIC. The related field – silicon photonics, is not only aiming to provide functional devices for communications system, but also the potential as optical interconnects. The history and current research progress of silicon photonics are discussed in next section.



## 1.2 Silicon Photonics

Although the field of integrated optics (the technology used in PIC) has been established in 1969 [8], the proposed use of silicon as a photonic material platform for telecommunications wavelengths in 1.3-1.6  $\mu\text{m}$  started 16 years later by Soref in 1985 [9-10]. During that time, silicon has already dominated microelectronic industry. Silicon based photonics devices like charged-coupled device (CCD) image sensors were commercially available too. The reasons of why silicon cannot be the photonic material in telecommunications wavelengths were due to three basic physical limitations:

- 1) silicon is an indirect-bandgap semiconductor thus lacks of efficient light sources
- 2) silicon has a bandgap of 1.12 eV thus it does not detect light in telecommunications wavelengths
- 3) silicon is a centro-symmetric crystal thus it does not exhibit linear electro-optic (Pockels) effect

For the first point, indirect bandgap of silicon indicates that the radiative recombination of electrons and holes across the bandgap is weak, resulting in extremely low internal quantum efficiency in bulk silicon ( $10^{-6}$ ). Consequently, silicon lacks of efficient LEDs or electrically pumped lasers. It has been a serious deficiency of using silicon as a PIC platform since, without light sources, a complete suite of photonic components is not available for monolithic on-chip integration.

To discuss the second point, the fact that silicon is transparent above 1.1  $\mu\text{m}$  is like a paradox. Because silicon is transparent in telecommunications wavelengths (1.3-1.6  $\mu\text{m}$ ) means that silicon can be used as low-loss optical waveguides. The

major difference of silicon compared with InP platform is that InP-based PIC has capability of bandgap engineering by changing the composition of III-V alloys. Silicon-based platform does not have this capability so it does not provide the functions of wave-guiding and detection on the same wafer.

For the third point, silicon does not exhibit Pockels effect – a traditional means of achieving modulation of refractive index in a waveguide-based device. It prohibits the usage of silicon as an electro-optical modulator. Although thermal tuning in silicon is available, the speed is limited to 1MHz [6] so it is not suitable for high-speed modulation. Silicon needs another way to achieve refractive index modulation in order to provide functions on high-speed active tuning.

Because of the above reasons, the research effort in photonic devices on silicon was only modest after the initial work of Soref. There were work on the passive components, photodetectors by complementary metal-oxide-semiconductor (CMOS) compatible materials and modulators by carrier effect in silicon [11] (details will be discussed in section 1.4).

Besides the deficiency of using silicon as a photonic material in telecommunications wavelengths, silicon has several major advantages which include the mature fabrication technology on silicon by the microelectronic industry (CMOS fabrication process started to dominate in 1990s) and availability of making low-loss passive devices.

Optoelectronic IC (OEIC) to integrate the electronic and photonic components in the same platform becomes a huge advantage of silicon. As silicon already dominates the microelectronic industry, the development of photonic devices in silicon could enhance both the performance and cost efficiently by the concept of

OEIC. Figure 1.2.1 shows the related concept, a silicon-based OEIC “superchip” proposed by Soref in 1993 [12].

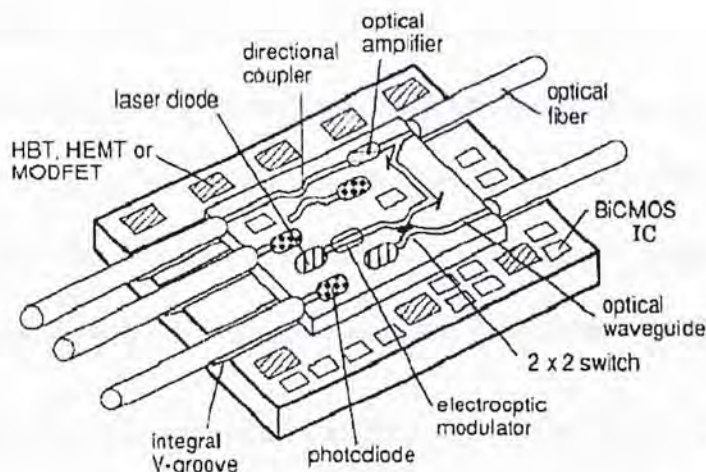


Fig. 1.2.1 Silicon-based optoelectronic IC (OEIC) “superchip” proposed by Soref in 1993 [12]

In year 2000, the manufacturing technologies of SOI became mature. A commercially available high-quality SOI wafers for photonic usage provide another advantages for silicon photonics – high integration density. This becomes a catalyst of research in silicon-based photonic devices.

Consequently, the research on photonic devices on silicon increased rapidly after year 2000. The explosion of research efforts led to a stand-alone research field – silicon photonics. The driving force of silicon photonics at that time was mainly by the development of high-volume OEIC and commercial PICs in SOI platform. The field is still full of momentum today and many of the fundamental physical limitations in silicon have been solved by tremendous research efforts over the past 20 years.

In order to provide a light source on silicon PIC, integrating a III-V semiconductor laser to the silicon PIC chip by hybrid fabrication method is one of the promising solutions [14]. Although the hybrid method may potentially lead to higher complexity and fabrication costs, the integration of III-V semiconductor lasers to



silicon PIC is still a good approach to realize a complete suite of PIC in silicon in current circumstances.

It is feasible for the silicon PIC to detect the light signal in 1.3-1.6  $\mu\text{m}$  by using an integrated germanium (Ge) or silicon-germanium (SiGe) photodetector [15]. The advantage of using Ge or SiGe is fully compatible with CMOS process. The state-of-the-art performance of Ge photodetector modules on silicon substrates is largely compatible with III-V semiconductor-based photodetectors [6].

The refractive index of silicon can be modulated by adding or subtracting the number of free-carriers. The corresponding effect – free-carrier plasma dispersion effect [11] becomes a major modulation mechanism in silicon. By optimizing the electrical and photonic structures, one can attain above 10 Gb/s modulation by all-silicon-based optical modulators [16].

Figure 1.2.2 shows the overview of Luxtera's silicon PIC in 2005 [16]. The PIC was fabricated by a CMOS-compatible fabrication process for the all-silicon modulators, Ge photodetectors, passive photonic devices and electronic circuits. A light source was made by flip-chip bonding techniques of III-V semiconductor lasers emitting in 1.55  $\mu\text{m}$ . This silicon PIC consequently was re-packaged as active optical cables to provide low-cost optical interconnects in computing centers and data centers.



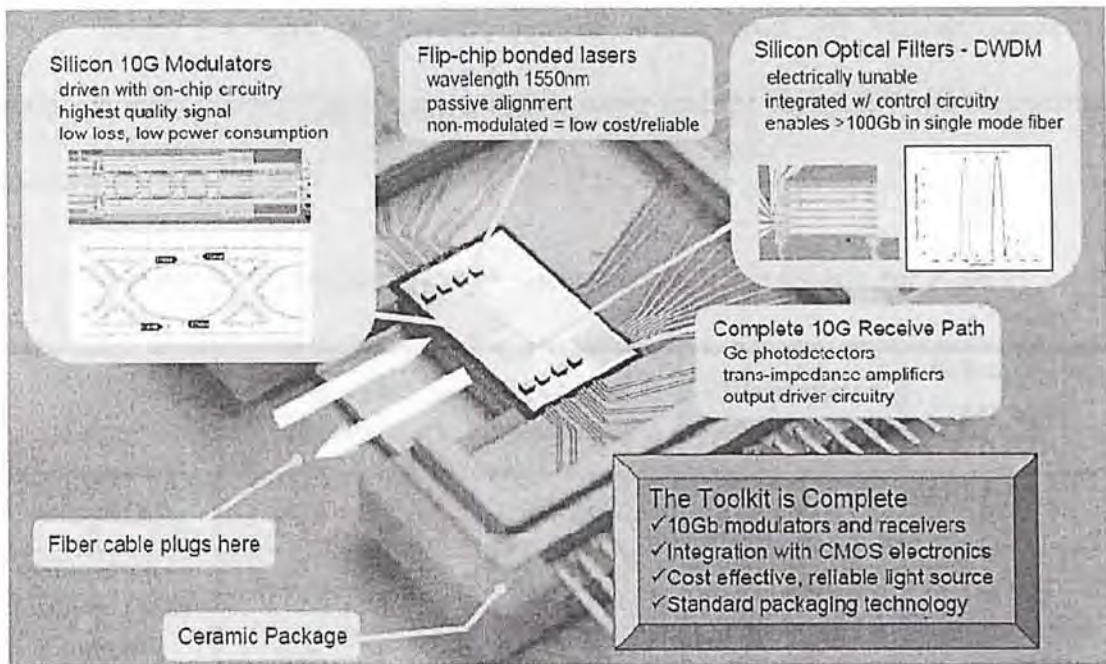


Fig. 1.2.2 Overview of Luxtera's silicon PIC in 2005 [16]

As cost is a big advantage of silicon photonics against III-V semiconductor based photonics, in the followings detailed descriptions of manufacturing cost will be discussed.

The manufacturing costs of PIC are determined by three factors: (a) the cost of substrate per area, (b) the cost of fabrication processes on the substrate per area and (c) the integration densities of the functional PIC chips. Thus, the total manufacturing cost per each functional PIC chip can be represented as:  $\text{total cost} = ((a) + (b)) \times (c)$ . We need to minimize the substrate and fabrication costs and maximize the integration densities of the devices layout in order to get the minimum costs of the PIC chips.

However, the cost of substrates is determined by the commercial market. It is well-known that silicon wafers is much cheaper than III-V semiconductor wafers as the microelectronic industry is dominant by silicon.

Table 1.4 lists the comparison of wafer costs of various kinds of semiconductor wafers. The largest available wafer sizes in both R&D and commercial markets are also listed.

Table 1.4 Comparison between various costs of semiconductor wafers

	Wafer sizes (R&D)	Wafer sizes (commercial)	Wafer costs (USD)	Substrate costs per 1mm <sup>2</sup> (USD)
Silicon (Si)	450 mm	300 mm	150	0.0015
Silicon-on-insulator (SOI)	450 mm [17]	300 mm	1200	0.012
Indium phosphide (InP)	150 mm	100 mm	450	0.045
Gallium arsenide (GaAs)	200 mm	150 mm	450	0.02

The substrate cost per area for SOI wafers is half of GaAs wafers and one-third of InP wafers. In addition, the fabrication cost in SOI is also cheaper than in III-V by the mature CMOS fabrication process and well-developed facilities. For point (c), in order to maximize the integration density, the primary limitation is on the refractive index of core and cladding of optical waveguides. Fundamental waveguide principle shows that the higher refractive index difference between the core and cladding ( $\Delta n$ ) would enable higher confinement of optical mode in the core region, finally enables smaller size of optical waveguides and smaller bending radius. The smaller size and bending radius allow a higher integration density, thus the integration density of a PIC is accessed by the ratio of  $\Delta n/n$ .

Table 1.5 shows the comparison among SOI and III-V semiconductor including InP and GaAs [2].



Table 1.5 Comparison among SOI and III-V semiconductor PIC platform

	Wavelength ( $\mu\text{m}$ )	Refractive index $n$	Band gap	$\Delta n/n$ (%)	T/O coef. $dn/dT$ ( $\text{K}^{-1}$ )
Silicon-on-insulator (SOI)	1.1	3.5	Indirect	60	$1.86 \times 10^{-4}$
Indium phosphide (InP)	1.55	3.1	Direct	0-3	$0.8 \times 10^{-4}$
Gallium arsenide (GaAs)	0.8	3.4	Direct	0-14	$2.5 \times 10^{-4}$

Due to the large refractive index difference between Si (3.5) and the cladding silicon dioxide  $\text{SiO}_2$  (1.5), the  $\Delta n/n$  of the SOI PIC platform can be as high as 60%, which is significantly higher than in InP (3% (channel)) and GaAs (14% (rib)). Today's single-mode optical waveguides in SOI platform has a typical dimension of 500 nm width and 220 nm height. This sub-micron 'nanowire' waveguide provides ultrahigh integration density compared with III-V semiconductors.

From the above analysis, SOI platform provides all the cost advantages than III-V semiconductor platforms in substrate costs, fabrication costs and integration density. The cost advantages of SOI platform is thus a great advantage of silicon photonics to accomplish the goals of optical interconnects.

Finally, figure 1.2.3 summarizes the advantages, physical properties, disadvantages, and related solutions in the field of silicon photonics.

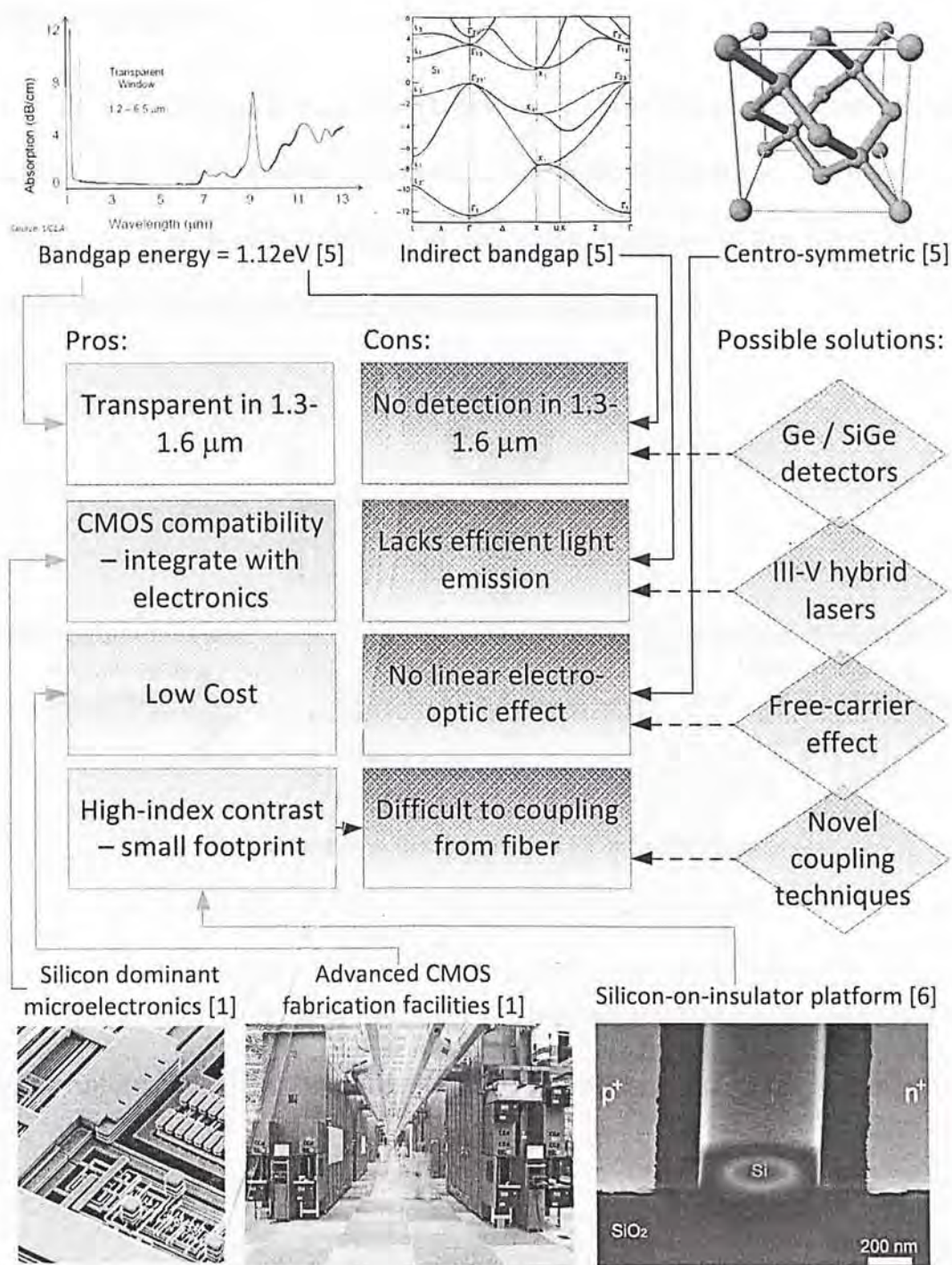


Fig. 1.2.3 Summary of advantages and limitations in silicon photonics.

### 1.3 Optical Modulators

The optical modulator is a crucial element for optical interconnects and optical communications. Optical modulators are used to transfer the electrical information to the optical wave propagating either in an optical waveguide or in free space. Figure 1.3.1 shows the schematic of the operation of an optical modulator.

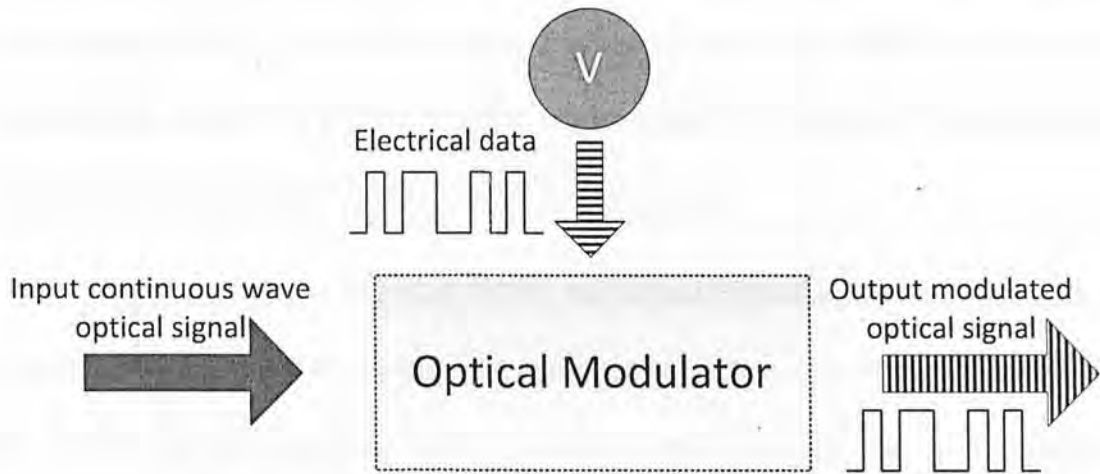


Fig. 1.3.1 Schematic of the operation of an optical modulator

Optical wave has various fundamental characteristics that can be modulated to carry the information. Equation 1.3.1 shows the general expression of an optical wave:

$$E = Ae^{j(\omega t - \beta z)} \quad (1.3.1)$$

where  $E$  is the electric field,  $A$  is the amplitude,  $\omega$  is the angular frequency,  $t$  is time,  $\beta$  is the propagation constant and  $z$  is the distance in the travelling direction of the wave.

From equation 1.3.1, the amplitude  $A$ , frequency  $\omega$  and phase term  $(\omega t - \beta z)$  can be modulated to vary the characteristics of the wave. Hence, the related modulation schemes are called amplitude modulation (AM), frequency modulation (FM) and phase modulation (PM). In digital communications, they correspond to



amplitude shift keying (ASK), frequency shift keying (FSK) and phase shift keying (PSK). Due to the advantage of simplicity of envelope photodetection in the receiver side, amplitude modulation (on-off keying (OOK)) has been widely employed in optical communications systems. Recently, the use of phase modulation has started in optical communications. The variant format – differential phase shift keying (DPSK) [18] in optical communications provides an advantage of 3dB lower optical signal-to-noise ratio (OSNR) than OOK to reach a given bit-error ratio (BER). An external modulator is needed in DPSK or other phase modulation schemes because direct modulation of laser source cannot achieve such function.

Optical carrier can be either directly modulated in the laser diode or externally modulated by an optical modulator. Direct modulation scheme has been deployed into the system in the beginning age of optical communication due to its simple architecture and modest bandwidth requirement at that time. But the increasing demands on the modulation bandwidth and signal performance finally lead to the use of external optical modulator in today's long-haul optical communications networks.

The major advantages of external modulation over direct modulation includes: (1) higher electrical bandwidth (speed), (2) larger extinction ratio and (3) better signal performance (low chirp).

However, a special type of laser diodes – vertical-cavity surface-emitting laser (VCSEL), which enables low fabrication cost, has been used in the short range optical networks. It is possibly because commercial optical modulators are targeted for long-haul usage and are relatively expensive. But once the costs on optical modulators can be scaled down (for example, by silicon photonics), the use of external modulators has additional advantages over VCSELs. First, the optical source can be more

inexpensive and stable than VCSELs due to the looser requirement on high-speed modulation. Second, a single WDM light source can be used as an input light source modulated by several modulators on a single chip, resulting in an increase of total bandwidth.

Table 1.6 gives the comparison between direct modulation of laser sources and external modulation.

Table 1.6 Comparison between the direct modulation of laser sources and external modulation

	Direct modulation	External modulation
System complexity	Simple and compact	Complex with addition component
Cost	Low	High
Modulation speed	< 20 Gb/s (VCSEL) [19]	> 100 Gb/s [20]
Extinction ratio	Low	High
Signal performance	High chirp	Low chirp (in push-pull configuration of a MZI modulator)
Comments:	Optical sources become more expensive if high-speed VCSELs are used in the system	Feasible of phase modulation (for advanced modulation formats)

Today, optical modulators become an essential and crucial element in the whole communications system as it determines the highest speed supported by each single channel (single wavelength). For example, in a dense wavelength-division multiplexing (DWDM) system with 40 channels, an improvement on speed of optical modulators from 10 Gb/s to 40Gb/s will finally increase the total bandwidth to 1.6



Tb/s in a single fiber. This explains the importance of high-performance of optical modulators in the development of optical communications networks.

Beside the application in optical communications systems, optical modulators also play a key role in the optical interconnects applications. In addition to providing high data-rate interconnections, optical modulators are also feasible to provide on-chip clock signal distribution.

From table 1.2, there are several materials that are capable for making modulators. Lithium niobate, EO polymers and III-V semiconductors based optical modulators have an electrical bandwidth of over 40GHz and are commercially available. However, the modulation mechanisms used in silicon modulators is different from all of the mentioned materials above. The detailed discussion on silicon modulators will be shown on next section.

#### 1.4 Modulation Mechanisms in Silicon

As discussed in section 1.2, it is commonly accepted that silicon does not provide Pockels effect due to its centro-symmetric lattice structure. We first give the general modulation mechanisms, then introduce the current mechanism that has been used in silicon.

There are two broad categories of modulation – electro-refraction and electro absorption. The change in the real part of the refractive index ( $n$ ) with an applied electric field is known as electro-refraction. Similarly, the change in the imaginary part ( $k$ ) of the refractive index with an applied electric field is considered as electro-absorption. It is well-known that the real and imaginary part of the refractive index are related by the Kramers-Kronig dispersion relations [21].

The electro-refraction based modulations are mainly based on Pockels effect and Kerr effect. Pockels effect is a second-order optical nonlinear effect, the refractive index changes linearly with the applied electric field. It also called linear electro-optic (LEO) effect. Kerr effect is a third-order optical nonlinear effect, where the change of refractive index is directly proportional to the square of the applied electric field.

The electro-absorption-based modulations are mainly based on Franz-Keldysh effect and quantum-confined Stark effect (QCSE) [22]. Franz-Keldysh effect occurs in bulk semiconductors. QCSE occurs in thin quantum-well structures ( $\sim 10$  nm). Both effects shift and broaden the band-edge absorption of the semiconductor under the applied electric field.

In order to study the electro-optical effects in silicon, Soref in 1987 did a numerical Kramers-Kronig analysis to predict the refractive-index changes produced

in crystalline silicon by the applied electric field or by charge carriers [11]. The analysis shows that for the electro-refraction caused by Franz-Keldysh effect, an applied electric field of  $10^5$  V/cm results in a refractive index change ( $\Delta n$ ) of  $1.3 \times 10^{-5}$  at wavelength of  $1.07 \mu\text{m}$ . On the same field strength ( $E=10^5$  V/cm), the Kerr effect gives  $\Delta n$  of  $10^{-6}$ . The results indicate that bulk crystalline silicon does not exhibit the major electro-optic effects we mentioned above (QCSE only for quantum well structures). However, silicon as a semiconductor exhibits an additional electro-optic effect – free-carrier plasma dispersion effect. An effect caused by injecting or depleting free carriers into the semiconductor. Soref's analysis showed that a depletion or injection of  $10^{18}$  carriers/ $\text{cm}^3$  produce a  $\Delta n$  of  $\pm 1.5 \times 10^{-3}$  at wavelength of  $1.3 \mu\text{m}$  and  $\Delta n$  of  $\pm 2.1 \times 10^{-3}$  at wavelength of  $1.55 \mu\text{m}$ .

Soref calculated the refractive index changes by free-carrier plasma dispersion effect from the Kramers-Kronig relation [23]. The empirical relations of changes of refractive index ( $\Delta n$ ) and absorption coefficient ( $\Delta \alpha$ ) in silicon at wavelength of  $1.55 \mu\text{m}$  are shown as follows:

$$\Delta n = \Delta n_e + \Delta n_h = -8.8 \times 10^{-22} \times \Delta N_e - 8.5 \times 10^{-18} \times (\Delta N_h)^{0.8} \quad (1.4.1)$$

$$\Delta \alpha = \Delta \alpha_e + \Delta \alpha_h = 8.5 \times 10^{-18} \times \Delta N_e + 6.0 \times 10^{-18} \times \Delta N_h \quad (1.4.2)$$

where  $\Delta N_e$  is the free-electron concentration,  $\Delta N_h$  is the free-hole concentration,  $\Delta n_e$  is the change of refractive index resulting from the change of free-electron concentration,  $\Delta n_h$  is the change of refractive index resulting from the change of free-hole concentration,  $\Delta \alpha_e$  is the change of absorption coefficient (with unit of /cm) resulting from change of free electron concentration,  $\Delta \alpha_h$  is the change of absorption coefficient resulting from the change of free-hole concentration.

To theoretically describe the free-carrier plasma dispersion effect in semiconductor, the Drude model has been used, which regards the free-charge-carriers as harmonic oscillators [68]. The formula for free-carriers-induced refraction and absorption change are [68]:

$$\Delta n = -(e^2 \lambda^2 / 8 \pi^2 c^2 \epsilon_0 n) [\Delta N_e / m_{ce}^* + \Delta N_h / m_{ch}^*] \quad (1.4.3)$$

$$\Delta \alpha = (e^2 \lambda^2 / 4 \pi^2 c^2 \epsilon_0 n) [\Delta N_e / m_{ce}^* \mu_e + \Delta N_h / m_{ch}^* \mu_h] \quad (1.4.4)$$

where  $e$  is the electronic charge,  $\epsilon_0$  is the permittivity of free space,  $n$  is the refractive index,  $m_{ce}^*$  is the conductivity effective mass of electrons,  $m_{ch}^*$  is the conductivity effective mass of holes,  $\mu_e$  is the electron mobility and  $\mu_h$  is the hole mobility.

From Soref's analysis carrier effect is the most efficient electro-optic effect in silicon. Free-carrier effect becomes a major stream on the research of silicon modulator for more than two decades until now. However, the first breakthrough of silicon modulators was only published in 2004 by A. Liu from Intel Corporation [24]. A. Liu et al. experimentally demonstrated the first GHz-speed silicon modulator. They used an electrical structure of metal-oxide-semiconductor (MOS) capacitor to achieve the free carrier effect by carrier accumulation around the waveguide core region. The optical structure of the device is based on Mach-Zehnder interferometer (MZI). The cross sectional schematic of their device is depicted in Figure. 1.4.1 [24].



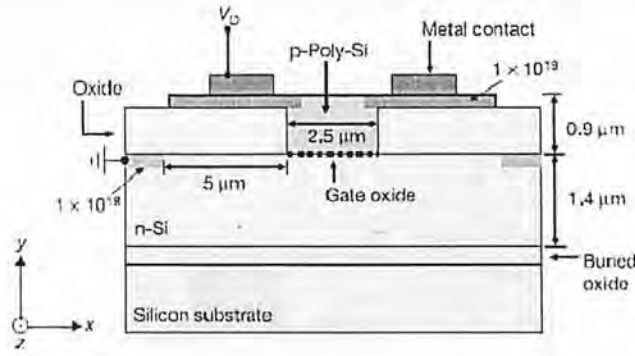


Fig. 1.4.1 Schematic diagram showing the cross-sectional view of a MOS capacitor waveguide phase shifter using ‘silicon-on-insulator’ technology. The n-type doped crystalline silicon layer thickness is  $\sim 1.4 \mu\text{m}$ , and the p-type doped polysilicon thickness at the centre of waveguide is  $\sim 0.9 \mu\text{m}$ . The gate oxide thickness is  $120 \text{ \AA}$ . The polysilicon rib and the gate oxide widths are both  $\sim 2.5 \mu\text{m}$ . The n-type silicon has an active doping concentration of  $\sim 1.7 \times 10^{16} \text{ cm}^{-3}$  and the p-type poly-silicon has an active doping concentration of  $\sim 3 \times 10^{16} \text{ cm}^{-3}$ . These doping concentrations were chosen to produce a modulation speed of the phase shifter of above 1 GHz, as the speed of the device depends on silicon and polysilicon resistance. A surface doping density of  $1 \times 10^{19} \text{ cm}^{-3}$  was designed to minimize the metal-semiconductor contact resistance. [24]

The second breakthrough on silicon modulators is a GHz-speed ring resonator by Q. Xu et al. from Cornell University [25]. Q. Xu et al. experimentally demonstrated a micrometer-scale silicon modulator by a resonator-based optical structure. They used an electrical structure of p-i-n diode to achieve the free-carrier effect by carrier-injection into the waveguide core region. The optical structure of the device is based on a microring resonator. The modulation thus obtained by shifting the high-Q resonance wavelengths under the applied electric field. The top-view and cross sectional schematics of the device are depicted in figure. 1.4.2 [25]. This work demonstrated the feasibility of ultra-small-footprint optical modulators on silicon,

which arouses the desire of on-chip interconnects. In 2007, Q. Xu et al. increased the modulation speed of similar structure to 12.5 Gb/s by using a pre-emphasis circuit [26].

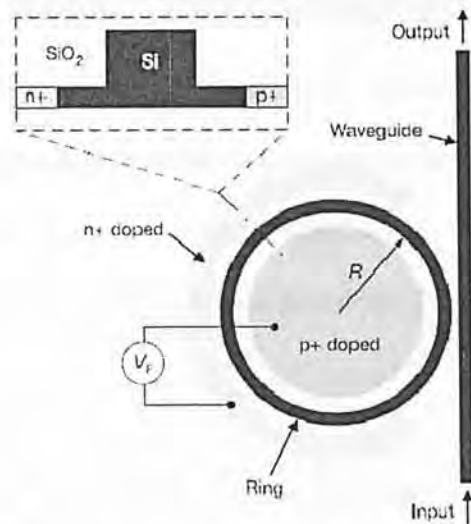


Fig. 1.4.2 Schematic layout of the ring resonator-based modulator. The inset shows the cross-section of the ring.  $R$ , radius of ring.  $V_F$ , voltage applied on the modulator. [25]

The third milestone of research on free-carrier-effect-based silicon modulators was a 30 Gb/s carrier-depletion-based modulator demonstrated by A. Liu et al. from Intel Corporation [27]. A. Liu et al. experimentally demonstrated the first 30 Gb/s silicon modulator due to the intrinsic fast carrier response in the reverse-bias of a p-n diode. They used the electrical structure of a p-n junction to achieve the free-carrier effect by depleting the free-carriers inside the core of waveguide under reverse-bias voltage. A travelling-wave electrode (TWE) design is used to enhance the bandwidth of the modulator. The 3-dB roll off bandwidth is 20 GHz while the digital data transmission can be up to 30 Gb/s. The cross sectional schematic is depicted in figure 1.4.3 [27]. Further improvement on a similar design by Intel showed a 40 Gb/s data transmission later [28].

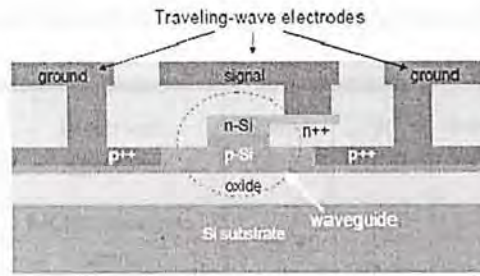


Fig. 1.4.3 Cross-sectional view of a pn junction waveguide phase shifter in silicon-on-insulator. The coplanar waveguide electrode has a signal metal width of  $\sim 6 \mu\text{m}$  and a signal-ground metal separation of  $\sim 3 \mu\text{m}$ . The metal thickness is  $\sim 1.5 \mu\text{m}$ . The high-frequency characteristic impedance of the travelling wave electrode is  $\sim 20\Omega$ . [27]

During the last few years, researches on carrier-effect-based silicon modulators continue. Various structures have been proposed and demonstrated to optimize the figure of merits. However, the fundamental operation principles of these devices are similar to those demonstrated by A Liu et al. and Q. Xu et al.'s work mentioned above. Table 1.7 lists a summary on the experimental demonstrations of free-carrier-effect-based silicon modulators since 2004.

Table 1.7 State-of-the-art of silicon modulators based on plasma effect

	Optical structure	Electrical structure	Speed (Gb/s)	ER <sup>†</sup> (dB)	Insertion loss (dB)	V <sub>π</sub> L (Vcm) / Footprint	Optical BW*
A. Liu et al. [24] (2004)	MZI	MOS capacitor, carrier accumulation	1	16 (DC)	15.3	8 Vcm	-
Q. Xu et al. [25] (2005)	Microring resonator	pin diode, carrier injection	1.5	15 (DC)	0.5	10 <sup>2</sup> μm <sup>2</sup>	0.1 nm
C. Gunn [16] (2005)	MZI	pn diode, carrier depletion	10	5	-	-	-
L. Zhou et al. [66] (2006)	Microdisk resonator	pin diode, carrier injection	0.5 GHz	7 (DC)	23	-	-
A. Liu et al. [27] (2007)	MZI	pn diode, carrier depletion	30	1	5.4	4 Vcm	> 75 nm
W. Green et al. [29] (2007)	MZI	pin diode, carrier injection with pre-emphasis	10	10 (DC)	12	0.036 Vcm	-
Q. Xu et al. [26] (2007)	Microring resonator	pin diode, carrier injection with pre-emphasis	12.5	9	0.5	10 <sup>2</sup> μm <sup>2</sup>	0.1 nm
S. Spector et al. [30] (2008)	MZI	pn diode, carrier depletion	10	-	-	5.3 Vcm	-
D. Marris-Morini et al. [31] (2008)	MZI	pipin diode, carrier depletion	10	14 (DC)	5	5 Vcm	> 30 nm
M. Watts et al. [32] (2008)	Microdisk resonator	pn diode, carrier depletion	10	8 (DC)	1.5	20 μm <sup>2</sup>	0.1 nm
P. Dong et al. [33] (2009)	Microring resonator	pn diode, carrier depletion	10	8	2	10 <sup>2</sup> μm <sup>2</sup>	0.1 nm
D.D'Andrea et al. [34] (2009)	MZI	MOS capacitor, carrier accumulation	10 (up to 40)	9	-	0.2 Vcm	-
M. Watts et al. [35] (2010)	MZI	pn diode, carrier depletion	10	> 10 (DC)	6.2	1 Vcm	> 50 nm

<sup>†</sup>extinction ratio; \*band width;



Several modulation mechanisms other than free-carrier effect have been developed in silicon photonics in recent years including the QCSE effect in SiGe/Si multiple quantum wells (MQWs) [36], Franz-Keldysh effect in SiGe [37] and by hybrid III-V electro-optic effect [38, 39]. Table 1.8 lists the summary on the state of the art of optical modulators on silicon other than free-carrier effect.

Table 1.8 State-of-the-art of optical modulators on silicon other than free-carrier effect

	Optical structure	Modulation Mechanism	Speed (Gb/s)	ER <sup>†</sup> (dB)	Insertion loss (dB)	V <sub>π</sub> L (Vcm) / Footprint	Optical BW*
J. Roth et al [40] (2007) <sup>†</sup>	EAM	QCSE in SiGe/Si MQW	-	7.3	-	-	20 nm for ER > 3 dB
J. Liu et al [37] (2007)	EAM	Franz-Keldysh effect in SiGe	1.2 GHz	10	14.8	-	14 nm
H. Chen et al [38] (2011)	MZI	EO effect in hybrid InP	40	11.4	3	0.24 Vcm	> 100 nm
Y. Tang et al [39] (2011)	EAM	EA effect in hybrid InP	50	9.8	3	10 <sup>5</sup> μm <sup>2</sup>	30 nm

<sup>†</sup>Non-waveguide based device, operate at 1.46 μm; <sup>†</sup>extinction ration; \*band width;

Compared to these modulation mechanisms, silicon modulators based on free-carrier effect provide advantages of simple fabrication processes, wavelength insensitivity and fully CMOS-compatibility.

### 1.5 Motivation

The first part of our work is to investigate the possible uses of silicon-based modulators in the analog optical links. Silicon photonics provide the advantages of low cost and CMOS-compatible of silicon-based PIC. Also, the performance of state-of-the-art silicon based modulators (as shown in table 1.7) is capable in commercial use with moderate requirements. The silicon-based modulators thus have potential in analog optical systems, in which the photonic component cost is the roadblock for system upgrade. However, in analog optical links, an additional figure-of-merit becomes important – linearity. Because of that we need to first analyze the linearity of silicon-based modulator, which has not been reported before. We focus on depletion-type modulators as it gives the optimal balance between simple fabrication process and high-speed among available modulation mechanisms. We describe modeling on various optical structures and diode structures. We also demonstrate an experiment on data transmission in an analog optical link using the silicon-based modulator.

The second part of our work is aimed at optimizing the design of silicon depletion-based modulators in order to solve the existing engineering problems. There are two sections in the modulator design crucial to the performance – (1) diode design and (2) electrode design. The novel diode designs could improve the modulation efficiency, insertion loss and fabrication tolerance of the modulator. The travelling wave electrode (TWE) design could cancel the resistance-capacitance (RC) time limit of the modulator and achieve the velocity matching. TWE design is aimed at maximizing the speed of the modulator as speed of modulator is limited by RC time limit rather than the carrier transit time limit. We describe detailed design principles of diode and electrode designs. Finally, we describe a device fabrication and experiment.

## 1.6 Thesis Outline

The thesis is organized as follows: Chapter 2 presents the study on linearity of silicon depletion-based modulators. We study the linearity of various optical and diode structures. We also experimentally demonstrate a radio-over-fiber (ROF) signal transmission by using a silicon injection based ring modulator. Chapter 3 presents the design, fabrication and characterization of a novel diode structure on a carrier depletion-based silicon modulator. The proposed design simultaneously provides high fabrication tolerance, high modulation efficiency and low loss. Chapter 3 also presents the design principle of the T-rail capacitance loaded travelling-wave electrode. The travelling wave electrode provides the function of characteristic impedance matching and group velocities matching. Therefore, a higher electrical bandwidth can be achieved. Chapter 4 concludes the thesis and suggests the continuing work in the near future.

## **Chapter 2: Use of Silicon-based Modulators in Radio-over-fiber**

### **Optical Links**

We introduce the advantages of silicon photonics over conventional PIC platform in the introduction chapter. The low-cost and CMOS-compatible silicon-based PIC platform already enable applications in optical interconnects and optical communications. Except those applications, we envision the silicon-based PICs are also of interest in analog optical signal transmission.

Radio-over-fiber (ROF) is a type of analog optical links. It offers the advantages of simpler maintenance, lower operational costs and smaller size than by distributing the radio signals via optical fibers to remote antenna units (RAU). It is used for multiple purposes such as cable television (CATV) signal distribution and antenna remoting [41].

A key component for high-performance transparent ROF systems is the optical modulator. In addition to the conventional figure-of-merits of modulators such as speed, extinction ratio and insertion loss, modulators used in ROF system should also provide good linearity. There are previous work on linear optical modulators for ROF including two-stage Mach-Zehnder Interferometer (MZI) [42], linearized directional couplers [43], combination of MZI and directional couplers [44] and ring resonator(s)-assisted MZIs [45,46]. However, these structures used the materials with linear electro-optic effect (LEO) and the analyses are not applicable to silicon-based modulators which are based on free-carrier effect as refractive index is changed non-linearly with the applied voltage in free-carrier effect.



Although silicon MZI-based modulators have been proposed for analog optical links [30], the linearity of silicon-based modulators have not been analyzed yet (at the time we started our work). So in order to investigate the possible applications of silicon modulators in analog optical links, we are required to first analyze its linearity. We focus on depletion-type modulators since which give the advantages on simple fabrication process and high-speed operation compared to other modulation mechanisms.

In this chapter we present the study on linearity of silicon depletion-based modulators and experimental demonstration of the analog optical signal transmission through silicon modulators. Section 2.1 studies the linearity on various optical structures of carrier depletion-based silicon modulators. Section 2.2 presents the studies of linearity on various diode structures of carrier depletion-based silicon modulators. Section 2.3 describes the experiment of ROF signal transmission by silicon injection-based ring modulators. Finally, section 2.4 summarizes the chapter.

## 2.1 Modeling of Linearity of Silicon Carrier Depletion-based Modulators

In this section, the linearity of carrier depletion-based modulators on various optical structures is analyzed. We consider several types of modulator designs including conventional MZI and ring(s)-assisted MZI while the diode structure is assumed to be the same in these structures. The wavelength of operation is assumed to be 1.55  $\mu\text{m}$  in this section.

The silicon depletion-based modulator considered in this section is based on a lateral  $p^+ - i - p - i - n^+$  diode structure under reverse bias operation for free-holes depletion modulation [31]. We choose  $p^+ - i - p - i - n^+$  diode instead of  $p^+ - i - n - i - n^+$  diode because the refractive index changed by free-holes is larger than that of free-electrons for the same carrier concentration change below  $8 \times 10^{19} \text{ cm}^{-3}$  (equation 1.4.1). Also, the absorption loss due to free-holes is lower than that due to free-electrons (equation 1.4.2). In our design the fabrication process is simpler than normally four ion implantation steps are reduced into two steps.

Figure 2.1.1 shows the cross-sectional schematics of the optical waveguide, numerically simulated optical transverse-electric (TE) mode (electric field polarized parallel to the substrate) field distribution (by beam-propagation method) and  $p^+ - i - p - i - n^+$  diode. The waveguide is formed on a 220 nm thick silicon-on-insulator (SOI) wafer. The waveguide is 220 nm high and 500 nm wide with a slab region of 50 nm thick for the  $p^+$  and  $n^+$  doping to form the metal contacts. The  $p^+$  and  $n^+$  doped regions are separated from the waveguide sidewalls with a spacing of around 0.5  $\mu\text{m}$ . The carrier concentrations for the  $n^+$  and  $p^+$  slab regions are  $2 \times 10^{20} \text{ cm}^{-3}$  and  $1 \times 10^{19} \text{ cm}^{-3}$ . The waveguide region has a Gaussian-distribution doping profile with a peak  $p$ -doping concentration of around  $4 \times 10^{18} \text{ cm}^{-3}$ . The proposed modulator structures are

designed to be fabricated by the overseas shared-wafer foundry service at LETI, France through ePIXfab [47]. By considering the fabrication constrain given by the design rules from LETI, the p-doping width of 120 nm is employed in order to achieve a moderate p-doping concentration and low absorption loss. In order to achieve the largest effective refractive index change, the p-doping region is positioned towards the p<sup>+</sup> slab region with a displacement of 180 nm from the waveguide center so that the free-holes' depletion could overlap the most effectively with the optical mode filed distribution.

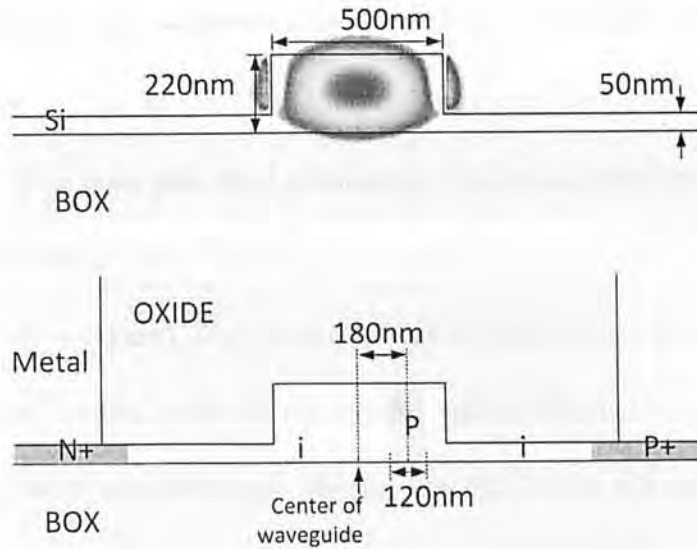


Fig. 2.1.1 (top) Cross-sectional schematic of the waveguide and the TE optical mode field distribution. (down) Cross-sectional schematic of the p<sup>+</sup>-i-p-i-n<sup>+</sup> diode

The application of a reverse-bias will remove holes from the p-doped region inside the waveguide. By using the commercial semiconductor simulation software and combining the free-carrier effect and mode distribution, we are able to find out the effective index changes and absorption coefficient changes upon various biases. Various diode parameters such as doping concentration and position of p-doped region have been optimized to give the balance between modulation efficiency and

loss. The detailed methodology of simulation is described in Appendix D.

Figure 2.1.2 shows the calculated effective refractive index changes and absorption coefficient changes. Effective refractive index describes the phase velocity of the light travelling in waveguide and is analogous to refractive index  $n$  in a material. At 5V reverse-bias, the refractive index change  $\Delta n$  is around  $1.5 \times 10^{-4}$ . Thus a 5.2 mm long phase shifter is required to achieve  $\pi$  phase change in one arm drive MZI. This corresponds to a  $V_{\pi}L$  of 2.6 Vcm.  $V_{\pi}L$  is defined as the product of required phase shifter length  $L$  and applied voltage  $V$  in order to achieve complete modulation in MZI. The value of  $V_{\pi}L$  is governed by the amount of  $\Delta n$  under applied voltage  $V$  as required phase shifter length  $L = \lambda/2\Delta n$  for single-arm drive MZI modulator (the value of  $L$  is half in push-pull MZI modulator).  $V_{\pi}L$  also described the modulation efficiency as the modulation efficiency of a modulator is higher when the value of  $V_{\pi}L$  is smaller ( $\Delta n$  is higher). The calculated values here are compatible with state-of-the-art modulator results with a potentially lower fabrication costs. The loss coefficient at thermal equilibrium is around  $2.8 \text{ cm}^{-1}$ , with 5.2 mm long arm, the insertion loss due to the free-carrier absorption is around 6.3 dB. We assume that both arms are being implanted with dopants but modulation only in one arm. The effective index change against voltage is clearly a nonlinear response, which re-emphasizes the need of analysis on linearity of silicon modulators here.



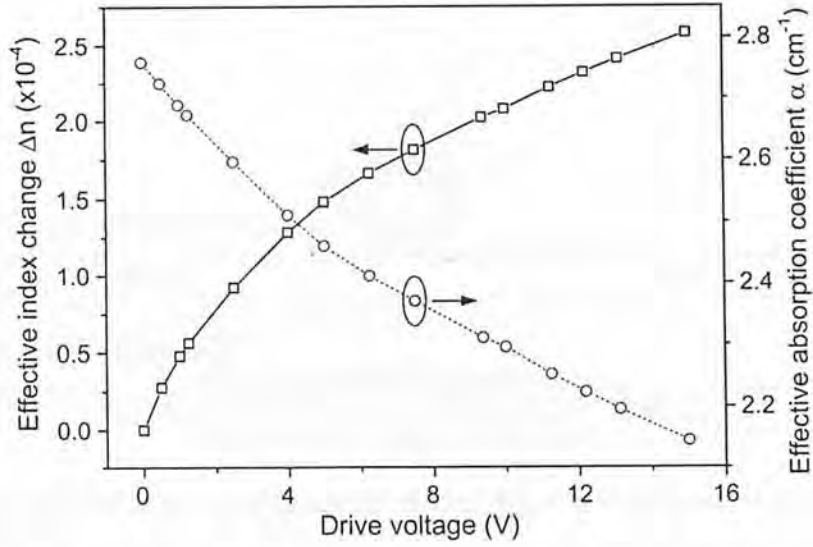


Fig. 2.1.2 Calculated effective refractive index and absorption coefficient changes as a function of drive reverse-bias voltage.

Figure 2.1.3 shows the modulators' configurations discussed in this section. They are MZI, single-ring-assisted MZI (RAMZI) and two-ring-assisted MZI (2RAMZI). RAMZI and 2RAMZI have been previously found to enhance the linearity of conventional linear electro-optic effect (LEO) modulators [45, 46]. A specified transmission coefficient(s)  $\tau$  of the ring resonator used to give a specified phase response. The phase response of the ring(s) thus linearizes the transfer function of the MZI structure. However, the applicability of RAMZI and 2RAMZI to silicon carrier-depletion modulators has not yet been studied. Furthermore, the limiting optical bandwidth and strict requirement on coupling coefficient become a big limitation in the particular employment of ring(s)-assisted MZI structures. However, these optical structures are good to be used in the theoretical analysis to see the various impacts by the carrier effect on linearity.



Fig. 2.1.3 Schematics of the configurations of ring(s)-assisted MZI and conventional MZI-based modulator structures.

The required optical phase changes in order to achieve complete modulation are different for different modulator designs. For instance,  $\pi$  phase change is needed in single-arm-drive MZI, while  $4\pi/3$  phase change is required in RAMZI [45] and value of phase change is depending on coupling coefficients in 2RAMZI [46].

The wavelength of the optical signal is set to be 1550 nm. We assume only one arm of the MZI is modulated in the MZI structure and one arm of the MZI is coupled to the modulated ring(s) in RAMZI and 2RAMZI structures. We also assume the rings have the same radius in the 2RAMZI. The modulator lengths were selected to give the required phase change ( $\pi$  for MZI) assuming a 5 V peak-to-peak modulation voltage  $V_{pp}$  and a reverse-bias  $V_{bias}$  of 2.5 V.

The transfer function of MZI modulator is given by:

$$T(\phi) = \frac{P_{out}}{P_{in}} = \frac{1}{2} (1 + \sin\phi) \quad (2.1.1)$$

where  $\phi$  is the phase difference between two arms of the MZI.

The phase term  $\phi$  is related to refractive index change  $\Delta n$  and phase shifter

length  $L$  in the MZI as:

$$\phi = \frac{2\pi}{\lambda} \Delta n L \quad (2.1.2)$$

In LEO-based modulators,  $\Delta n$  is changed linearly with applied voltage  $V$ . We set the phase shifter length  $L$  to give the  $\pi$  phase change when  $V_{pp} = 5$  V and  $V_{bias} = 2.5$  V, the phase term  $\phi$  is related to applied voltage  $V$  as:

$$\phi = \frac{\pi(V-2.5)}{5} \quad (2.1.3)$$

In the absence of loss in the ring resonator(s), the transfer function of ring(s)-assisted MZI is given by [46]:

$$T(\theta) = \frac{P_{out}}{P_{in}} = \frac{1}{2} (1 + \sin [G(\theta)]) \quad (2.1.4)$$

where  $\theta$  is the microring round-trip phase, and  $G(\theta)$  is the phase transfer function of the ring resonator(s):

$$G(\theta) = \tan^{-1} \left\{ \frac{(1-\tau_1^2)(2\tau_2 \sin \theta - \sin 2\theta)}{2\tau_1 + (1+\tau_1)^2(\tau_2^2 - 2\tau_2 \cos \theta) + (1+\tau_1^2) \cos 2\theta} \right\} \quad (2.1.5)$$

where  $\tau_1$  is the transmission coefficient of the first coupled ring resonator,  $\tau_2$  is the transmission coefficient of the second coupled ring resonator. In order to linearize the transfer function,  $\tau_1$  is set to be 0.268 and  $\tau_2$  is 1 (i.e. light does not coupled to the second ring) in RAMZI, while  $\tau_1$  is 0.3 and  $\tau_2$  is 0.21 in 2RAMZI [45,46].

The phase term  $\theta$  is related to refractive index change  $\Delta n$  and phase shifter length  $R$  in the ring(s)-assisted MZI as:

$$\theta = \frac{2\pi}{\lambda} \Delta n R \quad (2.1.6)$$

We set the phase shifter length  $R$  to give the  $4\pi/3$  required phase change in RAMZI and  $0.57\pi$  required phase change in 2RAMZI when  $V_{pp} = 5$  V and  $V_{bias} = 2.5$  V, the phase term  $\theta$  is related to applied voltage  $V$  as:

$$\theta = \begin{cases} \frac{2\pi (V-2.5)}{3} & (\text{for RAMZI}) \\ \frac{0.28\pi(V-2.5)}{2.5} & (\text{for 2RAMZI}) \end{cases} \quad (2.1.7)$$

By solving equation 2.1.1 and 2.1.3, we can obtain the transfer function of LEO-based MZI modulator with applied voltage. Similarly, by solving equation 2.1.4, 2.1.5 and 2.1.7, we can obtain the transfer functions of LEO-based RAMZI and 2RAMZI modulators with applied voltage. Figure 2.1.4 shows the calculated transfer functions of the LEO-based modulators. The modulator optical structures include MZI and ring(s)-assisted MZI.

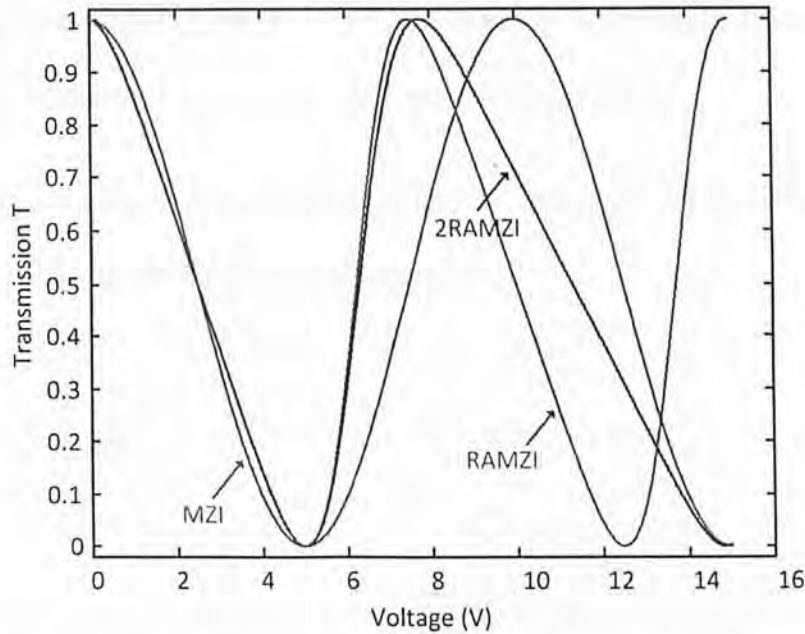


Fig. 2.1.4 Calculated transfer functions of the LEO-based modulator employing MZI and ring(s)-assisted MZI optical structures at a voltage bias of 2.5V.

From figure 2.1.4, the transfer functions of RAMZI and 2RAMZI are different



from the sine wave response of MZI, with a more linear slope compared with MZI. There is a conventional figure-of-merit used to measure the linearity of the transfer function – spurious-free dynamic range (SFDR) [41]. By definition, SFDR is equal to the signal-to-noise ratio (SNR) when the power of intermodulation (IMD) product meets the noise level. We thus evaluate the SFDR of these modulator structures by employing the two-tone input frequencies and analyze the fundamental harmonic and 3<sup>rd</sup> order intermodulation (3<sup>rd</sup> IMD) at the output product.

In order to investigate the linearity of different modulators here, the two-tone signals with frequency  $f_1 = 1$  GHz and  $f_2 = 1.2$  GHz were applied as input to the transfer functions. From the Fourier Transform of the modulated output signal we obtain the 3<sup>rd</sup> IMD signal at 0.8 GHz and fundamental signal at 1 GHz. Where the noise floor of the system is set to be -163 dBm in the simulations, which is a common value that has been used in similar work [45, 46]. The noise power is dominated by both the relative intensity noise of the laser and shot noise [67].

Figure 2.1.5 shows the calculated output RF power versus the input RF power in LEO based modulators for all optical structures.

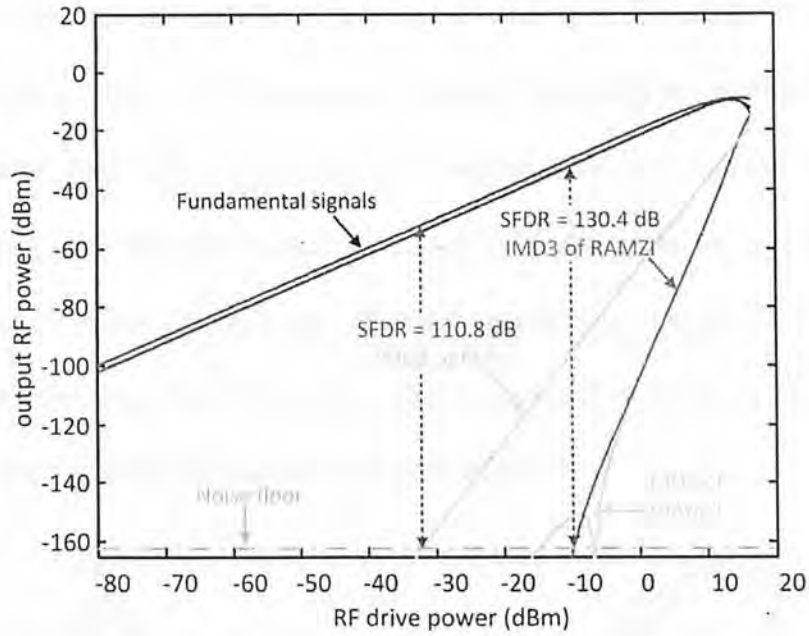


Fig. 2.1.5 Calculated RF output signal power and 3<sup>rd</sup> IMD power of LEO-based modulators as a function of RF input signal power.

The LEO MZI-based modulator gives a SFDR of 110.8 dB while the RAMZI-based modulator gives a SFDR of 130.4 dB in our calculation. The LEO 2RAMZI-based modulator gives a lower SFDR than RAMZI because of a ripple-like response in around -15 dBm drive input power. The response is supposed to be due to the numerical rounding error in the program in such small drive signals. The results here are matched with the published theoretical results in [45, 46], which shows our methodology and numerical program are feasible to calculate accurate SFDRs from the transfer functions.

In silicon depletion-based modulators,  $\Delta n$  is changed non-linearly with applied voltage  $V$  (as shown in figure 2.1.2). The non-linear change of  $\Delta n$  means the phase change against voltage in silicon depletion-based modulators is different from equation 2.1.3 and 2.1.7. We first set the length of phase shifters in all optical structures to provide the required phase change in  $V_{pp}$  of 5 V and  $V_{bias}$  of 2.5 V. We

numerically combine the function of  $\Delta n$  change with applied voltage in figure 2.1.2 with equation 2.1.1 and 2.1.2 to obtain the transfer function of silicon depletion-based MZI modulator. Similarly, we numerically combine the function of  $\Delta n$  change with applied voltage with equation 2.1.4, 2.1.5 and 2.1.6 to obtain the transfer functions of silicon depletion based RAMZI and 2RAMZI modulators. Figure 2.1.6 shows the calculated transfer functions of the silicon depletion-based modulators. The modulator optical structures include MZI and ring(s) assisted MZI.

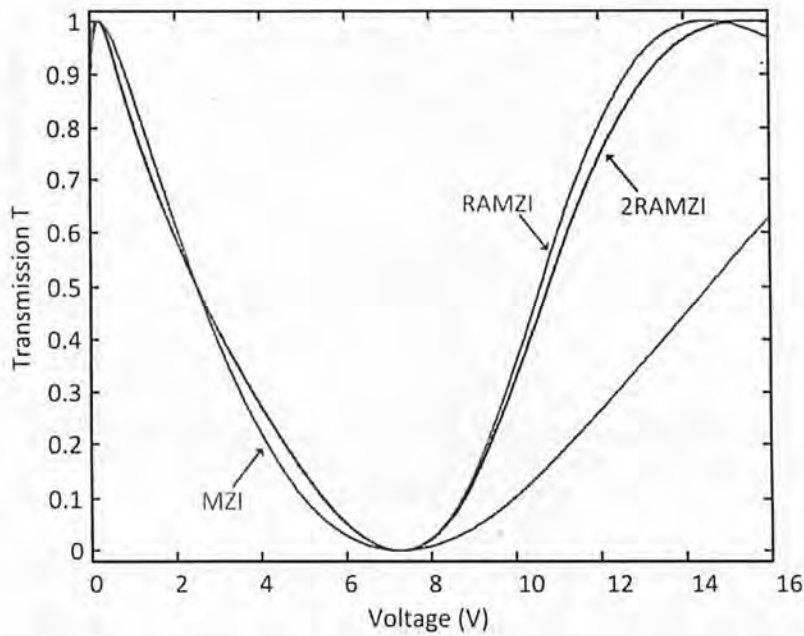


Fig. 2.1.6 Calculated transfer functions of the silicon depletion-based modulators based on MZI and ring(s) assisted MZI at a voltage bias of 2.5V.

Since the free-carrier effect in silicon depletion based modulators give nonlinear responses of refractive index change against applied voltage as shown in figure 2.1.2. The result of nonlinear responses is that the transfer functions in silicon-based modulator are different to LEO-based modulator for all optical structures. For example, the transfer function of silicon based MZI modulator is not a sine wave function. From figure 2.1.6, the variation of transmission is larger in small drive

voltage and smaller in large drive voltage, which is due to the approximately square-root like dependence of refractive index changes against applied voltage (as shown in figure 2.1.2).

Figure 2.1.7 shows the calculated output RF power versus the input RF power of a LEO based MZI modulator and a silicon carrier depletion-based MZI modulator.

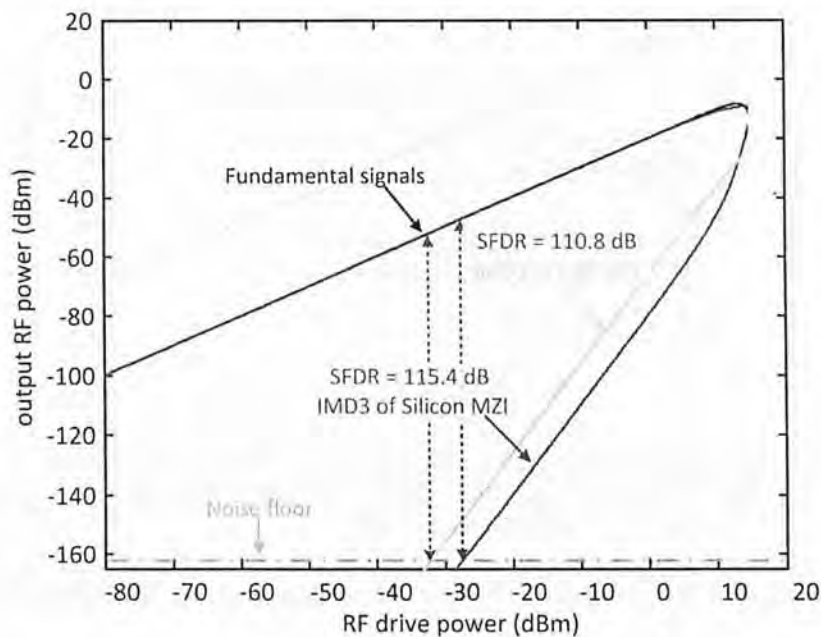


Fig. 2.1.7 Calculated RF output signal power and 3<sup>rd</sup> IMD power of both LEO- and silicon-based MZI modulators as a function of RF input signal power. The modulators are reverse-biased at 2.5V. From the simulation results, the SFDR of the silicon based MZI have 4.6 dB improvement from the LEO-based MZI.

From figure 2.1.7, the silicon-based MZI modulator has a 4.6 dB improvement in SFDR compared to the conventional LEO based MZI modulator. We attribute this improvement to the nonlinear response of refractive index change with voltage which actually helps linearize the MZI response.

Because of the nonlinear responses of refractive index changes against applied voltage, we also evaluate the SFDR of silicon-based modulators in various bias



voltages. Figure 2.1.8 shows the calculated output RF power versus the input RF power of silicon carrier depletion-based modulators including MZI and 2RAMZI at 7.5 V reverse bias voltage. For clarity we only show the SFDR of the 2RAMZI as the linearity of the RAMZI and the 2RAMZI were found to be quite similar [45, 46].

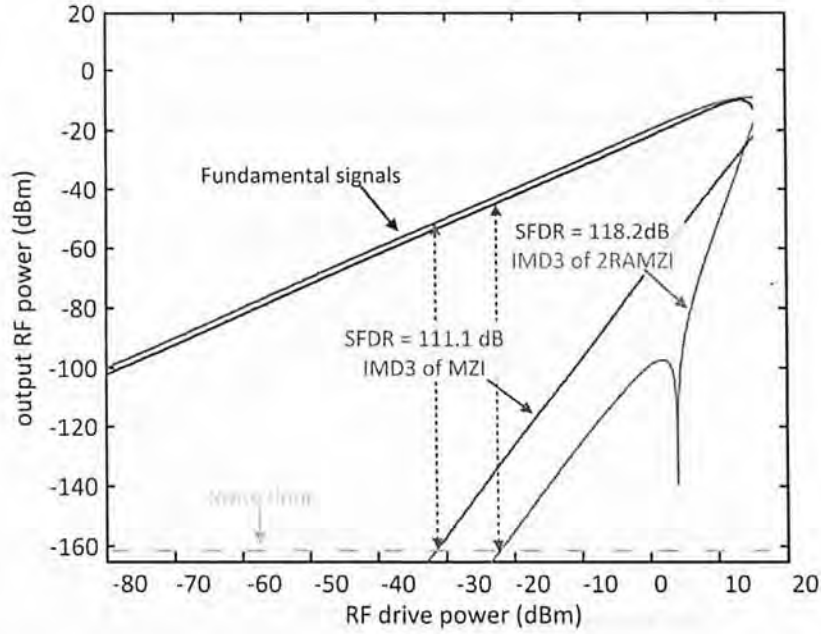


Fig. 2.1.8 Calculated RF output signal power and 3<sup>rd</sup> IMD power of the silicon-based MZI and 2RAMZI modulators as a function of RF input signal power. The modulators are reverse biased at 7.5V.

Comparing the results in figure 2.1.7 and figure 2.1.8, the SFDR of the silicon depletion-based MZI modulator is decreased from 115.4 dB to 111.1 dB when the bias voltage is increased from 2.5 V to 7.5 V. It is because of the response of refractive index changes against applied voltage becomes linear when the bias voltage increases from 2.5 V to 7.5 V. Figure 2.1.8 also shows the calculated SFDR of the 2RAMZI is around 118.2 dB at 7.5 V. The value is more than 10 dB lower than the SFDR of ring(s)-assisted MZI in LEO-based modulators. This means the nonlinear response of refractive index change in silicon depletion-based modulator degraded the

performance of the linearized transfer function in ring(s) assisted MZI structures.

Figure 2.1.9 shows the calculated values of SFDR in LEO MZI, silicon MZI and 2RAMZI modulators among various bias voltages. The bias voltages are ranged from 2.5V to 12.5 V.

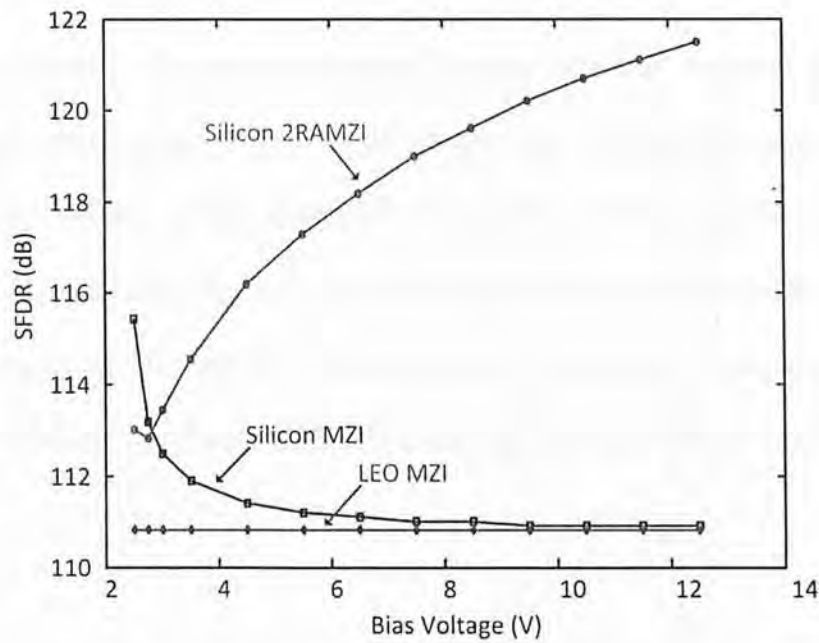


Fig. 2.1.9 Calculated SFDR of the silicon based MZI and 2RAMZI with various bias voltages.

From figure 2.1.9, the SFDR of silicon-based MZI modulator decreases as the bias voltage increases. In contrast, the SFDR of silicon-based 2RAMZI modulator increases as the bias voltage increases. In silicon-based MZI, the SFDR approaches the value in LEO-based MZI at the bias voltage of around 10 V. In silicon-based 2RAMZI, the SFDR increases to above 120 dB at the bias voltage of around 12 V, which approaches the value of SFDR in LEO-based 2RAMZI (130 dB). This matches the response of refractive index change against voltage in depletion-based modulators as higher drive voltage gives a linear response.

One may suggest that the phase response in the ring(s)-assisted MZI structure may also be able to be used to cancel the nonlinear response due the free-carrier effect. However, the tight fabrication tolerances required for the more complicated ring(s)-assisted MZI structures make them difficult to be achieved in practice. While silicon-based MZI modulators provide more relaxed fabrication requirements and simpler structure, with better linearity at a low bias voltage.

The results in this section suggest that the nonlinear response of refractive index change with voltage actually helps linearize the MZI transfer function while it degrades the linearity of the linearized modulators. Silicon depletion-based MZI modulators have higher linearity over LEO-based MZI modulators at a low bias voltage. With lower cost and CMOS-compatibility, the silicon depletion-based MZI modulator would be a potential candidate in the use of analog optical links.

## 2.2 Modeling of Dependence of Linearity on Various Diode Structures

From section 2.1, we show the linearity of silicon depletion based modulator in MZI structure can be improved by the nonlinear response of free carrier effect. When we published the results in [48], there were also reports that the linearity of silicon depletion-based modulators can be improved by tuning the bias voltage [49] and by changing the phase shifter length [50] in MZI-based structure.

However, these proposed methods are based on a unique diode design. As the diode design plays the key role in the depletion-based modulator, it determines the modulation efficiency (described by  $V_{\pi}L$  or  $\Delta n$ ) and insertion loss. In terms of linearity, different diode designs are supposed to give different nonlinear responses of refractive index change against voltage, which results in different transfer functions and linearity.

In this section, we theoretically analyze the linearity of silicon depletion-based modulators on a host of diode designs. An optimum diode design is proposed to linearize the transfer function of the silicon modulator. The wavelength of operation is assumed to be 1.55  $\mu\text{m}$  in this section.

Here we investigate several horizontal  $p^+-p(i)-n-n^+$  diode structure designs for the conventional MZI-based modulator structure. Figure 2.2.1 shows the cross-sectional schematics of the optical waveguide, optical TE mode field distribution and  $p^+-p(i)-n-n^+$  diode. The waveguide width is 500 nm, height is 340 nm while slab thickness is 140 nm. The waveguide dimension used here is defined by considering a simple single-etching fabrication step of waveguides and efficient grating couplers on a 340nm thick SOI wafer. The optical waveguide can support multi mode propagation, however, the grating couplers can act as the mode filters to excite only the



fundamental mode in the waveguide. The  $p^+$ - and  $n^+$ -doped regions are separated from the waveguide sidewalls with a spacing of around 500 nm. The doping concentrations for the  $p^+$  and  $n^+$  slab region are around  $1 \times 10^{20} \text{ cm}^{-3}$ . The moderately doped p and n concentrations are around  $2 \times 10^{18} \text{ cm}^{-3}$  in order to achieve an efficient amount of depleted carriers in about 5 V.

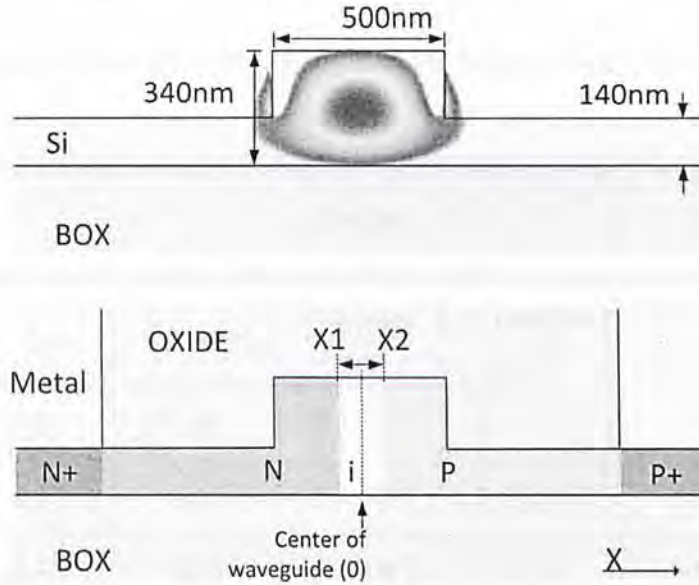


Fig. 2.2.1 (top) Cross sectional schematic of the waveguide and TE mode field distribution. (down) Cross sectional schematic of the  $p^+$ -p-(i)-n-n<sup>+</sup> diode

In figure 2.2.1, X1 and X2 are defined by the distance from the center of waveguide to the moderately doped region. In our analysis, seven diode designs are defined by changing the doping windows of p and n implantation process and implantation doses. The diode structures are simulated by the commercial semiconductor process simulation software Athena by Silvaco [51]. The dopant used for p-doped ion implantation is boron, while the dopant used for n-doped region ion implantation is phosphorus. For all the designs, the ion implantation dosage for  $p^+$  is  $3 \times 10^{15} / \text{cm}^2$ , energy is 20 keV, and tilt angle is  $7^\circ$ . While the ion implantation dosage for  $n^+$  is  $2 \times 10^{15} / \text{cm}^2$ , energy is 40 keV, and tilt angle is  $7^\circ$ . After the steps of ion

implantation, a thermal annealing of 1000 °C for 30 minutes has been performed for all the designs. The oxide via and metal electrodes are defined after the annealing. The processes in the simulation are supposed to be the same as the processes used in actual fabrication in order to compare the simulation results and experimental results of the fabricated devices. Table 2.1 lists the parameters used in the simulations for various diode designs. The parameters include doping windows (X1, X2), ion implantation dose and energy. The tilt angle in the implantation processes is 7°.

Table 2.1 Simulation parameters of various silicon depletion-based modulator designs

Design	X1 (μm)	X2 (μm)	P dosage (/cm <sup>2</sup> )	N dosage (/cm <sup>2</sup> )	P energy (keV)	N energy (keV)
A	0.00	0.00	$5 \times 10^{13}$	$2 \times 10^{13}$	50	75
B	-0.15	0.15	$5 \times 10^{13}$	$2 \times 10^{13}$	50	75
C	-0.05	0.05	$5 \times 10^{13}$	$2 \times 10^{13}$	50	75
D	-0.10	0.10	$5 \times 10^{13}$	$2 \times 10^{13}$	50	75
E	-0.20	-0.10	$5 \times 10^{13}$	$2 \times 10^{13}$	50	75
F	-0.20	0.00	$5 \times 10^{13}$	$2 \times 10^{13}$	50	75
G	-0.20	0.00	$8 \times 10^{13}$	$2 \times 10^{13}$	50	75

The parameters used in our simulations are based on an efficient diode design A. In the initial simulation it gives a refractive index change of around  $2 \times 10^{-4}$  at 5 V reverse-bias drive voltage. The modulation efficiency here is optimized by the ion implantation energy and dose in a fixed optical waveguide structure and annealing process. Designs B-F are the variants of design A. They have different doping windows (X1, X2) from design A. Design G has a larger p dose than design F as other



parameters remain the same. In the depletion-based modulation of  $p^+p(i)n-n^+$  diodes, the application of a reverse-bias remove free-carriers from the depletion region inside the waveguide. By using the commercial semiconductor simulation software Atlas, by Silvaco [51] and combining the free-carrier effect and mode distribution, we are able to find out the effective index changes and absorption coefficient changes upon various biases. Again, the detailed methodology of simulation is described in Appendix D.

Figure 2.2.2 shows the calculated effective index changes as a function of drive reverse-bias voltage for diode designs A-G. We observe that all the refractive index change responses behave square-root-like dependence of drive voltage. At 5V reverse bias voltage, diode design A gives the highest refractive index change of around  $2 \times 10^{-4}$ , corresponding to a  $V_{\pi}L$  of 2.2 Vcm.

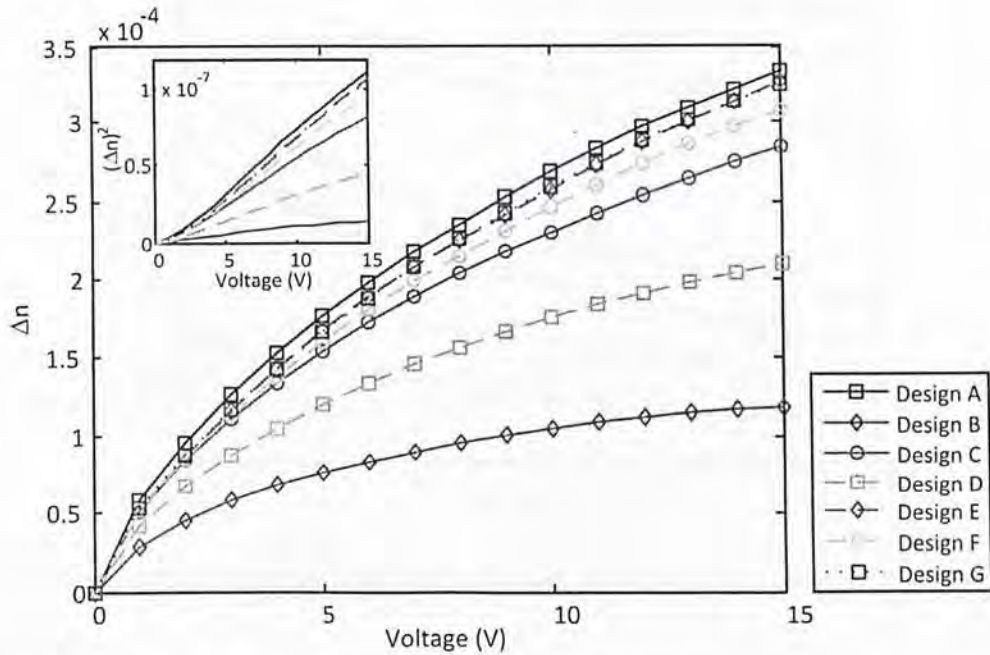


Fig. 2.2.2 Calculated effective refractive index changes as a function of drive voltage for diode designs A-G. Inset shows the plot of square of refractive index changes as a function of drive voltage, the refractive index change responses behave a square-root-like dependence of drive voltage.

Figure 2.2.3 shows the calculated absorption coefficient changes as a function of drive reverse-bias voltage for diodes A-G. The absorption coefficients range from around 1 /cm to 3 /cm at thermal equilibrium. As diode designs A-F are with the same doping concentration, less than few hundred nanometer variation of doping windows gives a loss coefficient variation of more than 100%. The results indicate the fabrication tolerance of this design in practice is quite strict. Because of this limitation, we are finding a novel diode design to increase the robustness of fabrication tolerance, which will be discussed in chapter 3. However, in our theoretical analysis here, the various diode designs are aimed to give the comparisons on the linearity. The fact of poor fabrication tolerance does not affect our analytical results, but it gives the challenges on the experimental verification.

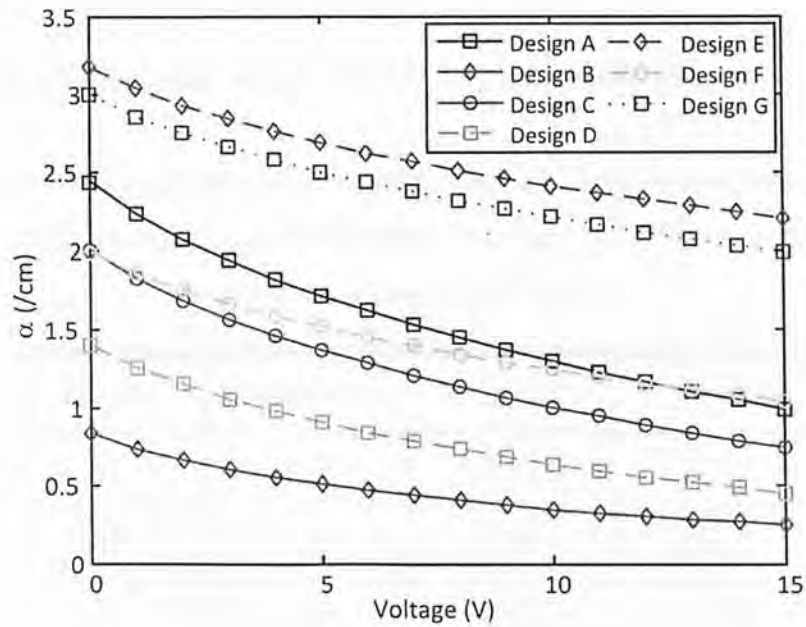


Fig. 2.2.3 Calculated absorption coefficient changes as a function of drive voltage for diode designs A-G.

The required modulator lengths are derived to satisfy the  $\pi$  phase change by assuming a 5 V peak-to-peak modulation voltage with a bias voltage of 2.5 V. We



assume only one arm of the MZI is modulated but diodes are embedded in both arms of the MZI. The insertion loss due to the free-carrier absorption is calculated by multiplying the loss coefficient at 2.5V bias and the required length. The wavelength of the optical signal is 1550 nm.

Using the similar methodology in section 2.1, we combine the calculated refractive index change in figure 2.2.2 with equation 2.1.1 and 2.1.2 to calculate the transfer function of different modulator designs. We then analyze the modulator linearity by SFDR. We evaluate the SFDR of the modulator by employing the two-tone input frequency ( $f_1 = 2.2$  GHz and  $f_2 = 2.4$  GHz) to the transfer function and from the Fourier Transform of the modulated output signal we obtain the 3<sup>rd</sup> IMD signal at 2.6 GHz and fundamental signal at 2.2 GHz. Table 2.2 lists the calculation results of the required modulator length, insertion loss due to the free-carrier absorption and SFDR at bias voltage of 2.5 V for all the diode designs.

Table 2.2 Calculation results of the required modulator length, insertion loss due to the free-carrier absorption and SFDR at bias voltage of 2.5 V of various silicon depletion-based modulator designs

Design	Length (mm)	Loss (dB)	SFDR (dB)
A	4.38	3.82	113.7
B	10.15	2.79	116.7
C	5.03	3.54	113.8
D	6.46	3.08	114.4
E	4.64	5.83	112.9
F	4.84	3.59	113.6
G	4.65	5.47	113.5

From table 2.2, design B gives the highest SFDR of 116.7 dB, which is 5.9 dB higher than the SFDR of LEO-based MZI modulator. Design B also gives the longest required length of around 1 cm in one-arm-drive MZI configuration. However, it gives the smallest free carrier absorption loss of 2.79 dB, which is due to an intrinsic region of 300 nm defined between the p and n doped regions.

Figure 2.2.4 shows the calculated SFDRs of all the designs with various bias voltages from 2.5 V to 7.5 V. Similar to the results in figure 2.1.9, the SFDR decreases as the bias voltage increases, asymptotically approaching the SFDR of LEO-based MZI modulators.

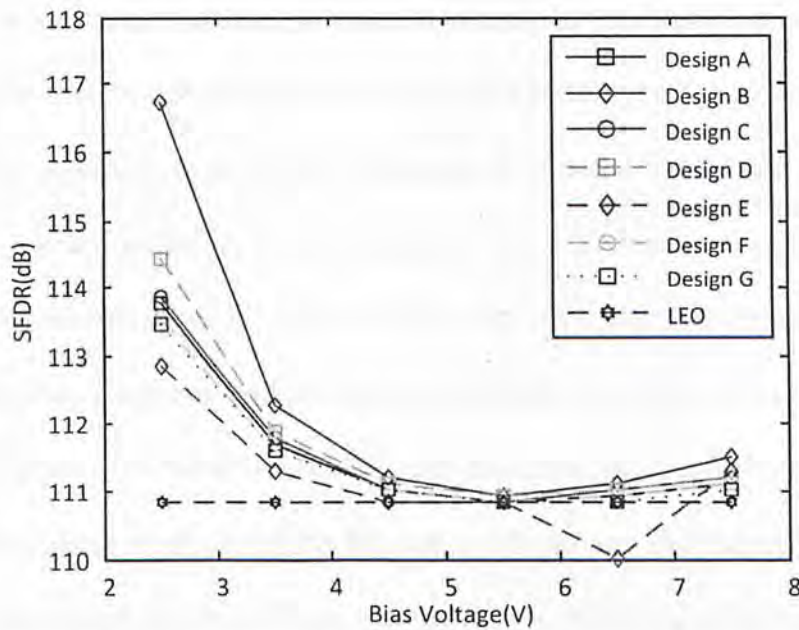


Fig. 2.2.4 Calculated SFDRs of diode designs A-G at various bias voltages

In this section, our theoretical analysis shows that the linearity of the silicon MZI optical modulator can be optimized by changing the diode design. The SFDR of silicon MZI modulators based on a reverse-bias  $p^+p\text{-}i\text{-}n^+$  diode has the highest improvement of 5.9 dB compared with conventional linear electro-optic effect MZI modulators.

### 2.3 Experiment of Radio-over-Fiber Signal Transmission by a Carrier-Injection

#### Silicon Microring Modulator

In this section we experimentally demonstrate a radio-over-fiber (ROF) signal transmission through a silicon modulator based on carrier-injection in a microring resonator structure.

We have fabricated two designs on  $p^+ - i - p - i - n^+$  diode embedded depletion-based modulator by oversea foundry service and the clean room facilities in local university (as described in this section). However, the fabricated devices did not perform optical modulation under reverse-bias applied voltage (by carrier-depletion) but they perform optical modulation under forward-bias applied voltage (by carrier-injection). The failures are mainly due to the fabrication error during the processes. Although the modulation speed in carrier-injection-based modulator is typically slower than carrier-depletion-based modulator when pre-emphasis circuit is not employed (as shown in table 1.7), we still can use the carrier-injection-based microring modulator here to experimentally demonstrate an application in ROF links with lower speed. In future work, we can also use the carrier-depletion-based microring modulator to demonstrate the same experiment with higher modulation speed when the carrier-depletion based modulator is successfully fabricated.

The transmission and distribution of long-reach (LR) ROF signal is challenging due to the chromatic-dispersion-generated periodic power fading and code time-shifting effect in the optical fiber. One promising method is to use single-sideband (SSB) ROF signal. However, the conventional generation of SSB-ROF signal requires tight optical filtering [52] or separate modulation and combination of



the sidebands [53, 54]. By using the narrow optical bandwidth characteristic of the microring resonator, here we report a convenient way to generate the SSB-ROF signal.

We first describe the fabrication process of the modulator, and then show the experimental setup, finally give the experimental results for LR SSB-ROF signal transmission up to 100 km long single-mode fiber (SMF).

### ***2.3.1 Device Fabrication***

The silicon microring modulator is fabricated by a ‘mix-and-match’ process of electronic beam lithography (EBL) in Micro and Nano Fabrication Laboratory (MNF) at The Chinese University of Hong Kong (CUHK) and i-line photolithography in Nanoelectronics Fabrication Facility (NFF) at The Hong Kong University of Science and Technology (HKUST). The step of defining grating coupler is fabricated in CUHK by using the EBL while other steps are fabricated in HKUST by using the i-line stepper.

Fig. 2.3.1 shows the schematic of the fabrication process flow for silicon modulators based on carrier-injection in a microring resonator structure.



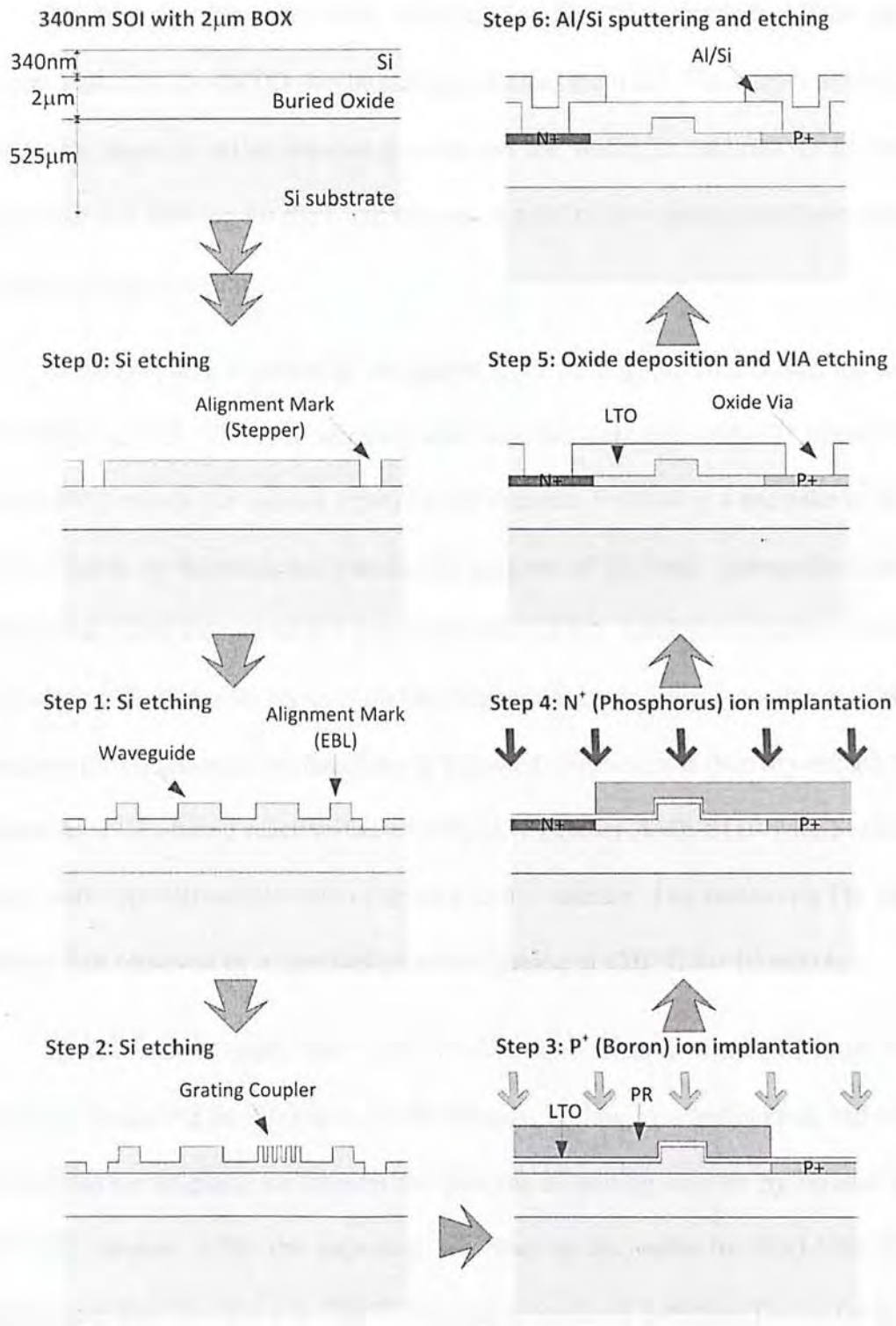


Fig. 2.3.1 Schematic of the fabrication process flow for silicon modulators based on carrier-injection in a microring resonator structure.

We fabricate the device on a 100 mm (4 inch) SOI wafer with 340nm top Si on 2  $\mu$ m buried oxide (BOX) purchased from Soitec, Inc. [55]. There are a total of six lithography steps to define various patterns on the wafer, in addition to an initial alignment mark forming for the i-line stepper. A total of five masks have been used in the photolithography steps.

In the first step concerning waveguide layer etching, we first coated the wafer with HMDS at 105 °C for 60 seconds, and then spin coat with AZ1075 photo resist (PR) at 4000 rounds per minute (rpm) for 60 seconds. Following a softbake at 90 °C for 60 seconds on hotplate, we transfer the patterns of photonic waveguide layer by ASML-5000 i-line stepper with a projection ratio of 5:1. After the exposure, we bake the resist at 110 °C for 90 seconds on hotplate, and then develop the wafer by FHD-5 developer for 60 seconds. No hardbake is followed. The wafer is then dry-etched for 9 minutes by a CF<sub>4</sub>-based reactive-ion-etching (RIE) etcher AME-8110 with Si etching recipe, with top silicon etch rate of around 220 Å/minute. The remaining PR on the wafer is then removed by a standard piranha cleaning at 120 °C for 10 minutes.

In the second step, the wafer is first spin coated with ZEP520A high-resolution ebeam PR at 3500 rpm for 60 seconds. Following a softbake at 180 °C for 180 seconds on hotplate, we transfer the patterns of grating coupler by Elionix ELS-7800 EBL system. After the exposure, we develop the wafer by ZED-N50 for 60 seconds, and then hardbake at 120 °C for 180 seconds on hotplate. The wafer is then dry-etched for 6 minutes by a SF<sub>6</sub>-based inductively-coupled-plasma (ICP) deep-reactive-ion-etching (DRIE) etcher Oxford Plasma Lab 100, with top silicon etch rate of around 340 Å/minute. The remaining PR on the wafer is then removed by the O<sub>2</sub> plasma in the same chamber for 5 minutes.

Prior to the third step, the wafer is first deposited with 250 Å thick low temperature oxide (LTO) in a furnace. The LTO acted as a sacrificial oxide layer during the ion implantation processes.

In the third and fourth steps, the wafer is first coated with HMDS at 105 °C for 60 seconds, and then spin coated with FH6400L PR at 4000 rpm for 60 seconds. Following a softbake at 110 °C for 60 seconds on hotplate, we transfer the patterns of p<sup>+</sup>- and n<sup>+</sup>- doped region by ASML-5000 i-line stepper. After the exposure, we develop the wafer by FHD-5 developer for 60 seconds, and then hardbake at 180 °C for 30 minutes in oven prior to the high-dosage ion implantation processes. We then use Varian CF3000 ion implanter to form the p<sup>+</sup>- and n<sup>+</sup>- doped regions. We implant boron for p<sup>+</sup> doping with the dosage of  $3 \times 10^{15} / \text{cm}^2$ , energy of 20 keV, and tilt angle of 7°. We implant phosphorus for n<sup>+</sup> doping, the dosage is  $2 \times 10^{15} / \text{cm}^2$ , energy is 40 keV, and tilt angle is 7°. After the ion implantations, we remove the resists on top by oxygen plasma cleaning in PS210 photo resist asher for 25 minutes. The wafer is then cleaned by a standard piranha cleaning at 120 °C for 10 minutes.

After the fourth steps, the 250 Å sacrificial oxide layer is removed from the wafer by buffered oxide etchant (BOE) for 60 seconds, and then re-deposited with 8000 Å thick LTO in the furnace. The 8000 Å oxide acted as a upper-cladding of the optical waveguide in order to prevent the loss induced by the modal overlap between the evanescent field and the metal. We then anneal the wafer at 1000 °C for 30 minutes in the furnace. The annealing process provides the functions of dopants activation and LTO densification.

In the fifth step, the pattern of oxide via is defined as the same recipe used in the first step for photonic devices. After the steps of photolithography, the wafer is

dry-etched for 15 minutes by a  $\text{CF}_4$ -based RIE etcher AME-8110 with  $\text{SiO}_2$  etching recipe, with LTO etch rate of around  $360 \text{ \AA}/\text{minute}$ . Then we wet-etch the wafer by BOE for 2 minutes in order to ensure the oxide via are opened through to provide good contact between metal and highly doped regions. We remove the resists by a standard piranha cleaning at  $120^\circ\text{C}$  for 10 minutes.

Finally, in the sixth step, the wafer is first sputtered with  $8000 \text{ \AA}$  thick Al:Si (1%) by Varian 3180 sputtering system. After the sputtering, the wafer is first coated with HMDS at  $105^\circ\text{C}$  for 60 seconds, and then spin-coated with HPR504 PR at 4000 rpm for 60 seconds. Following a softbake at  $110^\circ\text{C}$  for 60 seconds on hotplate, we transfer the patterns of metal contact by ASML-5000 i-line stepper. After the exposure, we develop the wafer by FHD-5 developer for 60 seconds, and then hardbake at  $120^\circ\text{C}$  for 30 minutes in oven prior to the wet metal etching. We wet-etch the Al/Si on the wafer by a  $\text{H}_3\text{PO}_4:\text{CH}_3\text{COOH}:\text{HNO}_3$  (100:10:1) solution at  $50^\circ\text{C}$  for 5-6 minutes. After the wet-etching, the wafer is dip in the Freckle etch solution for 2 minutes to remove the silicon residues left on the wafer. We then remove the resists by a MS2001 at  $120^\circ\text{C}$  for 10 minutes. We finally perform forming gas annealing (FGA) at  $400^\circ\text{C}$  for 30 minutes in order to achieve lower contact resistance.

Figure 2.3.2 (a) shows the cross-sectional schematics of the optical waveguide, the simulated optical transverse-electric (TE) mode field distribution and the  $\text{p}^+ \text{-i-n}^+$  diode. The waveguide width is 500 nm, height is 340 nm while the slab thickness is 140 nm in order to provide a conductive path between two electrodes. The waveguide dimension used here is defined by considering a simple single-etching fabrication step of waveguides and efficient grating couplers on a 340 nm thick SOI wafer. The optical waveguide can support multi-mode propagation, however, the grating couplers can act as the mode filters to excite only the fundamental mode in the



waveguide. The  $p^+$ - and  $n^+$ -doped regions are separated from the waveguide sidewalls with a spacing of around 500 nm. The doping concentrations for the  $p^+$ -doped region is around  $6 \times 10^{19} \text{ cm}^{-3}$  while for the  $n^+$ -doped region is around  $2 \times 10^{20} \text{ cm}^{-3}$ .

Figure 2.3.2 (b) shows the top-view microscope image of the fabricated silicon microring modulator on a SOI chip. The microring resonator has a ‘racetrack’ shape in order to increase the strength of evanescent coupling from the input waveguide. The designed racetrack microring arc radius is 20  $\mu\text{m}$ . The designed straight interaction length is 15  $\mu\text{m}$ . Our designed gap spacing between the sidewalls of the waveguides is 400 nm, which is 100 nm smaller than the critical dimension of the i-line stepper (500 nm), so the exposure energy and focus value during the photolithography process should be fine-tune in order to achieve gap opening. The metal contacts on the highly doped regions are extended to a ground-signal-ground (GSG) pad for high-speed probing.

Figure 2.3.2 (c) shows the cross-sectional scanning electronic microscope (SEM) image of our fabricated optical waveguide on the same SOI wafer. The upper-oxide cladding is removed by HF solution after the whole fabrication processes. The measured waveguide height is around 340 nm, width is around 570 nm and the slab is around 120 nm. The sidewall slope angle is around  $75^\circ$ . The waveguide width difference between the fabricated device and our design may be attributed to the limited resolution of the i-line stepper and the imperfect etching slope angle. The slab thickness is 20 nm smaller than our design, which may be due to the imperfect control of etching time and non-uniformity of etching.

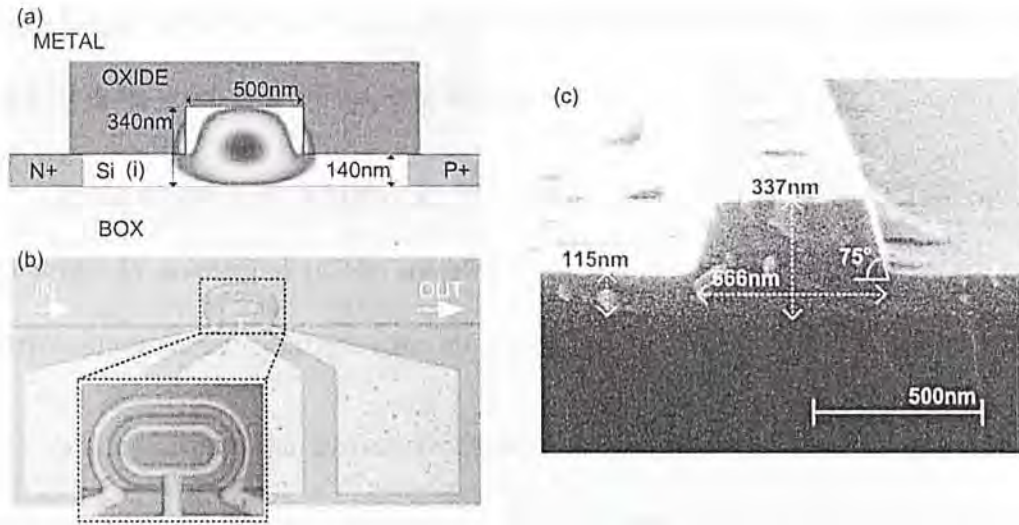


Fig. 2.3.2 (a) Cross sectional schematic of the optical waveguide, the simulated optical transverse-electric (TE) mode field distribution and the schematic of the embedded  $p^+-i-n^+$  diode. (b) Top-view microscope image of the fabricated silicon carrier injection-based modulator. Inset: zoom-in microscope image of the ring resonator (c) Cross sectional scanning electron microscope (SEM) image of our fabricated optical waveguide on SOI. The upper oxide cladding is removed by BOE.

### 2.3.2 Experimental Setups

Figure 2.3.3 shows the schematic of experimental setup in our work. A wavelength-tunable laser (1509 nm – 1640 nm wavelength) is used as light source. The laser beam is first launched to the erbium-doped fiber amplifier (EDFA) and then the band-pass filter (BPF). The beam is then TE-polarized by the polarization controller (PC), and then coupled to our device by a cleave-end SMF and a grating coupler. The output beam from the out-port of the device is coupled out by another pair of grating coupler and cleave-end SMF. The beam is then launched to the second EDFA and second BPF. Before entering the photodetector, the beam passes through

various lengths of SMF: (1) 0 km / back-to-back (B2B), (2) 50 km, (3) 100km (with a third EDFA between two 50 km long fibers).

In the experiment, a high-speed (40 GHz) ground-signal (GS) radio-frequency (RF) probe is connected to the metal pad of our device in order to measure the electrical characteristic and drive the electrical data.

The electrical data comes from the pattern generator is combined with the direct-current (DC) signal through a bias-T, and then drive the silicon modulator by the GS RF probe. The electrical data from the photodetector can be either connected to the oscilloscope or the pattern generator in order to characterize the modulated signal performance.

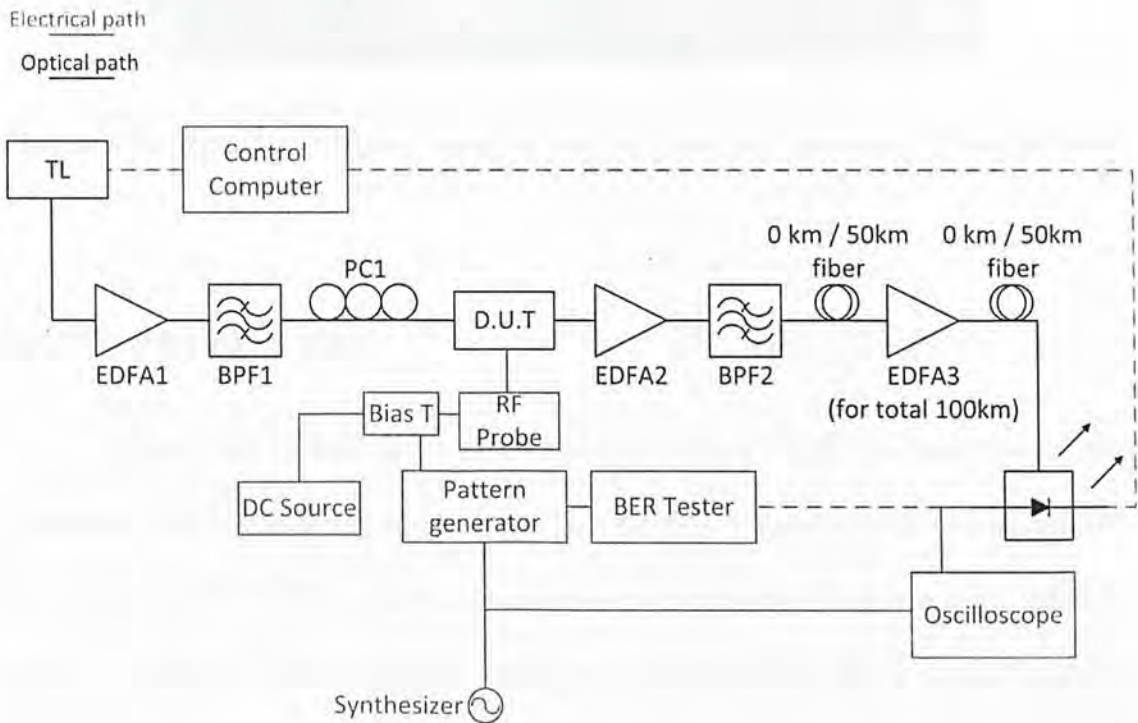


Fig. 2.3.3 Experimental setup in the testing of ROF signal transmission by using a silicon microring modulator. We employ LR signal testing of (1) B2B (0km), (2) 50km and (3) 100km long SMF.



Figure 2.3.4 shows the photograph of the optical coupling setup in our experiment. We use a long-distance lens and a CCD camera to monitor the position of the grating couplers and the SMFs. From the inset of figure 2.3.4, the SMFs are  $10^\circ$  tilt from the normal axis of the wafer.

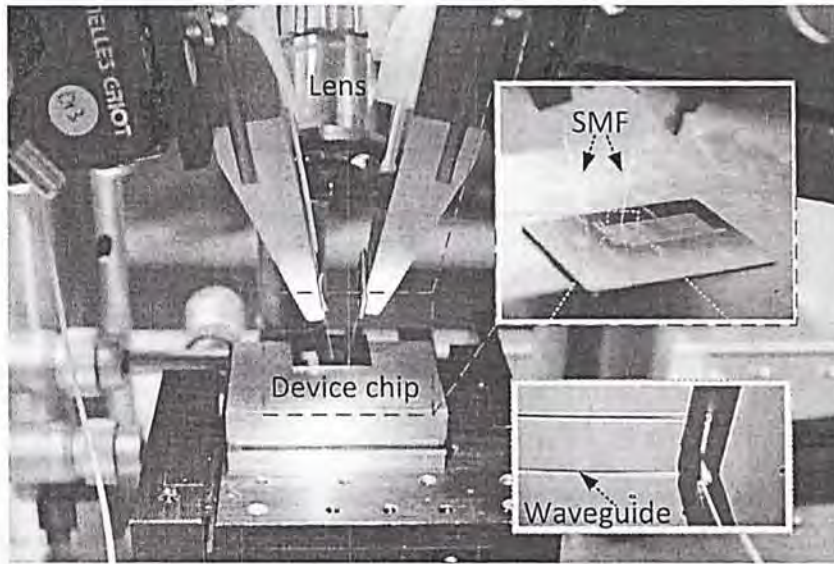


Fig. 2.3.4 Photograph of the optical coupling setup by grating couplers used in the experiment.

### 2.3.3 Experimental Results

Figure 2.3.5 shows the measured current-voltage (IV) characteristic of the fabricated silicon microring modulator. The results are measured by connecting the RF probe to HP 4145B semiconductor parameter analyzer through a BNC cable in order to ensure small resistance attributed by the setup. The measured current limitation of the analyzer is set to 30 mA. The turn-on voltage of the  $p^+i-n^+$  diode is around 1 V, and the turn-on resistance is around  $18\ \Omega$ . The IV characteristic of the device shows typical diode responses with relatively low turn-on voltage and low contact resistance. The results indicate a good fabrication process for the ion implantation, oxide via and metal contact layers.



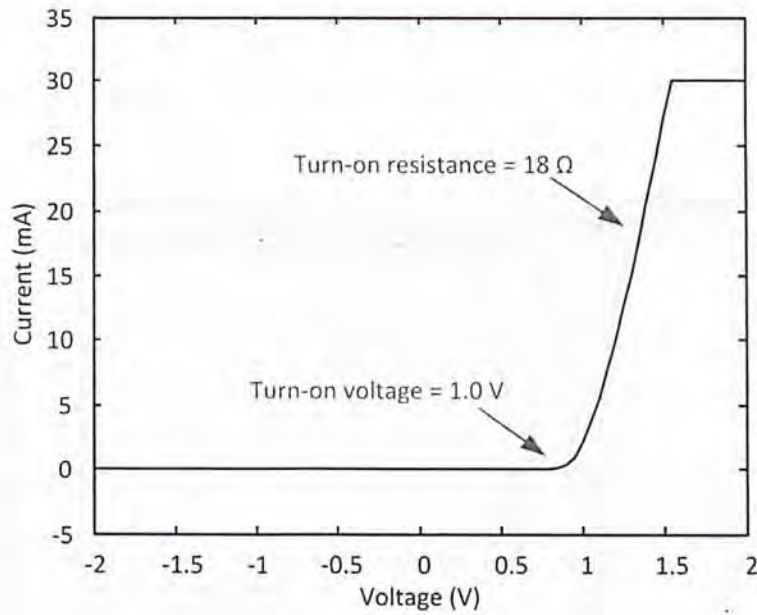


Fig. 2.3.5 Measured IV characteristic of the fabricated silicon microring modulator embedded with a  $p^+i-n^+$  diode

Figure 2.3.6 shows the measured transmission spectra of the silicon microring modulator under various forward bias DC voltages. The resolution of the spectra is 0.005nm. The spectra are normalized with the transmission of a reference waveguide. The forward-bias DC voltages are 0.5V, 0.8V, 0.9V and 1.0V. The resonance wavelength is shift towards shorter wavelength when the bias voltage increases, which is an evidence of modulation caused by injection of free-carriers inside the waveguide to reduce the refractive index. The spectrum at 0.5 V is almost the same as the spectrum at 0.0 V (not shown in the figure), which means that the  $p^+i-n^+$  diode does not turn on at 0.5 V (as carriers have not been injected into the waveguide). The full-width-at-half-maximum (FWHM) of the resonance is around 0.215 nm. Thus the quality factor  $Q$  is around 7000 at wavelength of 1530 nm for the microring resonator. The extinction ratio (ER) is around 16 dB for DC voltages below 0.5V. The  $Q$  is reduced to around 6000 while ER reduced to around 6 dB when the DC voltage is 1.0

V. The decrease of the ER and Q are due to the free-carrier absorption of the injected carrier into the waveguide.

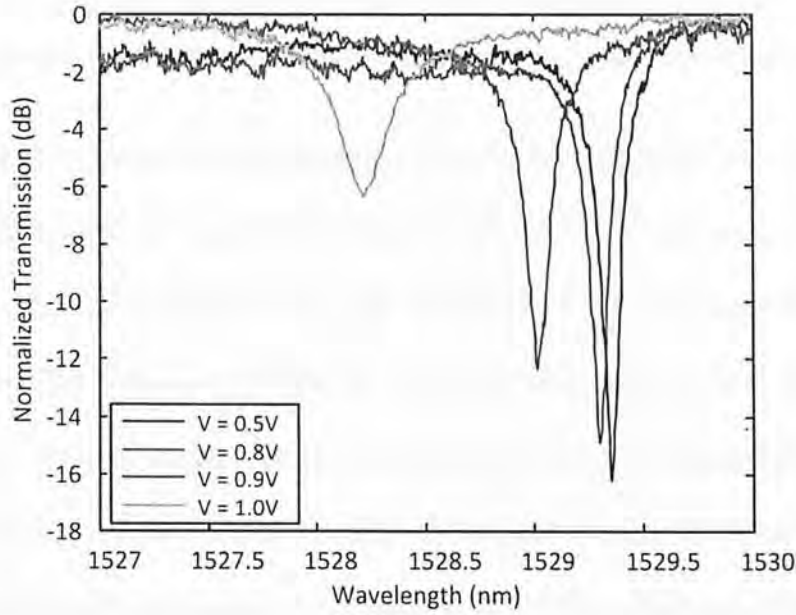


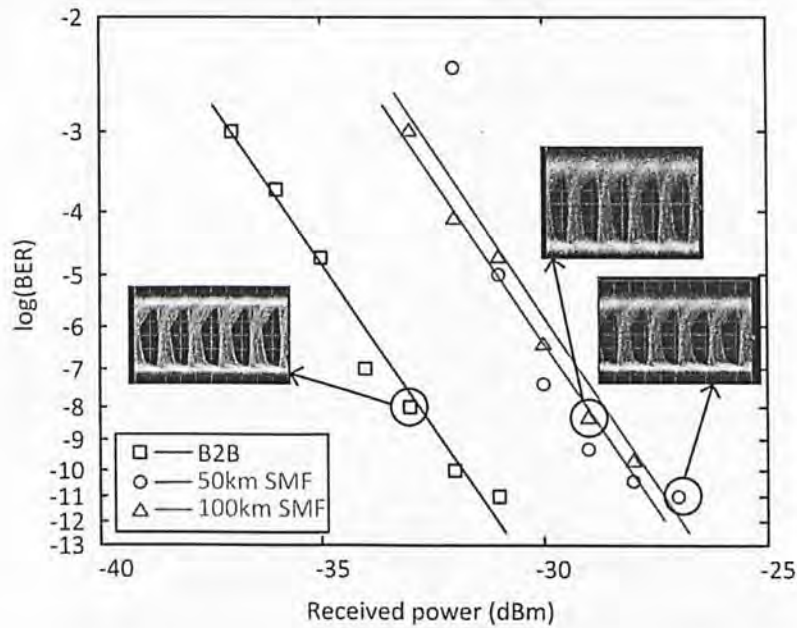
Fig. 2.3.6 Measured transmission spectra of the silicon microring modulator under various forward bias DC voltages

From the experimental results of other testing patterns, the typical measured coupling loss per grating coupler is around 6 dB. The waveguide loss measured by cut-back method is around 3 dB/mm. The coupling and waveguide losses are higher than the expectation. We attribute the high loss mainly to the fabrication imperfection, especially the silicon etching processes.

In the testing of ROF signal transmission, we first examine the high-speed digital data transmission capability of the silicon microring modulator. The probe wavelength of the input beam is set to 1529.35 nm, the resonance null when DC voltage is 0.5 V. The non-return-zero (NRZ) electrical driving signal has peak-to-peak voltage of 2 V, as directly output from the pattern generator. The DC bias level is fine-tuned to obtain the best output signal in every measurement. A RF amplifier has

been used. During the experiment, the highest data rate to maintain good eye opening of the output signal is 1.5 Gb/s. We supposed the speed is limited by the carrier recombination life time ( $\sim$ few ns [27]) of the injected free carrier. In our experimental demonstration of LR SSB-ROF transmission, we set the input data rate at 1 Gb/s.

We then examine the data transmission in a long-distance fiber. Figure 2.3.7 shows the NRZ bit-error rate (BER) measurement of the output signal for back-to-back, 50km fiber and 100km fiber. The insets shows the eye diagrams of  $2^7 - 1$  Pseudorandom Bit Sequence (PRBS) at 1 Gb/s for B2B, 50 km and 100 km SMF transmissions. From all cases, a clear eye opening is obtained. Error-free transmission ( $\text{BER} < 10^{-9}$ ) is measured without error-floor. We observed 2.5 dB power penalties in the 50km SMF transmission and an additional of 1.5 dB power penalties in the 100 km SMF transmission.





We generate an optical two-tone signal by optical carrier suppress (OCS) to replace the monochromatic input beam sources. We drive a 20 GHz sinusoidal wave from the synthesizer into the commercial high-speed MZI-based modulator at the null point to generate an optical two-tone with 40 GHz separation. The lower wavelength sideband at 1528.917 nm in the optical two-tone signal is then modulated by the ring modulator, in order to generate a SSB-ROF signal in the experiment. We choose the sideband at shorter wavelength because the resonance blue shift in the modulator would not affect the signal.

Figure 2.3.8 shows the measured transmission spectrum of the SSB-ROF signal generated by the silicon microring modulator. The spectrum is measured by optical spectrum analyzer (OSA) with resolution of 0.01 nm. The wavelength spacing between the two tones is around 0.3 nm, corresponding to 40 GHz frequency spacing. It shows a high center wavelength suppression of larger than 20 dB.

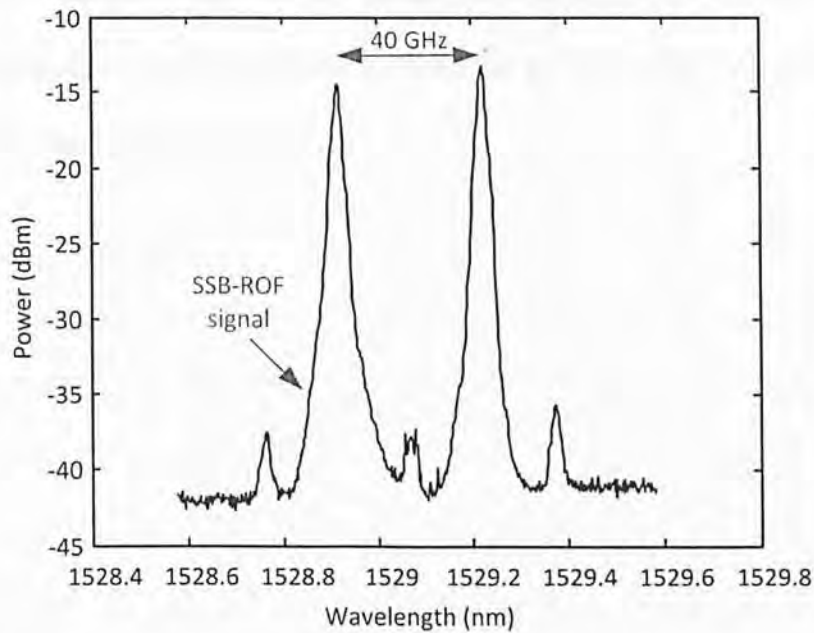


Fig. 2.3.8 Measured wavelength spectrum of the SSB-ROF signal



## 2.4 Summary

In summary, we present the theoretical studies on linearity of silicon depletion-based modulators and experiment of analog optical signal transmission by a silicon injection-based modulator. We find that the linearity of silicon depletion-based modulators can be improved by the nonlinear response of refractive index change of free-carrier effect. In MZI modulator structures, the SFDR of silicon depletion-based modulators is 4.6 dB higher than that of LEO-based modulators. We further show that the SFDR of silicon depletion-based modulator can be further improved by optimizing the embedded diode structure to 5.9 dB higher than that of LEO-based modulators. We also experimentally demonstrate the transmission of LR SSB-ROF signals at speed of 1 Gb/s by a silicon injection-based ring modulator. The analytical and experimental results in this chapter show that silicon-based modulators have good potential to be used in analog optical links. Silicon depletion based MZI modulators provide better linearity than LEO based MZI modulators. Silicon microring modulators provide an effective way to generate a SSB- ROF signal through its unique narrow-band characteristic.

### **Chapter 3: Novel Diode Structures and T-Rail Travelling-Wave Electrodes to Enhance the Performance of Depletion-based Modulators**

As shown in table 1.7, silicon modulators based on free-carrier effect commonly employ three different electrical structures: (1) carrier-injection in the p-i-n diode, (2) carrier-depletion in the p-n diode and (3) carrier-accumulation in the MOS capacitor.

Among these structures, carrier depletion-based modulators demonstrate the highest modulation speed because of following reasons: (a) compared to carrier-injection modulators in a pin diode, carrier depletion-based modulators exhibit much shorter carrier transit time in the order of picoseconds, while the carrier lifetime is typically longer than nanosecond in the injection-based device [27]. (b) Compared to carrier-accumulation in the MOS capacitor, the capacitance of the carrier depletion-based modulator is much reduced, hence a higher RC bandwidth [28].

In terms of fabrication complexity, carrier injection-based modulators require the simplest fabrication of a p-i-n diode. Carrier depletion-based modulators require more complicated fabrication processes as a doped region should be precisely defined in the waveguide in order to achieve high modulation efficiency. Among all structures, carrier accumulation-based modulators are the most complicated devices, MOS capacitor-based modulator typically require precise control of the regions of highly doped polysilicon and gate oxide in order to avoid excess optical loss and maintain high modulation efficiency.

By considering the speed limitation and fabrication complexity, carrier depletion-based modulators are a promising structure to achieve high-speed modulation with moderate fabrication complexity in the SOI-based PIC platform. However, there are two major figure-of-merits in depletion-based modulators that can be improved with further device optimization: (i) modulation efficiency and (ii) electrical bandwidth which is limited by the resistance-capacitance (RC) time limit.

Modulation efficiency can be described by the figure-of-merits  $V_{\pi}L$  (normally used in interferometer based modulator) or refractive index change  $\Delta n$  under applied voltage ( $V_{\pi}L$  is related to  $\Delta n$ ). The modulation efficiency of a modulator is higher when the value of  $V_{\pi}L$  is smaller ( $\Delta n$  is higher).  $V_{\pi}L$  is defined as the product of required phase shifter length  $L$  and applied voltage  $V$  in order to achieve complete modulation in MZI. The value of  $V_{\pi}L$  is governed by the amount of  $\Delta n$  under applied voltage  $V$  as required phase shifter length  $L = \lambda/2\Delta n$  for single-arm drive MZI modulator (the value of  $L$  is half in push-pull MZI modulator).

Modulation efficiency of depletion-based modulators is mainly governed by the structural designs of the optical waveguide and the embedded diode. Because the optical waveguide in the SOI-based PIC platform has limited ranges of dimensions to maintain single mode propagation and achieve high integration density, the embedded diode design optimization becomes the most effective way to enhance the modulation efficiency.

The electrical bandwidth of depletion-based modulators is limited by the RC time constant of the depletion-mode diode rather than the carrier transit time ( $\sim$ ps) [11]. Depending on the p-n diode design, the 3dB RC bandwidth is around few GHz assuming a 3 mm-long phase shifter in a RF system with impedance of 50  $\Omega$  (with

diode capacitance per unit length of  $0.3 \text{ fF}/\mu\text{m}$ ,  $RC \text{ bandwidth} = 1/2\pi RC$ ). Thus, a travelling-wave electrode design is needed to achieve both high-speed and large-extinction-ratio operation.

In this chapter, we propose a novel diode design structure to increase the modulation efficiency of the depletion-based modulator. Section 3.1 discusses the basic requirements of the diode design. Section 3.2 presents the design principle of the p-n diode. Section 3.3 shows the modeling results of our proposed device. Section 3.4 describes the fabrication process of our devices. Section 3.5 shows the experimental results of the fabricated devices. Section 3.6 presents our proposed design of travelling wave electrode. Finally section 3.7 summarizes the chapter.



### 3.1 Requirements of Diode Design for Depletion-based Optical Modulators

The modulation efficiency (described by  $V_{\pi}L$  or  $\Delta n$  under applied voltage) in depletion-based modulators is at least one order lower than that in injection-based modulators (0.036 Vcm [29]) because only small amount of free-carriers can be modulated by reverse-bias compared with carrier-injection and carrier-accumulation.

There are several advantages by improving the modulation efficiency. The device's footprint and/or drive voltage can be reduced. Therefore the device integration density can be increased and the power efficiency (switching energy =  $CV^2$  [35]) can be increased (for a given device capacitance). These two advantages are crucial for on-chip interconnects as optical modulators takes up most part of the power consumption in the optical interconnects [56, 57].

From the empirical relations of  $\Delta n$  and  $\Delta\alpha$  in silicon at wavelength of 1.55  $\mu\text{m}$  described in equations 1.4.1 and 1.4.2, one may state the increase of modulation efficiency ( $\Delta n$ ) would also increase the insertion loss of the device by Kramers-Kronig relation. However, the above statement is not completely correct because the insertion loss is a product of device length and loss coefficient. The decrease of required device length by increasing  $\Delta n$  could possibly compensate the increase of  $\Delta\alpha$ . We describe the concept with following equations. Equation 3.1.1 describes the required length  $L$  in a one-arm-drive MZI-based modulator:

$$L = \frac{\lambda}{2 \Delta n} \quad (3.1.1)$$

where  $\lambda$  is the free-space wavelength,  $\Delta n$  is the refractive index change.

The insertion loss (in dB) in the same configuration and assuming both arms are embedded with the same diode structure is:

$$\begin{aligned}
\text{Loss (in dB)} &= 4.343\alpha L \\
&= \frac{4.343\alpha\lambda}{2\Delta n}
\end{aligned} \tag{3.1.2}$$

where  $\alpha$  is the loss coefficient (in  $\text{length}^{-1}$ ) induced by the embedded diode.

From equation 3.1.2, the loss is proportional to  $\alpha$  and inversely proportional to  $\Delta n$ . So it is possible to have a diode design to increase modulation efficiency and maintain (or even decrease) the insertion loss.

However, in depletion-based modulators, the position of the depletion region should be precisely controlled. A wrong design or misalignment of the depletion region would decrease the modulation efficiency with the same (or even higher) insertion loss as the doping level inside the waveguide is the same.

Based on the analysis above, we find that an optimized diode design could provide better modulation efficiency and lower insertion loss. In addition to these requirements, we are also interested for a diode design with high fabrication tolerance. The primary reason is that our previous designs on depletion-based modulators all failed to provide modulation under reverse-bias. One possible reason is the relatively low fabrication tolerance of the  $p^+-i-p-i-n^+$  diode structure. The second reason is that misalignment error is an engineering problem on the fabrication of depleted based modulators. Only few approaches [58] have been proposed to solve this problem, but these approaches may sacrifice the modulation efficiency.

Finally in here, we list the three basic requirements for our diode design: (1) high modulation efficiency, (2) low carrier induced absorption loss and (3) high fabrication tolerance.

### 3.2 Diode Design Principle

First, we calculate the refractive index changes and absorption coefficient changes for free-holes and free-electrons based on the empirical relations of  $\Delta n$  and  $\Delta\alpha$  in equation 1.4.1 and 1.4.2. Figure 3.2.1 shows the calculated results of refractive index changes, loss coefficient changes (dB/mm), and ratio between the refractive index changes by free holes and free electrons. The carrier concentrations are from  $10^{17}/\text{cm}^3$  to  $10^{19}/\text{cm}^3$ .

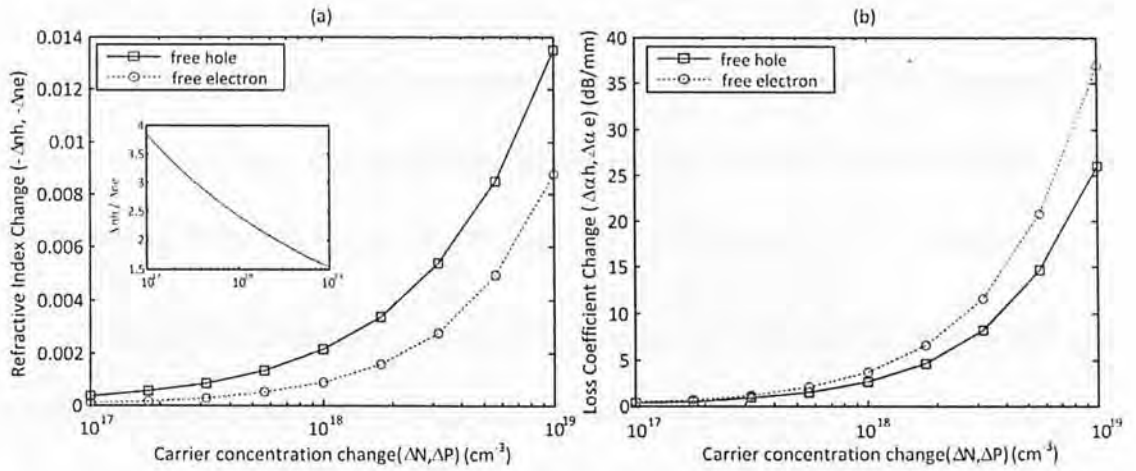


Fig. 3.2.1 (a) Calculated refractive index changes of free-holes and free-electrons. Inset: the ratio of  $\Delta n_h / \Delta n_e$  (b) Calculated loss coefficient changes of free holes and free electrons, with unit of (dB/mm).

From figure 3.2.1, the refractive index changes induced by free-holes are larger than that by free-electrons for carrier concentration change below  $10^{19}/\text{cm}^3$ . At concentration change of  $10^{18}/\text{cm}^3$ , the index change due to free-holes is 2.5 times larger than that due to free-electrons. From the calculated loss coefficient change, the loss induced by free-holes is less than that by free-electrons. The results suggest that the injection or depletion of free holes would be more efficient and provide less loss. This is the major objective for the design on  $p^+i\text{-}p\text{-}i\text{-}n^+$  diode structure to only deplete free-holes in the waveguide [31].

In carrier effect, the increase of free-carrier concentrations would increase the refractive index change. However, the increase of doping concentrations in depletion-based modulators may not always increase the refractive index changes because the change of free-carriers upon reverse-bias is only limited to the depletion region. The depletion width  $W_D$  is related to the doping concentration as described by equation 3.2.1 [59]:

$$W_D = \sqrt{\frac{2\epsilon_0\epsilon_r(V_{bi}+V_{app})}{e} \left(\frac{N_A+N_D}{N_A N_D}\right)} \quad (3.2.1)$$

where  $\epsilon_0$  is the permittivity of free space,  $\epsilon_r$  is the relative permittivity of material,  $V_{bi}$  is the built-in voltage,  $V_{app}$  is the applied reverse bias,  $e$  is the electron charge,  $N_A$  is the p-doping (acceptor) concentration,  $N_D$  is the n-doping (donor) concentration.

Figure 3.2.2 shows the calculated depletion width  $W_D$  as a function of different p and n doping concentration calculated from equation 3.2.1.

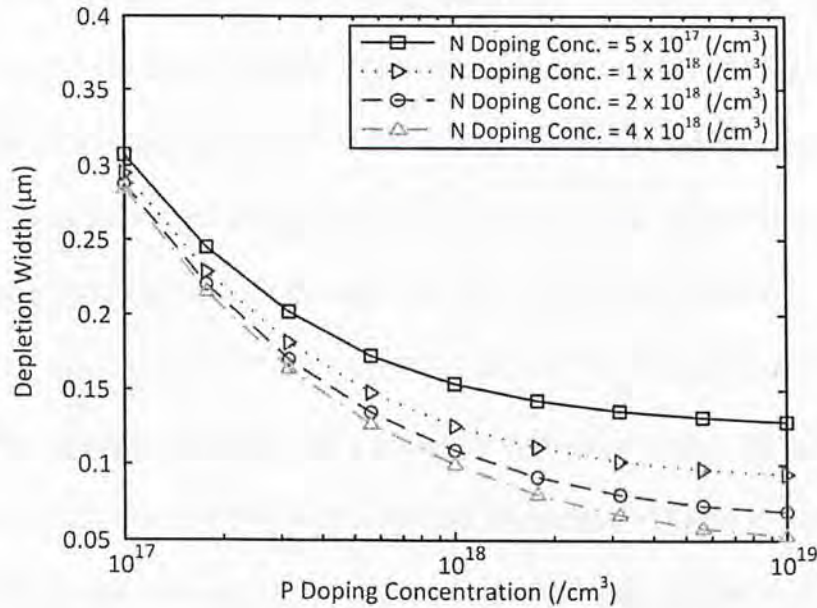


Fig. 3.2.2 Calculated depletion widths as a function of doping concentrations



The value of  $\epsilon_o$  is  $8.854 \times 10^{-14}$  F/cm,  $\epsilon_r$  is 11.9 for silicon,  $V_{bi}$  is assumed to be 1 V,  $V_{app}$  is set to be 5V,  $e$  is  $1.6 \times 10^{-19}$  C,  $N_A$  is ranged from  $10^{17}$  /cm<sup>3</sup> to  $10^{19}$  /cm<sup>3</sup> and  $N_D$  is ranged from  $5 \times 10^{17}$  /cm<sup>3</sup> to  $4 \times 10^{18}$  /cm<sup>3</sup>.

From the results in figure 3.2.2, when  $N_A$  and  $N_D$  are larger than  $5 \times 10^{17}$  /cm<sup>3</sup>,  $W_D$  is less than 200 nm. When  $N_A$  and  $N_D$  are larger than  $1 \times 10^{18}$  /cm<sup>3</sup>,  $W_D$  is less than 130 nm. When we review the experimentally demonstrated depletion-based modulator diode structures by various research groups, the horizontal p-n junctions are widely employed in depletion based modulators [30, 31, 33, 58], due to the simple process of embedding a p-n junction in a formed waveguide in the fabrication. The horizontal p-n junction is defined perpendicular to the wafer plane. As such, the depletion region of the p-n diode can only occupy less than 50% of the area in the waveguide core, compared to the optical waveguide on the SOI platform with a width of 500 nm.

Figure 3.2.3 (a) shows the cross-sectional schematic of an optical waveguide on SOI substrates and the corresponding calculated TE-mode field profile. The waveguide is 220 nm high, 500 nm wide with a 50 nm thick slab. Figure 3.2.3 (b) shows the cross-sectional schematic of the waveguide-embedded horizontal junction. Figure 3.2.3 (c-e) shows the cross-sectional schematics of the dimensions of depletion width inside an optical waveguide with various doping concentration. The doping concentrations are  $N_A, N_D = 5 \times 10^{17}$  /cm<sup>3</sup>,  $N_A, N_D = 1 \times 10^{18}$  /cm<sup>3</sup> and  $N_A, N_D = 2 \times 10^{18}$  /cm<sup>3</sup>. The calculated depletion width under 5V reverse bias are (c) 180 nm, (d) 125 nm and (e) 90 nm. Figure 3.2.3 (f-h) shows the lateral-direction TE-mode field profile of the waveguide in the core region at 110 nm high above the oxide cladding and the depletion width, in order to show the modal overlap between the optical mode and depletion region. We assume a depletion region is located at the middle of the waveguide to achieve maximum efficiency.

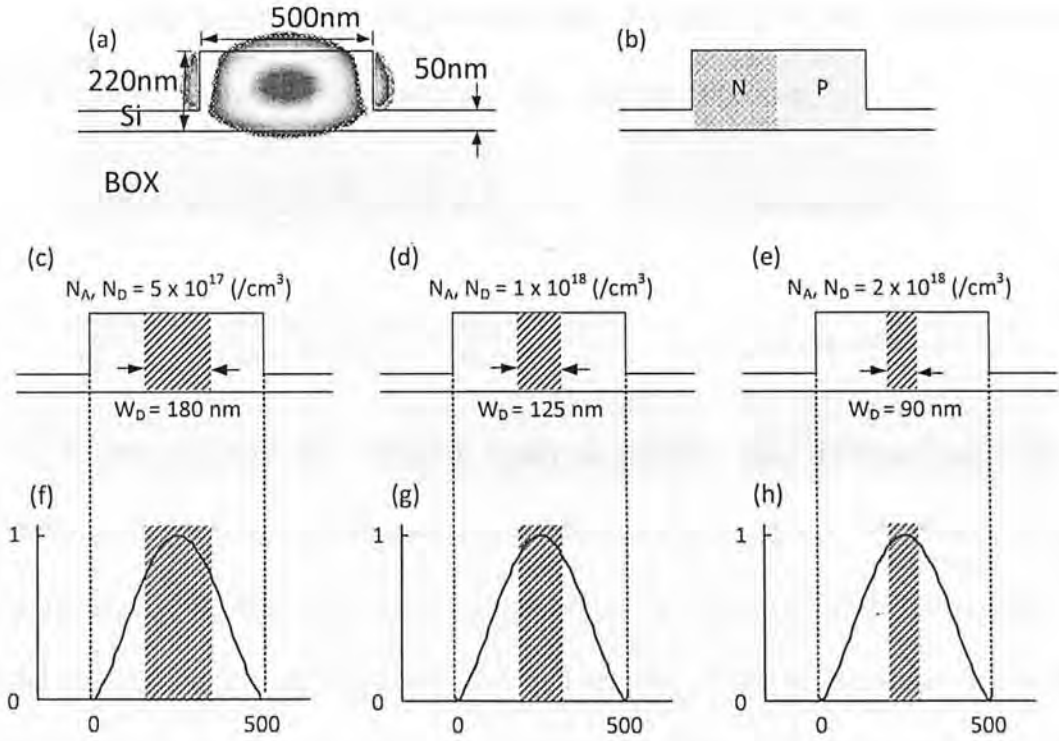


Fig. 3.2.3 (a) Cross-sectional schematic of the optical waveguide and optical-TE mode field distribution. (b) Cross-sectional schematic of the horizontal junction p-n diode in the waveguide. (c-e) Cross-sectional schematics of the dimensions of depletion width inside an optical waveguide with various doping concentrations. The doping concentrations are  $N_A, N_D = 5 \times 10^{17} / \text{cm}^3$ ,  $N_A, N_D = 1 \times 10^{18} / \text{cm}^3$  and  $N_A, N_D = 2 \times 10^{18} / \text{cm}^3$ . The calculated depletion width under 5V reverse-bias are 180 nm, 125 nm and 90 nm. (f-h) Lateral-direction TE-mode field profiles of the waveguide in the core region at 110 nm high above the oxide cladding and the depletion width.

From figure 3.2.3, we see the spatial overlap between the depletion region and the optical mode field decreases with the doping concentrations increase. The results indicate that the modulation efficiency under carrier-depletion would not follow as suggested in figure 3.2.1(a) because of the narrowing of the depletion width. The total refractive index change of the waveguide in depletion-based modulators is based on the weighted average of the total mode field intensity.

In a free-carrier effect without the limit of depletion region, the increase of refractive index change for free-holes and free-electrons become:

$$\frac{\Delta n_h(N_{A2})}{\Delta n_h(N_{A1})} = \frac{-8.5 \times 10^{-18} (N_{A2})^{0.8}}{-8.5 \times 10^{-18} (N_{A1})^{0.8}} = \left( \frac{N_{A2}}{N_{A1}} \right)^{0.8} \quad (\text{for holes}) \quad (3.2.2)$$

$$\frac{\Delta n_e(N_{D2})}{\Delta n_e(N_{D1})} = \frac{-8.8 \times 10^{-22} (N_{D2})}{-8.8 \times 10^{-22} (N_{D1})} = \frac{N_{D2}}{N_{D1}} \quad (\text{for electrons}) \quad (3.2.3)$$

In the case that the depletion width is narrower than 180 nm, the E-field normalized intensity has a peak normalized intensity exceeding 0.8. We assume the E-field intensity is the same as in the depletion region in order to simplify the analysis as modal integration is not necessary. To include the effect of depletion width on depleted-based modulators, we simply multiply the ratios of depletion width and waveguide width to the equations for various concentrations. We also assume that the free-carriers inside the depletion region are fully depleted and  $N_A$  is equal to  $N_D$ . The increase of refractive index change in depletion-based modulators for free-holes and free-electrons become:

$$\frac{\Delta n_h(N_{A2})}{\Delta n_h(N_{A1})} = \frac{-8.5 \times 10^{-18} (N_{A2})^{0.8} (W_{D2})}{-8.5 \times 10^{-18} (N_{A1})^{0.8} (W_{D1})} = \left( \frac{N_{A2}}{N_{A1}} \right)^{0.8} \quad (\text{for holes}) \quad (3.2.4)$$

$$\frac{\Delta n_e(N_{D2})}{\Delta n_e(N_{D1})} = \frac{-8.8 \times 10^{-22} (N_{D2}) (W_{D2})}{-8.8 \times 10^{-22} (N_{D1}) (W_{D1})} = \left( \frac{N_{D2}}{N_{D1}} \right)^{0.5} \quad (\text{for electrons}) \quad (3.2.5)$$

In equations 3.2.4 and 3.2.5, our analysis shows that in depletion-based modulators, a ten times increase of p-doping concentration  $N_A$  can only provide 2 times increase in the refractive index change, while ten times increase of n-doping concentration  $N_D$  can only provide 3 times increase in the refractive index change. However, the loss coefficient depends little on the depletion width because normally the entire waveguide region is doped with dopants. Due to this reason, in depletion-based modulator, a doping concentration of less than  $2 \times 10^{18} / \text{cm}^3$  is normally used to

avoid larger absorption. On the other hand, the narrower depletion width for a higher doping concentration requires more precise control on the forming of the doped regions, which may at the end result in a lower-efficiency modulator after the fabrication.

Our analysis showing the changing of the doping concentration provides little enhancement on the modulation efficiency due to the limited spatial overlap between the optical mode and the depletion region. So in order to increase the modulation efficiency, we consider a vertical junction p-n diode to increase the modulation efficiency in our diode design. The vertical junction is defined as the p-n junction is parallel to the wafer plane. The vertical-junction p-n diode would increase the modal overlap in the typical rectangular waveguide geometry.

Figure 3.2.4 (a) shows the cross-sectional schematic of the vertical-junction p-n diode in the waveguide. Figure 3.2.4 (b) shows the cross-sectional schematic of the dimension of the depletion region inside the optical waveguide. We assume  $N_A, N_D = 1 \times 10^{18} / \text{cm}^3$ . Figure 3.2.4 (c) shows the vertical direction TE mode field profile at the center of the waveguide, in order to show the modal overlap between the optical mode and the depletion region. The waveguide dimension is the same as that in figure 3.2.3.

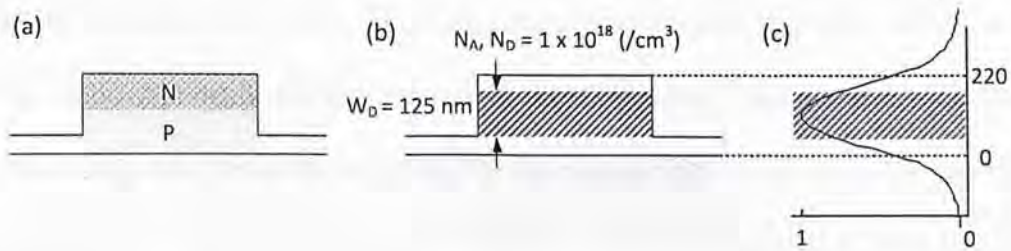


Fig. 3.2.4 (a) Cross-sectional schematic of the vertical-junction p-n diode in the waveguide. (b) Cross-sectional schematics of the dimension of depletion region inside the optical waveguide.  $N_A, N_D = 1 \times 10^{18} / \text{cm}^3$ . (c) Vertical direction TE mode field profile at the center of the waveguide.



With the vertical p-n junction, the depletion region occupies nearly 60% of the area in the waveguide core, while in the horizontal junction the depletion region occupies only 25% of the area with the same doping concentrations of  $N_A, N_D = 1 \times 10^{18} \text{ /cm}^3$ . The results show that the vertical junctions approximately increase the modulation efficiency by two times with similar loss coefficient with the same p- and n- doping concentrations.

In summary, we provide the principle for designing depletion-based modulators. First, we derive the relation between the modulation efficiency and the loss, showing that the increase of the modulation efficiency could mitigate the effect of loss coefficient increasing due to higher carrier concentration. Second, we show the increase of the doping concentration provides little enhancement in the modulation efficiency but results in higher loss and lower fabrication tolerance. Based on these principles, we propose to use a vertical-junction p-n diode in our design in order to optimize the modulation efficiency and insertion loss of the modulator. This fulfills the first two requirements listed in section 3.1.

For the requirement on fabrication tolerance, the vertical junction allows us to use the energy control during the ion implantation process to give a better control on the position of the p-n junction. Therefore, the p-n junction is no longer relying on the doping windows, which always suffer from the alignment problems and imperfection of photolithography. In our fabrication, the existing overlay accuracy is 100 nm (mean + 3sigma) of the i-line stepper in NFF (HKUST). While the energy control of the ion implanter has variation of less than 1% in commercial product line [60], which gives a projected range of less than 10 nm variation. The above information shows that our approach here may provide a more robust fabrication tolerance.

### 3.3 Modeling Results of Vertical-Junction p-n Diodes

First, we calculate the refractive index changes and loss coefficient changes for horizontal- and vertical- junction by finite-element-method. As the simulations include the mode integration and realistic doping profile, the accurate results can help proof our concepts above. Also, the diode structures used in the simulation share similar fabrication steps and are possible for us to fabricate.

Figure 3.3.1 shows the calculated doping profiles for horizontal-junction and vertical-junction p-n diodes in an optical waveguide by using Athena. The optical waveguide is 340 nm high, 500 nm wide with 140 nm thick slab. The diodes share the same ion implantation dosages, the peak concentration for p-doped and n-doped region are around  $1 \times 10^{18} / \text{cm}^3$ . In our designed vertical-junction p-n diodes, an additional horizontal junction is formed near the  $n^+$  slab region to provide a conductive path for the free electrons to deplete from the p-n junction.

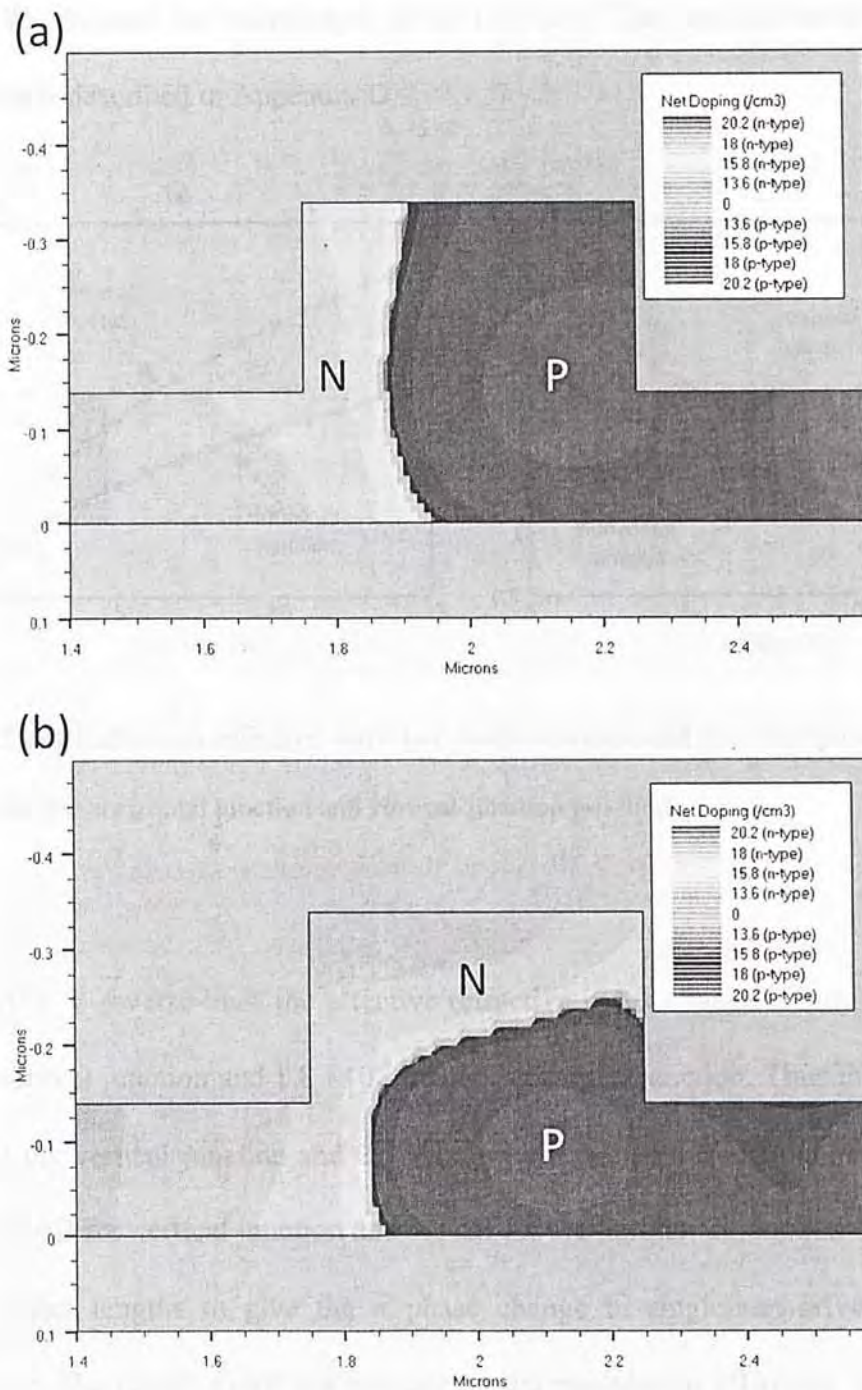


Fig. 3.3.1 Simulated doping profiles of the (a) horizontal-junction and (b) vertical-junction p-n diodes embedded into the optical waveguide. The profiles are simulated by Athena.

Figure 3.3.2 shows the calculated effective refractive index changes and absorption coefficient changes for the horizontal-junction and vertical-junction p-n

diodes. We assume the wavelength is at 1.55  $\mu\text{m}$ . The detailed methodology of simulation is described in Appendix D.

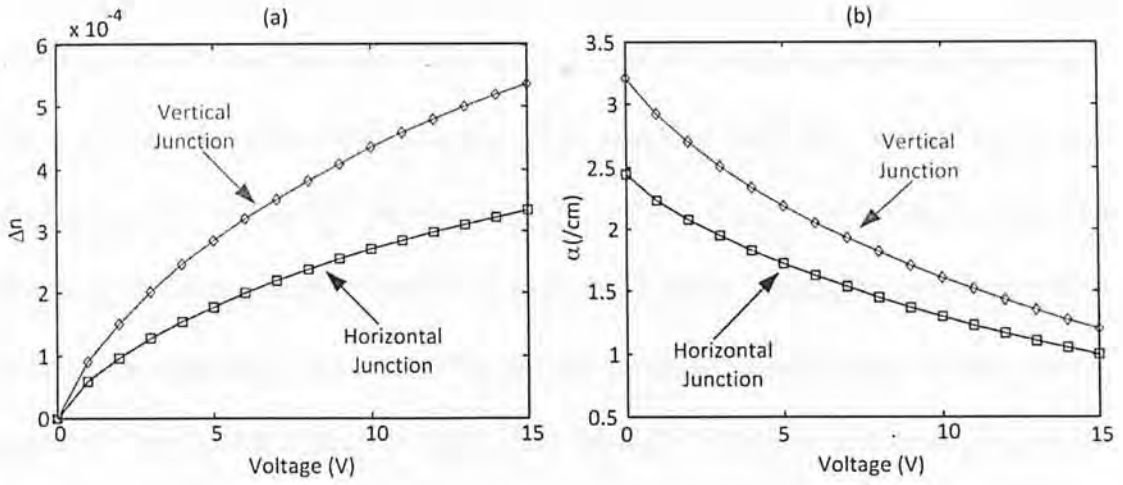


Fig. 3.3.2 (a) Calculated effective refractive index changes and (b) absorption coefficient changes for the horizontal junction and vertical-junction p-n diodes.

At 5 V reverse-bias, the effective refractive index change is around  $2.8 \times 10^{-4}$  for the vertical junction and  $1.8 \times 10^{-4}$  for the horizontal junction. Thus the  $V_{\pi}L$  is 1.4 Vcm for the vertical junction and 2.2 Vcm for the horizontal junction. The insertion loss is 3.1 dB for vertical junction and 3.8 dB for the horizontal junction assuming the phase shifter lengths to give the  $\pi$  phase change in single-arm-drive MZI-based modulator. The results proof our concept on the modulation efficiency enhancement and loss reduction by employing vertical junctions.

The modulation efficiency has 40% enhancement in the calculated results. The waveguide dimensions used in the analysis are defined by considering a simple fabrication process on 340 nm thick top silicon SOI wafer. The ratio of width to height is around 1.5, compared to waveguide with height of 220 nm (width/height = 2.3), the aspect ratio is 50 % smaller. Therefore, we believe that a 220 nm high



waveguide may have even higher efficiency. Our calculated results on 220 nm high, 500 nm width waveguide dimensions show that effective refractive index change is around  $4.5 \times 10^{-4}$  for the vertical junction and around  $2.1 \times 10^{-4}$  for the horizontal junction under 5 V reverse bias. Thus the  $V_{\pi}L$  is 0.9 Vcm for the vertical junction and 1.8 Vcm for the horizontal junction. The insertion loss due to the free-carrier absorption is 3 dB for the vertical junction and 4.6 dB for the horizontal junction assuming the phase shifter lengths to give the  $\pi$  phase change in single-arm-drive MZI-based modulator. The doubling of the modulation efficiency of the vertical junction compared to that of the horizontal junction is because of the doubling in the modal spatial overlap.

In order to investigate the effect of alignment error during the fabrication, we perform simulations on various doping windows. Figure 3.3.3 shows the cross-sectional schematics of the p-doped and n-doped ion implantation window on top of the silicon waveguide during the process. The center of the waveguide is defined as  $X = 2.00 \mu\text{m}$ . The edges of doping windows on the waveguide are originally  $0.15 \mu\text{m}$  apart from the center. The center of edge of p-doping window on the waveguide is defined as  $X = 1.85 \mu\text{m}$ . The center of edge of n-doping window on the waveguide is defined as  $X = 2.15 \mu\text{m}$ .

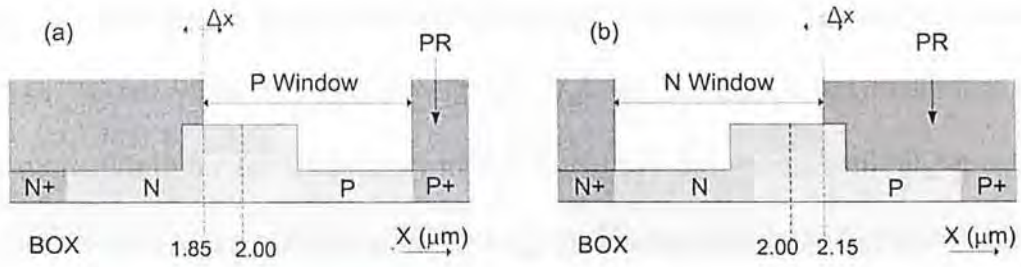


Fig. 3.3.3 Cross-sectional schematics of the ion implantation windows for (a) p-doping and (b) n-doping. The center of the waveguide is defined as  $X = 2.00 \mu\text{m}$ . The doping windows are  $0.15 \mu\text{m}$  apart from the center. The center of edge of p-doping window on the waveguide is defined as  $X = 1.85 \mu\text{m}$ . The center of edge of n-doping window on the waveguide is defined as  $X = 2.15 \mu\text{m}$ .

Figure 3.3.4 shows the calculated  $V_{\pi}L$  as a function of the doping window variations. The diode structure and doping concentration are the same as those in figure 3.3.1 (b). We calculated the  $V_{\pi}L$  by calculated effective refractive index change  $\Delta n$ :

$$V_{\pi}L = \frac{5\lambda}{2\Delta n} \quad (3.3.1)$$

where  $\Delta n$  is the effective refractive index change under 5 V reverse-bias.

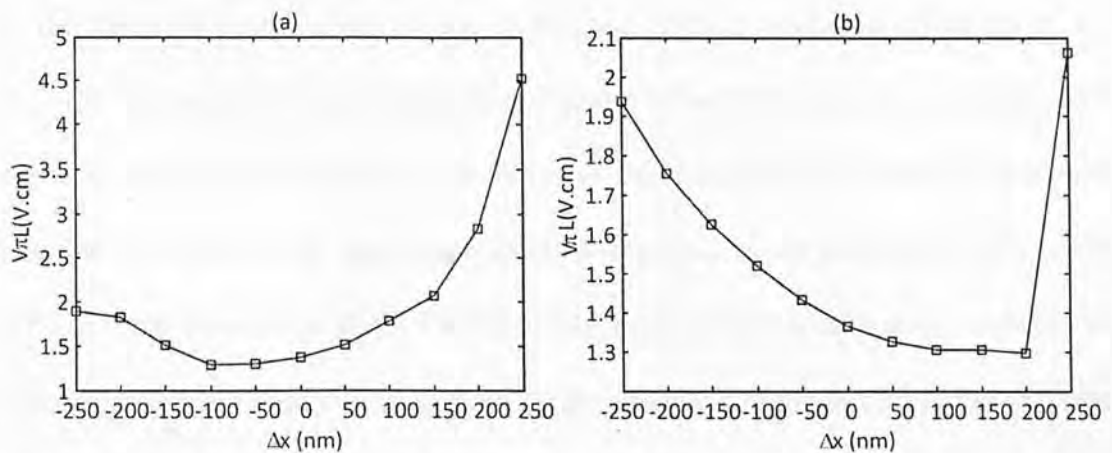


Fig. 3.3.4 Calculated  $V_{\pi}L$  as a function of (a) p- and (b) n- doping window variations.

From figure 3.3.4, the calculated results show that for the p-doping window with  $\pm 100$  nm window misalignment, the  $V_{\pi}L$  of the device has maximum 30% variation. While for the n-doping window with  $\pm 100$  nm window misalignment, the  $V_{\pi}L$  of the device has maximum 11% variation. The reason for the higher variation in the p-doping window is because the diode structure is optimized for the depletion of free-holes instead of free-electrons. The efficiency can be further improved if we move the doping window to the edges of the waveguide. However, it suffers from the risk that we may disconnect the electrical path way of the carriers, resulting in a hugely decrease of the modulation efficiency (e.g. shown in figure 3.3.4 (a) when  $\Delta x$  is -250 nm and in figure 3.3.4 (b) when  $\Delta x$  is 250 nm). The results here show our designs fulfill the requirement of fabrication tolerance.

Although our vertical-junction diode design can give better modulation efficiency, lower loss and high fabrication tolerance, the capacitance of the device is much higher compared to the horizontal junction due to the increased area of the diode. In both 220 nm and 340 nm high waveguides, the calculated capacitance per unit length at 2.5 V reverse bias voltage is 0.5 fF/ $\mu\text{m}$  for vertical junction and 0.25 fF/ $\mu\text{m}$  for horizontal junction by Atlas. The doubled capacitance can be compensated as the required length is halved due to increase of the modulation efficiency in 220 nm high waveguide. But the doubled capacitance of vertical junction p-n diode in 340 nm high waveguide results in a decrease of RC bandwidth compare to horizontal junction p-n diode in the same waveguide dimensions as the required length is only 70% of the horizontal junction. The relatively high doping concentrations between the anode and cathode lead to a calculated series resistance of around 2 k $\Omega$   $\mu\text{m}$  by Atlas. The device RC bandwidth ( $1/2\pi RC$ ) is thus over 50 GHz. However, in a RF system with impedance of 50  $\Omega$ , for the modulator with the required phase shifter length to



achieve  $\pi$  phase change, the RC bandwidth of the modulator is around 4 GHz. A shorter phase shifter length can be used to achieve high-speed modulation, however, the extinction ratio would also decrease. A capacitive-loaded travelling-wave electrode is thus a promising engineering solution to solve this problem. We will discuss this in section 3.6.

We simulate more than 80 diode structures to optimize the diode design in order to achieve best performance and balance the modulation efficiency and insertion loss. The parameters have been fine-tuned including the doping windows, the ion implantation energy (p-n junction position), the ion implantation dosages (doping concentrations) and the thermal annealing temperature. In our designs, the p-n junction is placed slightly higher than the middle of waveguide to form an asymmetric p-n diode, in order to maximize the spatial overlap between the change of free-holes concentration and the peak intensity of the TE mode field.

Figure 3.3.5 (a) shows the cross-sectional schematic of an optical waveguide on SOI substrates and the corresponding calculated TE-mode field profile. The waveguide is 340 nm high, 500 nm wide with a 140 nm thick slab. Figure 3.3.5 (b) and (c) shows the simulated free-hole and free-electron concentration changes in the waveguide core region upon 5 V reverse bias in the same waveguide dimensions. The diode structure and doping concentration are the same as those in figure 3.3.1 (b).



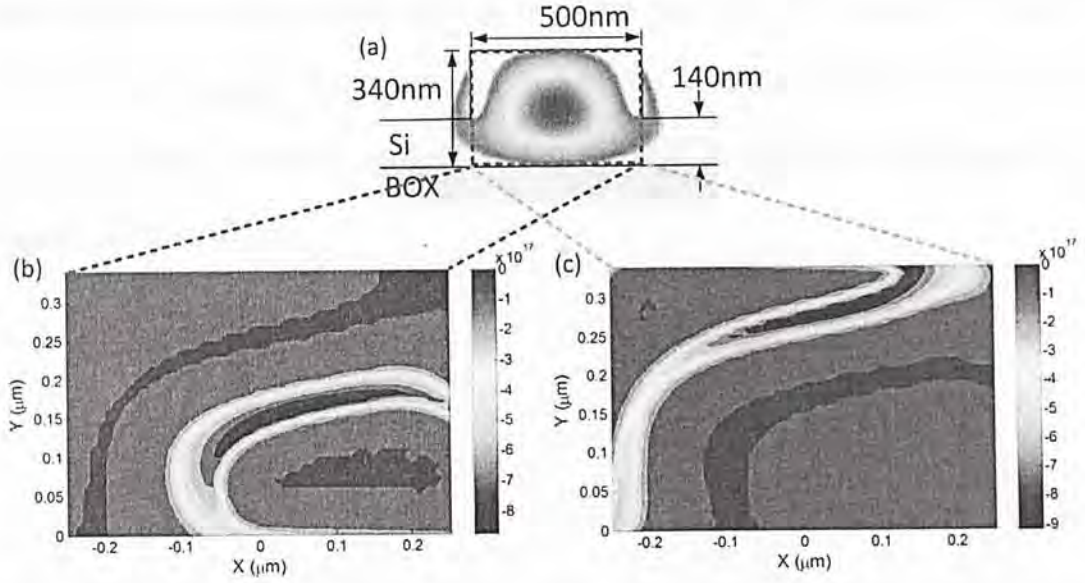


Fig. 3.3.5 (a) Cross-sectional schematic of an optical waveguide on SOI substrates and the corresponding calculated TE-mode field profile. The waveguide is 340 nm high, 500 nm wide with a 140 nm thick slab. (b-c) Simulated (b) hole and (c) electron concentration changes in the waveguide core region upon 5 V reverse bias in a 340 nm high waveguide.

From figure 3.3.5, the hole concentration change is spatially overlap with the peak intensity of TE the mode field, while the electron concentration change is at the region with a lower intensity. The maximum hole concentration change is around  $9 \times 10^{17} / \text{cm}^3$ . The maximum electron concentration change is also around  $9 \times 10^{17} / \text{cm}^3$ .

In our final diode designs, the modulation efficiency is 1.4 Vcm for 340 nm high waveguide and 0.9 Vcm for 220 nm high waveguide. Our simulated results are compatible with the best reported value so far [35]. The best results so far is also based on a vertical junction p-n diode but based on a waveguide with thicker slab thus less mode confinement, which potentially have larger banding radius and lower integration density compared to the waveguides used in our structures. Also, all the processes used in the simulation are relatively simple and capable for us to fabricate

the device by the clean room facilities in CUHK and HKUST. Finally, we have to fabricate the designed diode structure in 340 nm thick top silicon SOI wafer by ourselves. While the diode designs for 220 nm high waveguide are fabricated by a foundry service oversea.

### 3.4 Fabrication Process of the Silicon Modulator

Our design of silicon depletion-based modulators in 340 nm high waveguide is fabricated by a 'mix-and-match' EBL in MNF/CUHK and i-line photolithography and NFF/HKUST. The step of defining grating couplers is fabricated in CUHK by EBL while other steps are fabricated in HKUST by i-line stepper.

We fabricate the device on a 100 mm (4 inch) SOI wafer with 340 nm top Si on 2  $\mu\text{m}$  thick buried oxide (BOX) purchased from Soitec, Inc.. There are a total of eight lithography steps to define various patterns on the wafer, in addition to an initial alignment mark forming for the i-line stepper. A total of seven masks have been used in the photolithography steps. The fabrication process for the depletion-based modulators is similar to the injection-based modulator as described in chapter 2 in steps 1-4.

In the fifth and sixth steps, the wafer is first coated with HMDS at 105 °C for 60 seconds, and then spin coated with AZ1075 PR at 4000 rpm for 60 seconds. Following a softbake at 90 °C for 60 seconds on hotplate, we transfer the patterns of p- and n- doped region by the ASML-5000 i-line stepper. After the exposure, we bake the resist at 110 °C for 90 seconds on hotplate, and then we develop the wafer by FHD-5 developer for 60 seconds. We hardbake at 120 °C for 30 minutes in oven prior to the ion implantation processes. We then use the Varian CF3000 ion implanter to do ion implantation for the p- and n- doped-regions. We implant boron for p doping, with the dosage of  $5 \times 10^{13} / \text{cm}^2$ , energy of 70 keV, and tilt angle of 7°. We implant phosphorus for n doping, with the dosage of  $2 \times 10^{13} / \text{cm}^2$ , energy of 30 keV, and tilt angle of 7°. After the ion implantations, we remove the resists on top by oxygen



plasma cleaning in PS210 photo resist asher for 25 minutes. The wafer is then cleaned by a standard piranha cleaning at 120 °C for 10 minutes.

After the sixth steps, the 250 Å sacrificial oxide layer is removed from the wafer by buffered oxide etchant (BOE) for 60 seconds, and then re-deposited with 6000 Å thick LTO in the furnace. The 6000 Å oxide act as a upper cladding of the optical waveguide to prevent the loss induced by the modal overlap between the evanescent field and the metal. We then anneal the wafer at 1000 °C for 30 minutes in the furnace. The annealing process provides the functions of dopants activation and LTO densification.

In the seventh step, the pattern of oxide via is defined as the same recipe used in the first step for the photonic devices. After the steps of photolithography, the wafer is wet-etched by BOE solution for 9 minutes to ensure the oxide via are opened through to provide good contact between metal and highly doped region. We then remove the resists by a standard piranha cleaning at 120 °C for 10 minutes. We choose wet etching because of the machine for dry etching was not available during our process.

Finally, in the eighth step, the wafer is first sputtered with 8000 Å thick Al:Si (1%) by the Varian 3180 sputtering system. After the sputtering, the wafer is first coated with HMDS at 105 °C for 60 seconds, and then spin coated with HPR504 PR at 4000 rpm for 60 seconds. Following a softbake at 110 °C for 60 seconds on hotplate, we transfer the patterns of metal contact by the ASML-5000 i-line stepper. After the exposure, we develop the wafer by FHD-5 developer for 60 seconds, and then hardbake at 120 °C for 30 minutes in oven prior to the wet metal etching. We wet-etched the Al/Si on the wafer by a  $\text{H}_3\text{PO}_4:\text{CH}_3\text{COOH}:\text{HNO}_3$  (100:10:1) solution



at 50 °C for 5-6 minutes. After the wet-etching, the wafer is dip in the Freckle etch solution for 2 minutes to remove the silicon residues left on the wafer. We then remove the resists by a MS2001 at 120 °C for 10 minutes. We finally perform FGA at 400 °C for 30 minutes in order to achieve lower contact resistance.

Figure 3.4.1 shows the schematics of the fabrication process flow.

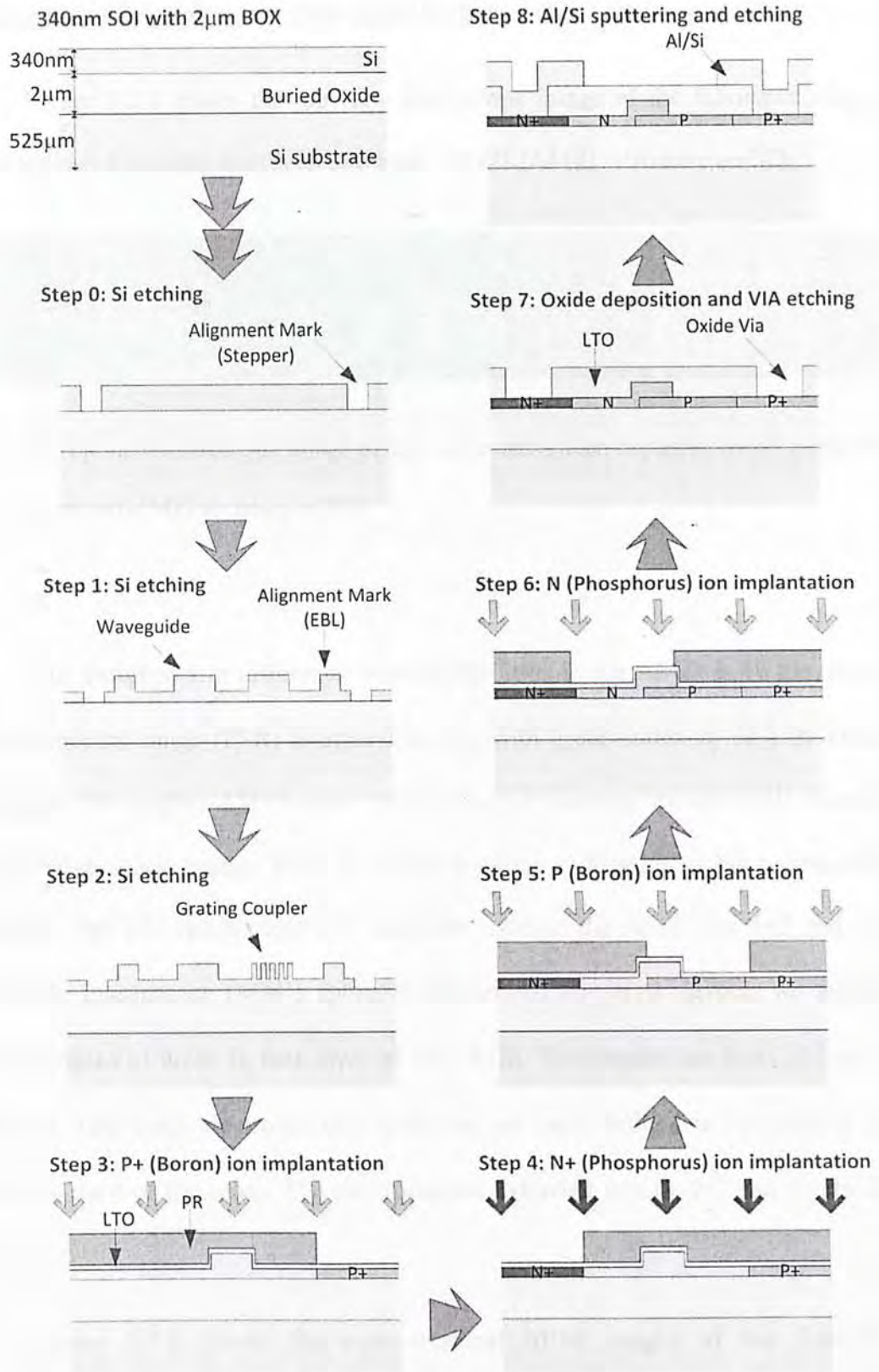


Fig. 3.4.1 Schematics of the fabrication process flow for the silicon depletion-based modulator embedded with a vertical junction  $p^+-p-n-n^+$  diode.

### 3.5 Experimental Results of the Fabricated Devices

Figure 3.5.1 shows the top-view microscope image of the fabricated silicon depletion-based modulator with an asymmetric MZI (AMZI) structure on SOI.



Fig. 3.5.1 Top-view microscope image of the fabricated silicon depletion-based modulator with an asymmetric MZI structure on SOI.

Our designed arm difference between the arms in the AMZI is  $40\text{ }\mu\text{m}$ , hence the free spectral range (FSR) is around  $15\text{ nm}$  with group index  $n_g$  of 4 in silicon waveguide. We employ AMZI as our optical structure because we can easily measure the refractive index change from the shifting of the null point in the transmission spectrum. The  $1\times 2$  splitter and  $2\times 1$  combiner used in the AMZI are  $1\times 2$  and  $2\times 1$  multimode interference (MMI) splitter/combiner. In our mask layout, we employ various lengths of diode in both arms of the AMZI. The lengths are from  $500\text{ }\mu\text{m}$  to  $4000\text{ }\mu\text{m}$ . The metal electrodes and oxide via are only defined in one arm of the AMZI for most of the cases. The electrodes are extended to a G-S-G pad for the RF probing.

Figure 3.5.2 shows the cross-sectional SEM images of the fabricated waveguide and diode-embedded waveguide. The designed dimensions of the waveguide are  $340\text{ nm}$  high,  $500\text{ nm}$  wide and with a  $140\text{ nm}$  thick slab. The designed separation between waveguide sidewall and oxide-via is  $2\text{ }\mu\text{m}$ . The designed



separation between waveguide sidewall and metal electrode is 1  $\mu\text{m}$ . The deposited oxide has not been removed this time for the SEMs.

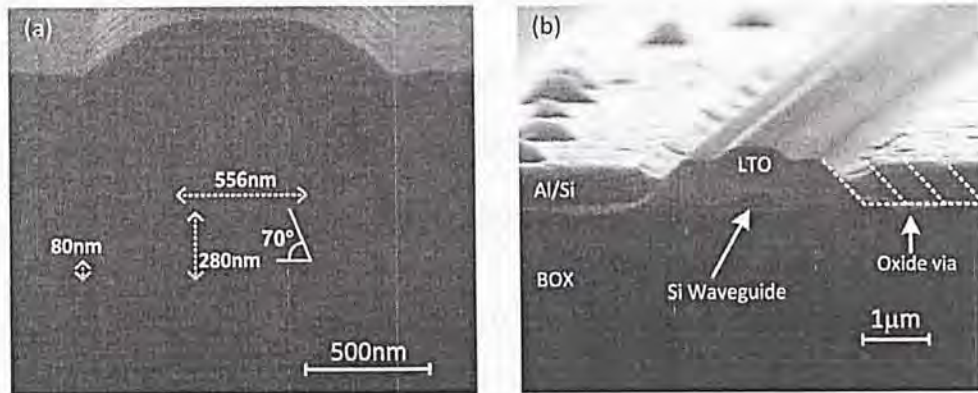


Fig. 3.5.2 (a) Cross-sectional SEM image of the fabricated waveguide. (b) Cross-sectional SEM image of the fabricated diode embedded waveguide.

From figure 3.5.2 (a), the measured waveguide height is only around 280 nm, width is around 550 nm and the slab thickness is around 80 nm. The sidewall slope angle is around 70°. The measured height and slab thickness is 60 nm thinner from our design. The sidewall slope angle is even worse than the results of our previous device discussed in chapter 2. We attribute the deviation to a fabrication error due to plasma cleaning in the process step 2, in which a  $\text{SF}_6$  gas is mixed with oxygen in the oxygen cleaning for 5 minutes. The  $\text{SF}_6$  gas can etch silicon even in a small amount. The fabrication error also leads to the poor sidewall slope angle, as during the oxygen cleaning no resists is used as a mask. Actually, we are aware of the problems after the process as the color of the SOI wafer is changed. We experimentally evaluate the etch depth using in the same recipe by a bulk silicon wafer and subsequently increase the sacrificial oxide thickness in the following process. However, the values measured in the SEM far exceed our expectation and possibly become the main reason for the device failure.



From figure 3.5.2 (b), the oxide via is around 1.4  $\mu\text{m}$  away from the waveguide sidewall. The metal electrode is also around 1.4  $\mu\text{m}$  away from the waveguide sidewall. Both results are consistent with the isotropic etching of 600 nm thick oxide and 800 nm thick Al/Si. The sidewall slope of the oxide is around  $50^\circ$  as wet etching has been used. However the SEM image indicates that the device loss should not be contributed by the metal absorption of the electrodes.

Figure 3.5.3 shows the measured IV characteristic of the fabricated silicon depletion-based modulator with a 1.5 mm long phase shifter. The results are measured by connecting the G-S RF probe to the HP 4145B semiconductor parameter analyzer through a BNC cable to ensure small resistance attributed by the setup. The measured current limitation of the analyzer is set to 10 mA. The turn-on voltage of the  $p^+ - p - n - n^+$  diode is around 0.9 V. The turn-on resistance is around 30  $\Omega$ . The IV characteristic of the device shows typical diode response with low turn-on voltage and low contact resistance. The results indicate a good fabrication processes for the  $p^+$  and  $n^+$  ion implantation, the oxide via and the metal contact layers. However, the turn-on resistance here is 12  $\Omega$  higher than our previously fabricated device (figure 2.3.5), the turn-on voltage also has 0.1 V smaller than in our previous device, which may be contributed by the lower doping concentrations of the  $p^+$  and  $n^+$  regions.

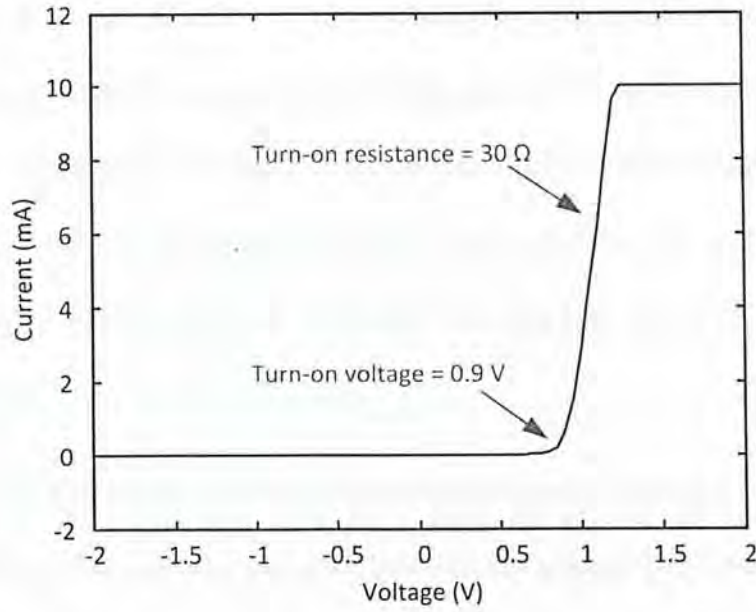


Fig. 3.5.3 Measured IV characteristic of the fabricated silicon depletion-based modulator embedded with a  $p^+p\text{-}n\text{-}n^+$  diode

In optical testing, the setup is similar to the one reported in chapter 2. First, from our testing pattern we observe the grating coupler has a coupling efficiency of lower than 6 dB per each grating. The peak wavelength of the coupler is shifted to 1510 nm. Both reduced coupling efficiency and shifted peak wavelength are not desired. We suppose the poor results are due to bad grating layer etching and the dimension deviation of the waveguide. Second, we also find high optical loss and unusual optical response for most of the devices on the chip. For example, we have more than 20 modulator design layouts with the same optical AMZI structure and slightly different diode structures, but only few of them provide reasonable response. The results are very inconsistent with our testing results for devices fabricated in NFF earlier (see chapter 2). We suppose the poor results are due to fabrication error in oxygen-cleaning process. Also, as the responses in various structures are similar among various dies across the wafer, we believe the masks used in the

photolithography may have some dimension errors compared to our designs, especially for the optical waveguide layer. Third, most of the devices gave fabry-perot responses. The fabry-perot responses in our devices limit our observation of null point shifting of the AMZI to deduce the refractive index changes. We suppose the poor results are due to fabrication error in oxygen cleaning also the error in fabricating grating couplers.

Figure 3.5.4 shows the measured transmission spectrum of the diode-embedded AMZI with 1.5 mm phase shifter without applied DC voltage (0V). The wavelength scan ranged from 1515 nm to 1560 nm. The resolution of the spectrum is 0.05nm. The laser input power is around -3 dBm.

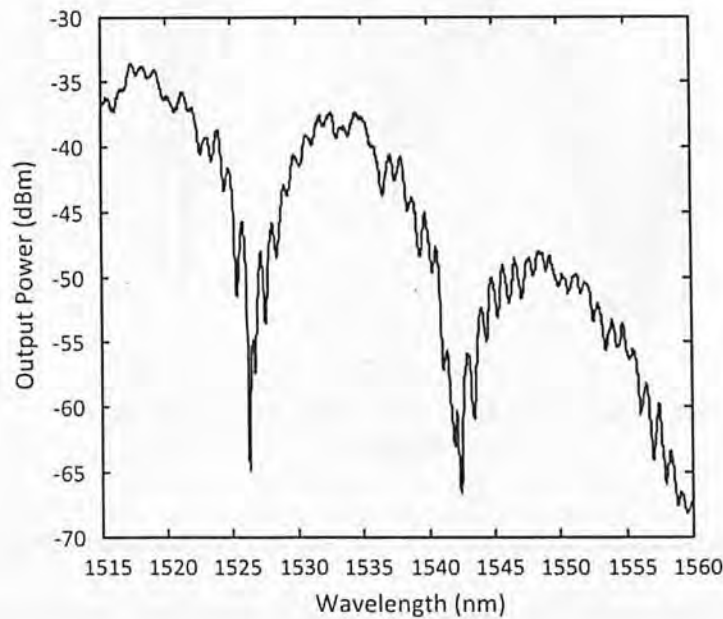


Fig. 3.5.4 Measured transmission spectrum of the diode-embedded AMZI with 1.5 mm phase shifter in waveguide with height of 340 nm without applied DC voltage (0V).

From figure 3.5.4, the maximum output power from the device under test is around -35 dBm. With 12 dB coupling loss and around 1 dB loss in the setup, the loss



of the device is around 22 dB. The measured FSR of the AMZI is around 16 nm, which matches with our design. The FSR of the fabry-perot response is around 1 nm, which we attribute to back-reflection of the grating coupler.

Figure 3.5.5 shows the measured transmission spectra of the diode-embedded AMZI with 1.5 mm phase shifter under various forward bias DC voltages. The device under test here has the same design structure as in figure 3.5.4 but on a different die. The output is normalized with the maximum power in each spectrum. The wavelength scan ranged from 1511 nm to 1550 nm. The resolution of the spectra is 0.05 nm.

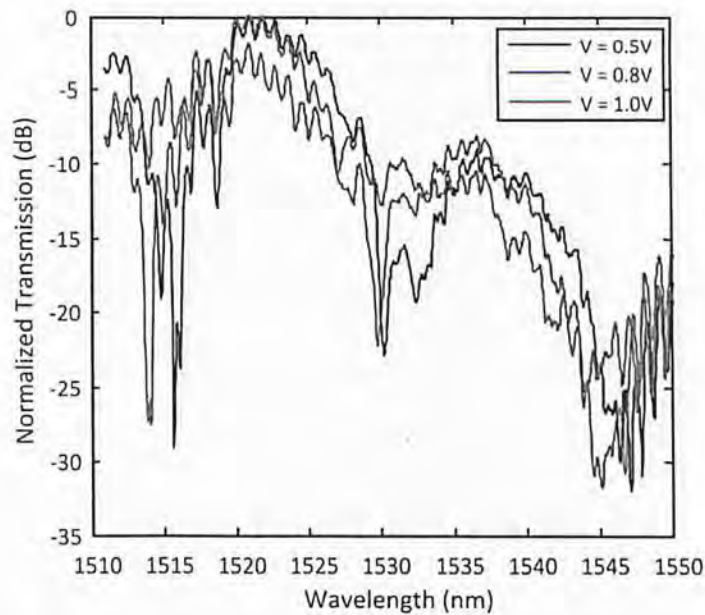


Fig. 3.5.5 Measured transmission spectra of the fabricated depletion-based modulator embedded with a  $p^+-p-n-n^+$  diode in waveguide with height of 340 nm under various forward bias DC voltages.

The null point of the AMZI response is shifted towards shorter wavelength upon forward-bias voltage of 0.8 V, which is an evidence of modulation caused by carrier injection. Upon forward bias voltage of 1.0 V, however, no null point from the



AMZI response has been observed in the spectrum. Because the diode is already turn-on at 1.0V, large amount of free carriers are injected into the waveguide region embedded with the 1.5 mm long phase shifter to attenuate the signal.

Figure 3.5.6 shows the measured transmission spectra of the diode-embedded AMZI with the 1.5 mm phase shifter under various reverse bias DC voltages. The device under test here is the same as that in figure 3.5.5. The output is normalized with the maximum power in each spectrum. The wavelength scan ranged from 1511 nm to 1550 nm. The resolution of the spectra is 0.05 nm.

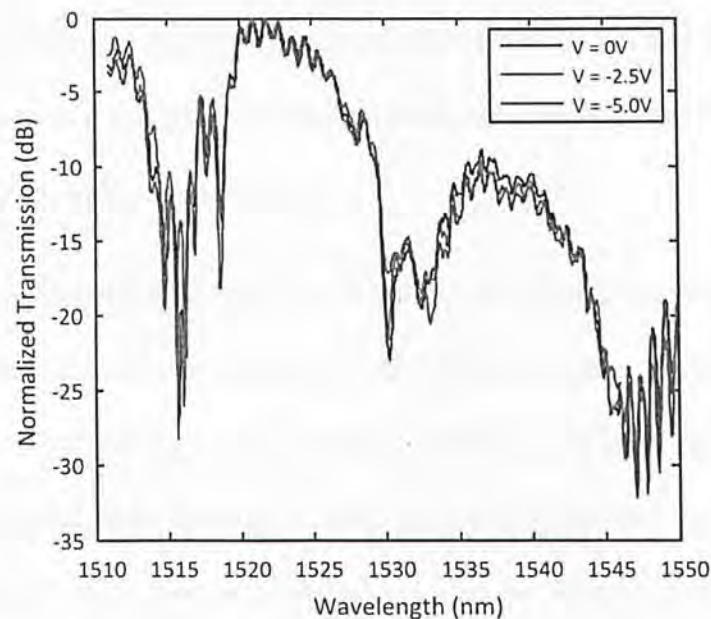


Fig. 3.5.6 Measured transmission spectra of the fabricated depletion-based modulator embedded with a  $p^+-p-n-n^+$  diode in waveguide with height of 340 nm under various reverse-bias DC voltages.

From figure 3.5.6, we cannot observe any shift of the null point when the reverse-bias voltage across the modulator is up to 5 V, which indicates very little amount (if not none) of free carriers have been depleted inside the waveguide core.

As our device shows good IV characteristics and demonstrates the carrier-injection-based modulation, the process steps on  $p^+$  and  $n^+$  ion implantation, oxide via and metal contact layers should be fine and do not influence the device performance. We suspect there are two reasons for no effect of carrier-depletion has been observed: (1) the ion implantation of the moderately p-doped and n-doped regions were not controlled well (2) the waveguide dimension has been hugely changed by fabrication error. The above two reasons are expected not to affect the modulation by carrier-injection significantly as the control of moderately p-doped and n-doped regions are not crucial in carrier-injection-based modulation and there are still 80 nm slab thickness for the electrical path for carrier-injection from the  $p^+$ - and  $n^+$ - regions. Our results also suggest that the depletion-based modulator is more sensitive to fabrication error than the injection-based modulator.

As the ion implantation processes for the p-doped and n-doped regions inside the waveguide are extremely crucial for the device performance, the device can easily become failure if a different implant energy or dosage has been employed. On the other hand, the waveguide dimension has been hugely changed by 60 nm thinner. Even if we used a 15 nm thicker sacrificial oxide in the following process, there can be around 45 nm difference of the p-n junction in the waveguide with our design. By considering our depletion width in the p-doped region is only 40 nm or less, the huge different waveguide dimension can lead to totally different device response.

We describe in following the preliminary experimental results of the vertical junction p-n diode embedded in 220 nm high waveguide device that fabricated in a CMOS compatible foundry service by IME, Singapore [69]. The device is fabricated by a fully-CMOS compatible-process with similar process described in section 3.4,

except that all the patterns are defined by the deep-ultraviolet (DUV) photolithography with 248 nm exposure wavelength.

Figure 3.5.7 shows the measured transmission spectra of the diode-embedded AMZI with the 2 mm phase shifter under various reverse-bias DC voltages from 0 V to 5 V. The wavelength scan ranged from 1530 nm to 1570 nm. The resolution of the spectra is 0.1 nm. The laser input power is around -2.5 dBm.

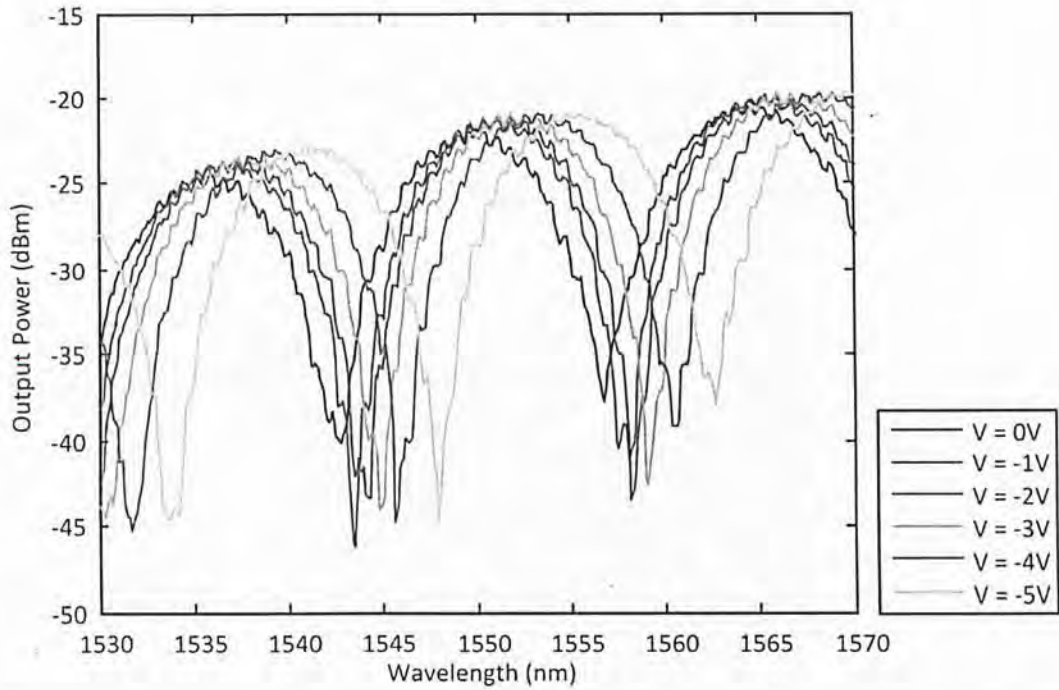


Fig. 3.5.7 Measured transmission spectra of the fabricated depletion-based modulator embedded with a  $p^+ - p - n - n^+$  diode in waveguide with height of 220 nm under various reverse-bias DC voltages.

From figure 3.5.7, the maximum output power from the device under test is around -20 dBm. With around 10 dB coupling loss and around 1 dB loss in the setup, the insertion loss of the device is around 11.5 dB. The measured FSR of the AMZI is around 15 nm, which matches with our design 40  $\mu\text{m}$  arm difference between the

arms in the AMZI. At reverse-bias voltage of 5 V, the null point in the transmission spectrum is shifted to the longer wavelength of around 5.9 nm, which corresponds to an effective refractive index change of around  $3 \times 10^{-4}$ . Thus the  $V_{\pi}L$  of this device is around 1.3 Vcm. At wavelength of 1556.8 nm, the DC extinction ratio is around 16 dB at reverse-bias voltage of 5 V. The output power is -21.5 dBm, correspond to an insertion loss of around 13 dB. The experiments on high-speed electrical response of the device are still undergoing.



### 3.6 T-Rail Travelling-Wave Electrodes

In this section, we present the design principle and proposed a T-rail capacitive-loaded travelling-wave electrode (TWE) [61] in order to achieve high-speed modulation and high-extinction-ratio simultaneously.

Just like in the diode designs, there are also three major requirements in the design of TWE. They are all aimed at increase the electrical bandwidth (thus speed) of the optical modulator. The requirements are: (1) impedance matching (2) microwave velocity and optical group velocity matching and (3) RF loss reduction.

#### ***3.6.1 The Limiting Factors to the Speed of Depletion-based Modulators***

There are several factors limiting the electrical bandwidth (speed) of the depletion based modulator. The carrier depletion based modulator has carrier transit time less than 10 picoseconds [27], which correspond to an electrical bandwidth of around 100 GHz. The electrical bandwidth is further limited by the RC time constant by the capacitance and series resistance in the p-n diode. Depending on the p-n diode design, the magnitudes of the diode capacitance can range from 0.2 fF/ $\mu\text{m}$  to 0.8 fF/ $\mu\text{m}$  [31, 35]. The series resistance of the diode can be around 5 k $\Omega$   $\mu\text{m}$  [35], resulting in a device RC bandwidth of around 30 GHz. However, in the RF system, the power supply and load also have impedance of 50  $\Omega$ . We assume a 3mm long phase shifter used in the depletion-based modulator, the diode capacitances thus translate to a 3dB RC bandwidth of around few GHz. In microwave system, the loss of microwave waveguide (electrode) would attenuate the microwave drive signals, thus results in a decrease of optical modulation depth, which becomes another bandwidth limitation. The velocities mismatch between microwave and optical wave also results in bandwidth limitation. In the case of silicon modulators, the group index

$n_g$  is around 4 in silicon waveguides while the microwave index  $n_\mu$  (describe the velocity of microwave signal as  $\text{velocity} = c/n_\mu$ ) is around 2.5 on a silicon substrate [63]. Even in a lossless transmission line, the large difference between  $n_\mu$  and  $n_g$  limit the 3dB bandwidth to 17 GHz with a 5 mm long modulator [62]. From the above analysis, the primary limiting factor in the depletion-based modulator is the RC limit in the RF system. The secondary limiting factor is the microwave loss, the velocities mismatch and the device RC limit. The carrier transit time is the fundamental electrical bandwidth limit of the depletion-based modulator. In addition, the photon cavity lifetime limits the bandwidth to around few tens of GHz in resonator-based modulators.

Figure 3.6.1 shows the schematic of the limiting factors on the speed of depletion-based modulators.

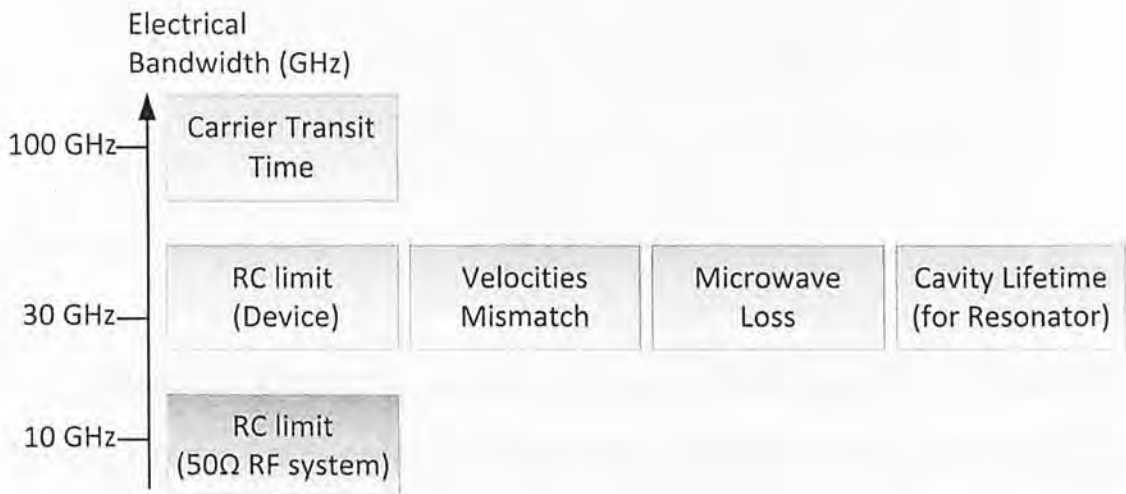


Fig. 3.6.1 Schematic of the limiting factors on the speed of depletion-based modulators.

To reduce capacitance, it is possible to use shorter phase shifter but this will be at the cost of decreasing the modulation depth (in the MZI based modulator). Another option is using resonator-based optical structure such as microring resonator

[25]. The resonators have typical required phase shifter length of less than  $100\ \mu\text{m}$ , and thus the speed is no longer limited by the RC time constant (but may be limited by the photon cavity lifetime in the resonator). The disadvantage of using a resonator structure is the narrow optical bandwidth of around  $0.1\ \text{nm}$  [25].

Because the RC limit is the major limiting factor of the speed (and extinction ratio) of the depletion-based modulator, we then employ a travelling-wave electrode structure to overcome this limit. Our design method is based on basic microwave circuit theory. However, the calculated results from such a method have good agreement with the testing and simulation results used by commercial software [62].

### 3.6.2 The Design Principle of T-Rail Travelling-Wave Electrodes

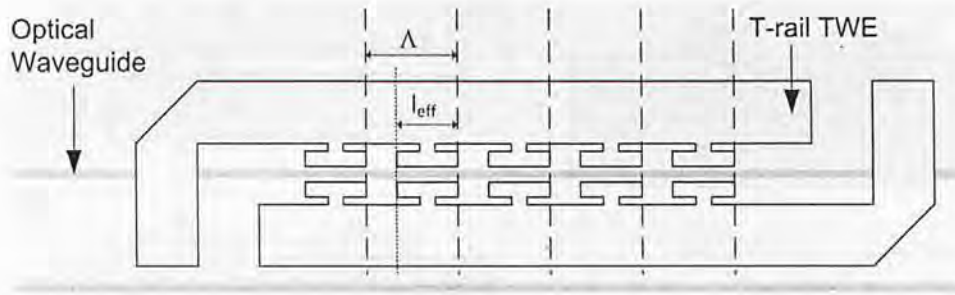


Fig. 3.6.2. Top-view schematic of the T-rail TWE design

Figure 3.6.2 shows the top-view schematic of the T-rail TWE. A T-rail TWE is formed by duplicating a segment of unloaded coplanar strip (CPS) with length of  $\Lambda$  loaded with lumped capacitor with length of  $l_{\text{eff}}$ . In the depletion-based modulator the lumped capacitor is mainly contributed by the waveguide-embedded vertical-junction p-n diode. The capacitive-loaded electrode scheme is used to cancel out the RC limit of the modulator. The dimensions of the T-rail waveguide determine the microwave velocity and the characteristic impedance, and thus govern the highest bandwidth of



the modulator. We discuss our design principle of the T-rail TWE in order to determine the dimensions of the T-rail TWE in this section.

Figure 3.6.3 (a) shows the top-view schematic of the unloaded CPS. Figure 3.6.3 (b) shows the cross-sectional schematic of the unloaded CPS. Figure 3.6.3 (c) shows the cross-sectional schematic of the E-field distribution of the CPS [67]. Figure 3.6.3 (d) shows the equivalent transmission line circuit model of the unloaded CPS. Each section of transmission line with length of  $\Lambda$  can be modeled as a lumped-element circuit, where  $R_0$  is the series resistance per unit length,  $L_0$  is the series inductance per unit length,  $G_0$  is the shunt conductance per unit length,  $C_0$  is the shunt capacitance per unit length.

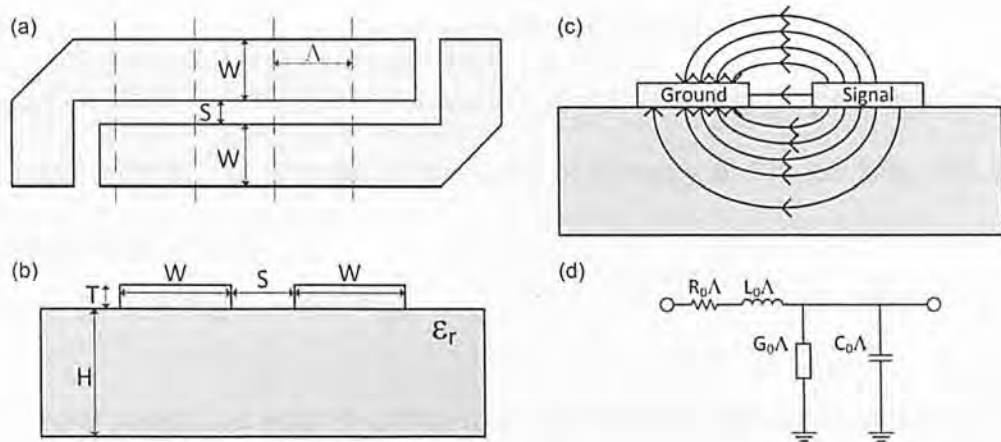


Fig. 3.6.3. (a) Top-view schematic of the unloaded CPS.  $W$  is the width of the strips,  $S$  is the gap separation between the two strips. (b) Cross-sectional schematic of the unloaded CPS.  $H$  is the height of the substrate,  $T$  is the height of metal strips,  $\epsilon_r$  is the relative permittivity of the substrate. (c) Cross-sectional schematic of the E-field distribution of the CPS. (d) Equivalent transmission line circuit model of the unloaded CPS.

In the microwave transmission line design, we can control the characteristic impedance of the CPS by controlling the width of the metal strip and the space between the two metal strips. Figure 3.6.4 shows the calculated characteristic



impedance of the CPS as a function of the gap separation by the empirical relationship [63]. We assume a 525  $\mu\text{m}$  thick substrate with  $\epsilon_r$  of 11.9 (silicon). We set the strip width to be 120  $\mu\text{m}$ .

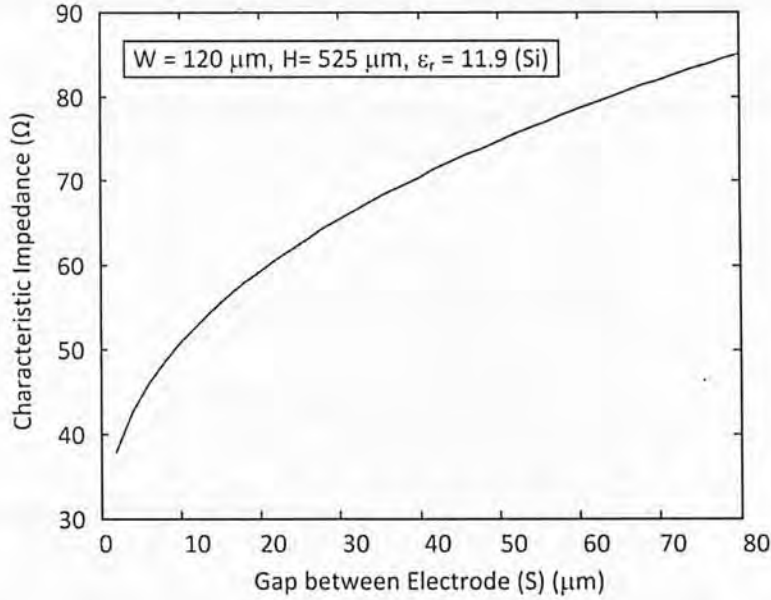


Fig. 3.6.4 Calculated characteristic impedance as a function of the gap separation of CPS by the empirical relation. The substrate is assumed to be silicon with 525  $\mu\text{m}$  thick. The strip widths are set to be 120  $\mu\text{m}$ .

In our design, we simplified the circuit model of the transmission line as a LC line. The hypothesis of the microwave transmission line into a simple LC line is correct in most cases as a typical microwave transmission line has low series resistance of the electrode and low shunt conductance between the ground and signal conductor. From the microwave circuit theory, the characteristic impedance  $Z_0$  of the circuit can be expressed as:

$$Z_0 = \sqrt{\frac{(R_0 + j\omega L_0)}{(G_0 + j\omega C_0)}} \approx \sqrt{\frac{L_0}{C_0}} \quad (3.6.1)$$

where  $\omega$  is the angular frequency.

The propagation constant  $\gamma$  can be expressed as:

$$\gamma = \sqrt{(R_0 + j\omega L_0)(G_0 + j\omega C_0)} = \alpha + j\beta \approx j\omega\sqrt{L_0 C_0} \quad (3.6.2)$$

where  $\alpha$  is microwave attenuation constant,  $\beta$  is the microwave propagation constant.

Hence, the microwave phase velocity  $V_{phase}$  and microwave index  $n_\mu$  can be derived as:

$$V_{phase} = \frac{\omega}{\beta} = \frac{\omega}{\omega\sqrt{L_0 C_0}} = \frac{1}{\sqrt{L_0 C_0}} \quad (3.6.3)$$

$$n_\mu = \frac{c}{V_{phase}} = c\sqrt{L_0 C_0} \quad (3.6.4)$$

where  $c$  is the speed of light in free space.

We can obtain various characteristic impedance  $Z_0$  by modifying the width and gap spacing of CPS. However, we are not able to change the microwave index of the CPS waveguide by modifying the design of CPS (the product of  $L_0$  and  $C_0$  is nearly constant). The approximate microwave index of CPS waveguide is  $\sqrt{(1 + \epsilon_r)/2}$  and in our design  $\epsilon_r$  is around 11.9 (silicon), thus the microwave index is around 2.5. The analysis suggests that an unloaded CPS can be designed to obtain impedance matching of the RF system, but it cannot provide the function of velocities matching.

If we load the p-n diode along the CPS, an additional shunt capacitance per unit length  $C_L$  is added to the circuit model. The characteristic impedance in the loaded CPS, defined as  $Z_0'$ , can be expressed as:

$$Z_0' = \sqrt{\frac{(R_0 + j\omega L_0)}{(G_0 + j\omega(C_0 + C_L))}} \approx \sqrt{\frac{L_0}{C_0 + C_L}} \quad (3.6.5)$$

As from equation 3.6.5, the  $Z_0'$  is different from the characteristic impedance of CPS waveguide  $Z_0$ , the additional  $C_L$  thus decreases the impedance of the loaded CPS when the dimensions of the CPS is remain unchanged (e.g. from 80  $\Omega$  to 50  $\Omega$ ). Because of this reason, in order to fulfill the impedance matching condition (50 $\Omega$  in common RF system) the design of the CPS width and gap spacing should have an impedance higher than 50  $\Omega$  (e.g. 80 $\Omega$ ) to achieve a final  $Z_0'$  of 50  $\Omega$ .

With the same approach to derive the microwave index in above for unloaded CPS waveguide, the microwave index for loaded CPS  $n_\mu'$  is expressed as:

$$n_\mu' = c\sqrt{L_0(C_0 + C_L)} \quad (3.6.6)$$

From equation 3.6.6, it is obvious that the microwave index of the loaded CPS can be increased by adding a loaded shunt capacitance. As mentioned before, the  $C_0$  and  $L_0$  are determined by the CPS dimension, and if we loaded the p-n diode into the CPS as a loaded CPS, the value of  $C_L$  is similar to the value of capacitance per length  $C_{pn}$  of p-n diode. In our vertical junction p-n diode design, the value of  $C_{pn}$  in our calculation is around 0.35 to 0.5 fF/ $\mu\text{m}$  (350 to 500 pF/m) upon reverse bias of 2.5 V, depending on the variations of the diode fabrication such as doping window, implant energy and dosage. In order to engineer the value  $C_L$  to achieve both velocities and impedance matching, the T-rail TWE design is thus used. By changing the length of  $l_{eff}$  of T-rail TWE, the value of  $C_L$  can also be modified as:

$$C_L = (C_{pn} \times l_{eff})/\Lambda \quad (3.6.7)$$

The parasitic capacitance, which may come from the geometry of the electrode, also affect the magnitude of  $C_L$ , however, we do not have accurate method to



determine it in the design stage as it is normally evaluated by the device testing after the fabrication.

By equations 3.6.1 to 3.6.7, we can calculate the desired dimensions of the T-rail TWE to achieve the impedance and velocities matching. First, multiply equation 3.6.1 and equation 3.6.4, and multiply equation 3.6.5 and equation 3.6.6, we can express the value of  $L_0$  into  $Z_0$ ,  $n_\mu$ ,  $Z_0'$ ,  $n_\mu'$  and  $c$  as:

$$L_0 = \frac{Z_0 n_\mu}{c} = \frac{Z_0' n_\mu'}{c} \quad (3.6.8)$$

Equation 3.6.8 provides the relation to design the dimensions of the unloaded CPS in T-rail TWE with  $Z_0$  to achieve the final impedance of the T-rail TWE of  $50\Omega$ . As our design targeted of  $n_\mu'$  is 4.0, with  $n_\mu$  is 2.5,  $Z_0'$  should be  $50\Omega$  and  $Z_0$  of the CPS is around  $80\Omega$ . From figure 3.6.4, this corresponds to a CPS width  $W$  of  $120\mu\text{m}$ , gap  $S$  of  $60\mu\text{m}$ . Those values have been employ in our final design. Equation 3.6.8 also gives the estimated inductance per unit length  $L_0$  of the electrode. The value of  $L_0$  is around  $667\text{ nH/m}$ .

Then by dividing equation 3.6.4 by equation 3.6.1, also by  $Z_0 = Z_0' n_\mu' / n_\mu$ , we can express the value of  $C_0$  into  $Z_0$ ,  $n_\mu$ , and  $c$  as:

$$C_0 = \frac{n_\mu}{c Z_0} = \frac{n_\mu^2}{c Z_0' n_\mu'} \quad (3.6.9)$$

With  $n_\mu$  is 2.5,  $Z_0$  is  $80\Omega$ , the capacitance per length of the electrode  $C_0$  is  $104\text{ pF/m}$ .

Similarly, we divide the equation 3.6.6 by equation 3.6.5 and combine with equation 3.6.8 as:

$$C_0 + C_L = \frac{n_\mu'}{c Z_0'} \quad (3.6.10)$$



$$C_L = \frac{(n'_\mu)^2}{c Z'_0 n'_\mu} - C_0 = \frac{(n'_\mu)^2 - n_\mu^2}{c Z'_0 n'_\mu} \quad (3.6.11)$$

With  $n_\mu$  is 2.5,  $Z_0$  is  $80 \Omega$  and  $C_0$  is 104 pF/m, the value of  $C_L$  should be 162.5 pF/m. As we set the period of each T-rail session  $\Lambda$  to be  $500 \mu\text{m}$ , the corresponding  $L_0\Lambda$  is 333 pH,  $C_0\Lambda$  is 52 fF and  $C_L\Lambda$  is 81 fF. By equation 3.6.7 and the values of  $C_{pn}$  are from 350 pF/m to 500 pF/m, we find the corresponding effective lengths  $l_{\text{eff}}$  are from  $230 \mu\text{m}$  to  $160 \mu\text{m}$ . In addition, as in the modulator designs, the T-rail TWE is actually located on a stack of  $\text{SiO}_2$  and Si layer, we than assume that the microwave index of the CPS is slightly below 2.5. The changes of microwave index would change the corresponding values used in the equations above. We then re-calculate the dimensions of the T-rail TWE for every cases. We find that the width of strips  $W$  and gap  $S$  are nearly constant for a range of microwave index. The only value needs to be modified is the  $l_{\text{eff}}$ . Figure 3.6.5 shows the required  $l_{\text{eff}}$  to achieve both velocity and impedance matching as a function of microwave index with various diode capacitance.

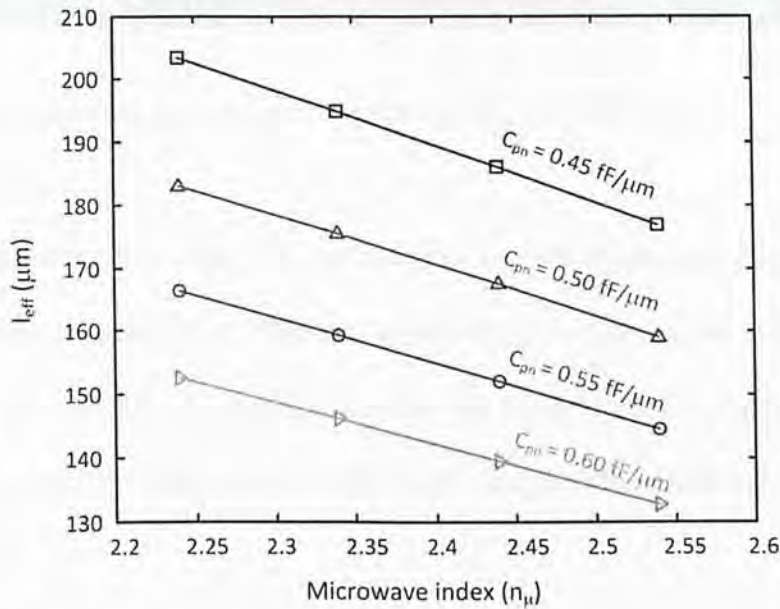


Fig. 3.6.5 Calculated required  $l_{\text{eff}}$  to achieve group velocity and impedance matching as a function of microwave index with various diode capacitance.

In our final designs, the width of strips  $W$  is set to be  $120\text{ }\mu\text{m}$ , gap spacing between strips  $S$  is set to be  $60\text{ }\mu\text{m}$  for all the designs. The period  $\Lambda$  is set to be  $500\text{ }\mu\text{m}$ . The values of  $l_{\text{eff}}$  range from  $100\text{ }\mu\text{m}$  to  $350\text{ }\mu\text{m}$ . The values are selected to compensate the various values of  $C_{\text{pn}}$  from simulations and parasitic.

### 3.6.3 The Fabricated Devices

The T-rail TWE designs are fabricated on the same SOI wafer with the processes described in section 3.4.

Figure 3.6.6 shows the top-view microscope image of the fabricated T-rail TWE on the SOI wafer.

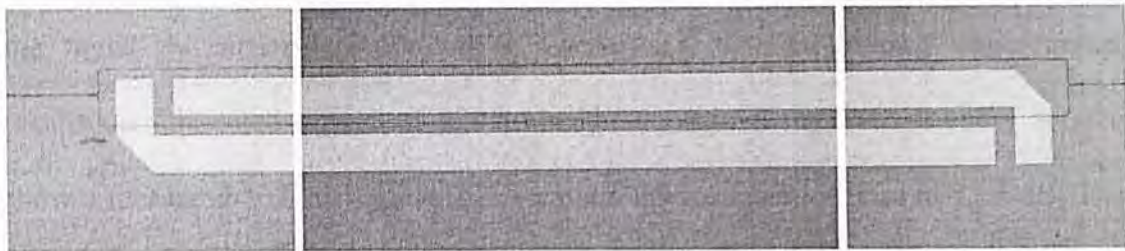


Fig. 3.6.6 Top-view microscope image of the fabricated T-rail TWE on SOI.

As discussed in section 3.5, our fabricated vertical-junction diode embedded depletion-based modulators are unable to provide response on carrier depletion-based modulation. We are still waiting for another set of devices fabricated by oversea foundry to evaluate the effect of our T-rail TWE design to the electrical bandwidth of the modulator.



### 3.7 Summary

In summary, we proposed and fabricated a vertical-junction p-n diode to achieve high modulation efficiency, low insertion loss and high fabrication tolerance depletion-based modulator. Our modeling results show a highly efficient diode design with  $V_{\pi}L$  of 0.9 Vcm in 220nm-height waveguide and 1.4 Vcm in 340nm-height waveguide. The device RC bandwidth of the modulator is over 50 GHz. The RC bandwidth of the modulator in a 50  $\Omega$  RF system is around 4 GHz. We fabricated the device of 340nm-height waveguide by mix-and-match process of EBL and i-line photolithography. The fabricated device shows good electrical response for the p-n diode with low turn-on voltage and low turn-on (contact) resistance. The devices are capable to modulate the signal by carrier-injection under forward-bias. However, due to the fabrication errors during the processes, the devices are not capable to modulate the signal by carrier-depletion under reverse-bias. The preliminary experimental results on fabricated device of 220nm-height waveguide by IME foundry service show a measured  $V_{\pi}L$  as high as 1.3 Vcm and device insertion loss of 11.5 dB. The DC extinction ratio is 16 dB at reverse-bias voltage of 5 V. The state-of-the-art fabrication environment would help realize our proposed design to demonstrate a highly efficient, low-loss and high-fabrication tolerance silicon-depletion based modulator. We also proposed the design of a T-rail travelling wave electrode to achieve the impedance-matching and velocities-matching. The travelling-wave electrode hence can simultaneously provide high-speed modulation and large-extinction-ratio.

## Chapter 4: Conclusion and Future Work

### 4.1 Conclusion

In this thesis, we first investigated the use of silicon-based modulators in analog optical links. We theoretically analyze the linearity of silicon depletion-based modulators and experimentally demonstrated a SSB-ROF signal generated by silicon injection-based microring modulators. Our work on linearity and ROF transmission suggested that silicon-based modulators have good potential to be used in analog optical links. We also proposed the design of a vertical-junction p-n diode for the silicon depletion based modulator. The new diode design has advantages of high efficiency, high fabrication tolerance and lower loss. In order to overcome the RC time limit, we designed a T-rail travelling-wave electrode (TWE) for the depletion-based modulator. The TWE can also achieve the impedance and velocities matching to allow higher electrical bandwidth of the modulator. Our work on vertical-junction diode design and TWE for depletion-based modulators suggested that the performance of silicon depletion-based modulators can be further improved. This is important for the future optical communications and on-chip interconnect applications.

#### ***4.1.1 Use of Silicon-based Modulators in Radio-over-fiber Optical Links***

We theoretically studied the linearity of silicon depletion-based modulators and experimentally demonstrated a radio-over-fiber (ROF) signal transmission in analog optical links by the use of silicon injection-based microring modulators. We found that the linearity of silicon depletion-based modulators is higher than LEO-based modulator in MZI structure. The linearity is improved by the nonlinear response of refractive index change of free-carrier effect. We also showed that the linearity of silicon depletion-based modulators can be further improved by optimizing



the embedded diode structure with a larger intrinsic region. The largest improvement in SFDR was 5.9 dB in a MZI structure. On the experimental side, we experimentally demonstrated the generation of single-side-band (SSB) ROF signals by a silicon injection-based ring modulator. We also characterized the performance of microring modulated signal transmission with up to 100 km long single-mode fiber. The analytical and experimental results presented in this thesis shows that silicon based modulators have good potential to be used in analog optical links. As silicon depletion-based MZI modulators provide better linearity than LEO-based MZI modulator, silicon microring modulators provide an effective way to generate a SSB-ROF signal through its narrow-band transmission characteristic.

#### ***4.1.2 Novel Diode Structures and T-Rail Travelling-Wave Electrodes to Enhance the Performance of Depletion-based Modulators***

We designed, proposed and fabricated a vertical-junction p-n diode to achieve high modulation efficiency, low insertion loss and high fabrication tolerance in a depletion-based modulator. Our modeling results showed a highly efficient diode design with  $V_{\pi}L$  of 0.9 Vcm in 220nm-height waveguide and 1.4 Vcm in 340nm-height waveguide. The device RC bandwidth of the modulator was over 50 GHz. The RC bandwidth of the modulator in 50  $\Omega$  RF system was around 4 GHz. In order to experimentally demonstrate our designs, we fabricated the device by mix-and-match process of EBL and i-line photolithography in MNF/CUHK and NFF/HKUST. The fabricated device showed good electrical response for the p-n diode with low turn-on voltage and low turn-on resistance. The preliminary experimental results suggested that the devices were capable to modulate the signal by carrier injection under forward bias. However, due to fabrication errors and facilities limitation during our

processes, the devices were not capable to modulate the signal by carrier depletion under reverse bias. The preliminary experimental results on fabricated device of 220nm-height waveguide by IME foundry service show a measured  $V_{\pi}L$  as high as 1.3 Vcm and device insertion loss of 11.5 dB. The DC extinction ratio is 16 dB at reverse-bias voltage of 5 V. The state-of-the-art fabrication facilities would help realize our proposed design to demonstrate a highly efficient, low loss and high fabrication tolerance silicon depletion-based modulator. We also designed, proposed and fabricated a T-rail TWE to achieve the impedance matching and velocities matching. We presented the detailed design principles of the TWE based on circuit theory. The travelling-wave electrode was aimed to simultaneously provide high speed modulation and large extinction ratio.

## 4.2 Future Work

On the applications of silicon modulators in analog optical links, our analysis on the linearity of depletion-based modulators is mainly on numerical modeling due to unavailability of working device. Thus, we should test the linearity of a fabricated working depletion-based modulator to further compare with our results. As in our latest fabrication layout, we also designed minor variations on the diode structures. We can then compare the linearity on various diode structures to compare with our simulation results. On the other side, we can also perform more experiments of the system-level ROF signal transmission by using existing or fabricated silicon modulators.

On the further optimization of efficiency by the vertical-junction diode design, we can use even smaller waveguide dimensions. In our pervious works, since by the consideration of easy fabrication of SOI with top silicon thickness of 340 nm and 220 nm, we limited to design our diodes in a waveguide dimension of 340 nm and 220 nm height with 500 nm width. However, with our design principle described in chapter 3, the depletion region width is around 130 nm at doping concentrations of around  $1 \times 10^{18} / \text{cm}^3$ . To increase the overlap between the optical mode profile and depletion region width, we can use a waveguide with height of 150 nm or less. A systematic analysis on the relation between the waveguide height and modulation efficiency should be studied to find out an optimum height as the evanescent field also increase as height decreases.

On the work of depletion-based modulators, we can employ various novel photonic structures to enhance the performance of modulators. Our previous designs mainly focus on the MZI structures, we can employ either resonator-based structures

or photonic-crystal-based structures to improve the required footprint, energy per bit and drive voltage of the modulator. The footprint, energy and drive voltage are crucial for on-chip interconnect systems. In the energy performance of our proposed design, a systematic study on the relation between increased capacitance and energy required by our proposed vertical-junction p-n diode is needed. Furthermore, most of the current silicon modulators are based on amplitude modulation scheme, we can design a modulator to be used as a phase modulator to modulate DPSK or DQPSK signals.

On the travelling-wave-electrode, we can further optimize the design parameters once the devices have been tested. As discussed in the previous section, as parasitic capacitances are hard to be predicted in the design stage, we should measure the parasitic components of the fabricated devices to further improve the designs of TWE. At the optimization stage, the microwave commercial design software, either ADS or HFSS, should be used in the modeling. On the other hand, our previous electrode design did not provide the function to minimize the microwave loss of electrode. In the further optimization stage, we can employ similar methods as in InP-based modulators to use a thicker low-loss substrate below the metal electrodes. A thicker oxide may be a good option by considering the requirement of CMOS-compatibility.



## Appendix-A List of Symbols

$A$	amplitude
$c$	speed of light in free space
$C_0$	shunt capacitance per unit length (of electrode)
$C_L$	shunt capacitance per unit length (of load)
$e$	electron charge
$E$	electric field
$G_0$	shunt conductance per unit length (of electrode)
$L_0$	series inductance per unit length (of electrode)
$n_g$	group index (of optical wave)
$n_\mu$	microwave index
$n_\mu'$	microwave index (of loaded electrode)
$N_A$	p doping (acceptor) concentration
$N_D$	n doping (donator) concentration
$Q$	quality factor
$R_0$	series resistance per unit length (of electrode)
$V_{bi}$	built-in voltage
$V_{app}$	applied reverse bias
$W_D$	depletion width
$Z_0$	characteristic impedance (of electrode)
$Z_0'$	characteristic impedance (of loaded electrode)
$\Delta n$	refractive index changes
$\Delta n_e$	changes of refractive index resulting from electron concentration change
$\Delta n_h$	changes of refractive index resulting from hole concentration change
$\Delta N_e$	free electron concentration change
$\Delta N_h$	free hole concentration change
$\Delta \alpha$	absorption coefficient changes

$\Delta\alpha_e$	changes of absorption coefficient resulting from electron conc. change
$\Delta\alpha_h$	changes of absorption coefficient resulting from hole conc. change
$\beta$	propagation constant
$\epsilon_o$	permittivity of free space
$\epsilon_r$	relative permittivity
$\lambda$	wavelength
$\tau$	coupling coefficient
$\omega$	angular frequency

## Appendix-B List of Abbreviations

2RAMZI	Two ring assisted Mach Zehnder interferometer
3 <sup>rd</sup> IMD	3 <sup>rd</sup> order intermodulation
AM	Amplitude modulation
AMZI	Asymmetric Mach Zehnder interferometer
ASK	Amplitude shift keying
AWG	Arrayed waveguide grating
BER	Bit error ratio
BOE	Buffered oxide etchant
BOX	Buried oxide
BPF	Band pass filter
CATV	Cable television
CCD	Charged coupled device
CMOS	Complementary metal-oxide-semiconductor
CPS	Coplanar strip
DBR	Distributed Bragg reflector
DC	Direct-current
DPSK	Differential phase shift keying
DRIE	Deep-reactive-ion-etching
DFB	Distributed feedback
DWDM	Dense wavelength division multiplexing
EAM	Electroabsorption modulator
EBL	Electronic beam lithography
EDFA	Erbium doped fiber amplifier
ER	Extinction ratio
FEM	Finite element method
FM	Frequency modulation

FSK	Frequency shift keying
FSR	Free spectral range
FWHM	Full width at half maximum
GS	Ground-signal
GSG	Ground-signal-ground
IC	Integrated circuit
ICP	Inductively-coupled-plasma
LEO	Linear electro optic
LR	Long-reach
LTO	Low temperature oxide
MZI	Mach Zehnder interferometer
MQW	Multiple quantum well
NRZ	Non-return-zero
OCS	Optical carrier suppress
OEIC	Optoelectronic integrated circuit
OOK	On off keying
OSA	Optical spectrum analyzer
OSNR	Optical signal to noise ratio
PC	Polarization controller
PIC	Photonic integrated circuit
PM	Phase modulation
PR	Photo resist
PRBS	Pseudorandom bit sequence
PSK	Phase shift keying
QCSE	Quantum-confined Stark effect
RAMZI	Ring assisted Mach Zehnder interferometer
RAU	Remote antenna units
RC	Resistance-capacitance



RF	Radio-frequency
RIE	Reactive-ion-etching
ROF	Radio-over-fiber
SEM	Scanning electronic microscope
SFDR	Spurious free dynamic range
SMF	Single mode fiber
SNR	Signal to noise ratio
SOA	Semiconductor optical amplifier
SOI	Silicon on insulator
SSB	Single-sideband
TE	Transverse-electric
TWE	Travelling wave electrode
VCSEL	Vertical cavity surface emitting laser
WDM	Wavelength division multiplexing

## Appendix-C Principles of Various Optical Structures of Modulators

Refer to table 1.5, there are two type of optical structures have been employed in the optical modulator: (1) Mach-Zehnder interferometer (MZI) and (2) optical resonator. The schematics of MZI and optical resonator are depicted in figure C.1.

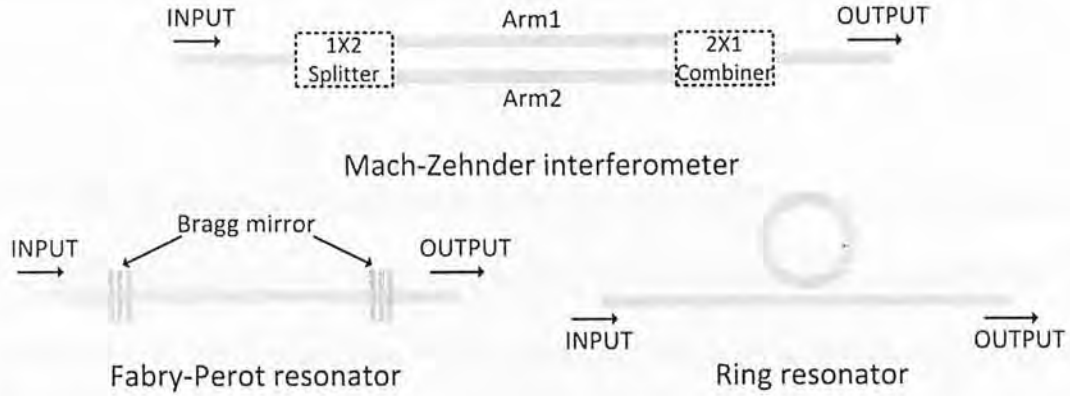


Fig. C.1 Schematics of Mach-Zehnder interferometer (MZI), Fabry-Perot (FP) resonator and ring resonator.

The first type of widely used optical structure in optical modulator is MZI. A MZI based modulator uses an interferometer structure to convert the phase modulation of optical wave into intensity modulation. In the MZI structure, input optical wave split equally into isolated 2 paths by a beam splitter (e.g. 1X2 MMI or Y-branch), then pass through different arm finally combine together by a beam combiner (2X1 MMI or Y-branch). At the output combiner, interference occurs and the output intensity is determined by the phase difference between two arms.

The phase of the optical wave for each arm at the combiner is calculated by:

$$\phi = \frac{2\pi (n_{eff} + \Delta n) L}{\lambda} \quad (C.1)$$

where  $\phi$  is the output phase of the optical wave at the combiner,  $L$  is length of the arm,  $\lambda$  is the wavelength of the optical wave,  $n_{eff}$  is the effective index of the waveguide,  $\Delta n$  is the changed of refractive index by modulation.

Assume only arm1 has been modulated, and the length of two arms are same. Then the different of optical phase between two arms at the combiner becomes:

$$\Delta\phi = \frac{2\pi (\Delta n) L}{\lambda} \quad (C.2)$$

By equation C.2, if  $\Delta\phi$  is  $\pi$  or  $-\pi$ , the optical waves at two arms are anti-phase, destructive interference occurs, corresponding to the off-state of modulator (0-level). And if  $\Delta\phi$  is 0, the optical waves at two arms are in-phase, constructive interference occurs, corresponding to the on-state of modulator (1-level). This is the basic operation principle of the MZI based modulator.

Of course, one can also use ‘push-pull’ operation, which means simultaneously drive the arm1 and arm2, with one arm has positive  $\Delta n$  and another one has negative  $\Delta n$ , in order to achieve a total phase difference between two arm  $\Delta\phi$  is between 0 to  $\pi$ . The push-pull operation has advantage of lower drive voltage, shorter required arm length and lower chirp compare with single arm drive. But it requires more complicated driving circuits or electrode design.

The second type of widely used optical structure in optical modulator is resonator based structure. In resonator based structure, input optical wave is coupled to a resonator, which commonly can be Fabry-Perot or ring resonator. A waveguide based Fabry-Perot resonator typically consists of two parallel reflectors facing each other (e.g. Bragg mirror). A waveguide based ring resonator typically consists of a waveguide coupled to a closed loop waveguide in the shape of ring or racetrack. The

resonators behave as an interferometer and will be resonant for optical wave whose phase after each full trip around the resonator cavity is in-phase with the input light and constructive interference occur.

Take an example for ring resonator, the resonant wavelength  $\lambda_r$  is determined by the geometry of the resonator and effective refractive index as:

$$\lambda_r = \frac{2\pi R n_{eff}}{m} \quad (C.3)$$

where  $R$  is the ring radius with circular ring, and  $m$  is an integer.

From equation C.3, one can simply modulated the refractive  $n_{eff}$  in the resonator to change the resonant wavelength  $\lambda_r$  thus the new resonant wavelength  $\lambda_{r2}$  can shift to either longer (if  $n_{eff}$  is increase) or shorter (if  $n_{eff}$  is decrease) wavelength.

The resonant wavelength  $\lambda_{r2}$  under modulation is:

$$\lambda_{r2} = \frac{2\pi R (n_{eff} + \Delta n)}{m} \quad (C.4)$$

where  $\Delta n$  is the changed of refractive index by modulation.

When the input optical carrier is initially probed at wavelength  $\lambda_r$  (or  $\lambda_{r2}$ ), the intensity modulation of signal is achieved. The operation schematics of the resonator based modulators are depicted in figure C.2.



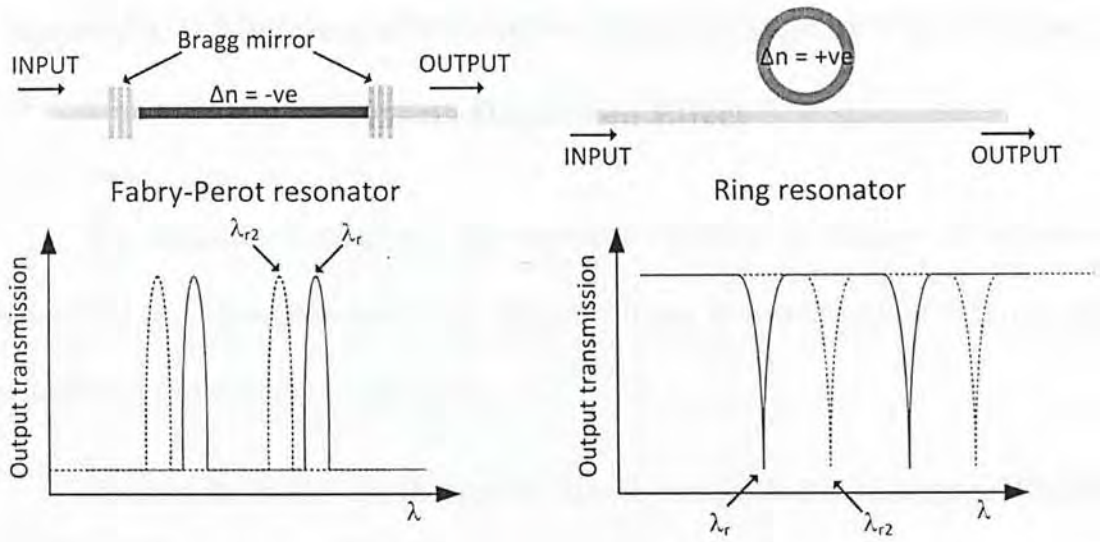


Fig. C.2 Schematics of the operation principle of resonator based modulators. In the Fabry-Perot resonator, refractive index inside the resonant cavity has been decrease, leads to a blue shift of resonance spectrum. In the ring resonator, refractive index inside the ring cavity has been increase, leads to a red shift of resonance spectrum.  $\lambda_r$  is the resonant wavelength,  $\lambda_{r2}$  is the resonant wavelength under modulation.

## Appendix-D Modeling of Refractive Index Change by Free-Carrier

### Plasma Dispersion Effect

We describes in chapter 1 the empirical relations of changes of refractive index ( $\Delta n$ ) and absorption coefficient ( $\Delta\alpha$ ) in silicon at wavelength of 1.55  $\mu\text{m}$  are described by equations 1.4.1 and 1.4.2.

In order the model the changes of reflective index and absorption coefficient induced by free carrier effect, there are two set of data we need to know: (1) the exactly number of free electrons and free holes of silicon under different bias condition and (2) the optical mode field profile.

As the total refractive index changes (and  $\Delta\alpha$ ) are governed by the overlap between the of optical mode and variation of refractive index, equation D.1 gives the value of refractive index change by changing the free carrier densities:

$$\Delta n_{eff} = \frac{\iint_{-x}^x \Delta n(x,y) I(x,y) dx dy}{\iint_{-x}^x I(x,y) dx dy} \quad (D.1)$$

where  $I(x,y)$  is the intensity of the optical mode at  $x$  and  $y$  coordinates,  $\Delta n(x,y)$  is the changes of refractive index at  $x$  and  $y$  coordinates.

Similarly, for the value of absorption coefficient change by changing the free carrier densities is

$$\Delta\alpha = \frac{\iint_{-\infty}^{\infty} \Delta\alpha(x,y) I(x,y) dx dy}{\iint_{-\infty}^{\infty} I(x,y) dx dy} \quad (D.2)$$

where  $\Delta\alpha(x,y)$  is the changes of absorption coefficient at  $x$  and  $y$  coordinates.

The equation D.1 and D.2 show the importance of the mode overlap in silicon modulator design based on carrier effect. We raise two different examples to explain the principle of this equation.

First, assuming that the carrier densities changes are exactly the same in silicon, which means  $\Delta n(x,y) = \text{constant}$  for any  $x$  and  $y$  coordinates in silicon. There are evanescent fields penetrating into the cladding regions. Even in high index contrast silicon waveguide on SOI platform, the confinement factor (describe the portion of optical mode field inside the core material) is only around 0.7. This means that a 30% of optical field is outside the silicon core regions and falls into SiO<sub>2</sub> regions in the SOI case. Certainly this 30% of optical field would not be modulated by the carrier effect in silicon because the field is located in SiO<sub>2</sub> which doesn't behave a carrier effect described in the equation 1.4.1 and 1.4.2. In this example, the  $\Delta n(x,y) = 0$  for  $x$  and  $y$  coordinates located in the silicon dioxide.

The second example is that the carrier densities changes are non-uniform inside the silicon region. This is normally the case in depletion based and accumulation based modulator. For example, carrier depletion based silicon modulators are operated under reverse bias of the pn junction, in a typical modulated voltage of few volts, the depletion width is less than several hundred nanometer. It indicates the carrier densities variations ( $\Delta n$ ) are only exist in a small depletion region. One may has different results if the depletion region is overlap with the core of waveguide or with the edge of waveguide, since the optical mode profile is more intensive in the core rather than the edge. Actually it is the basic idea to design a high efficient depletion type modulator by maximizing the spatial modal overlap between optical field and depletion region.



In our works, the exactly number of free electrons and free holes of silicon under different bias condition is obtained by the semiconductor simulation tools Athena and Atlas provided by SILVACO [51]. Where Athena is used to simulate the semiconductor processes and Atlas is used to simulate the semiconductor characteristics. The optical mode profile is obtained by BeamPROB provided by RSoft [64]. After extracting the 2D array profiles of free carrier distributions and optical mode field in Atlas and BeamPROB, the total refractive index changes (and  $\Delta\alpha$ ) in the silicon waveguide is then calculated by equation D.1 (and equation D.2) in MATLAB [65] by finite element method (FEM). In addition, Atlas also provides the small signal characteristics of the electrical structures such as shunt capacitance, shunt conductance and carrier transit time. Finally, the flow chart of our methodology in simulation the refractive index changes in silicon modulator based on carrier effect is shown in figure D.1.

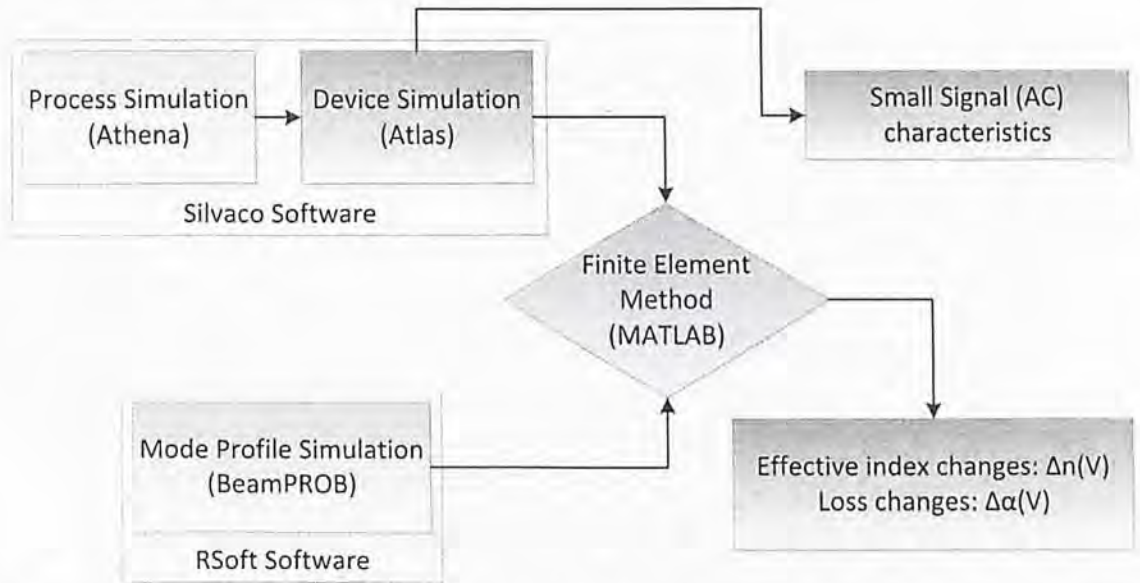


Fig. D.1 Schematic of flow chart of the methodology in simulation the refractive index changes in free carrier effect based silicon modulator. The 2D array profile of free carrier distributions is obtained by Athena and Atlas. The 2D array profile of optical mode field is obtained by BeamPROB. The final refractive index and loss coefficient changes under





## Reference

- [1] L. Pavesi, "Will silicon be the photonic material of the third millennium?" J. Phys.: Condens. Matter, 15, R1169-R1196, 2003
- [2] L. Eldada, "Hybrid integrated photonic components based on a polymer platform", Proceedings of SPIE, Vol. 4997, 88-102, 2003
- [3] R. Nagarajan et al., "InP photonic integrated circuits", IEEE Journal of Selected Topics in Quantum Electronics, Vol. 16, No.5, 2010
- [4] C. Li, "Silicon-based optical microresonator devices: polygonal microdisk channel filters and electro-optic modulators/switches", PhD Thesis, Hong Kong University of Science and Technology, Hong Kong, 2007
- [5] L. Pavesi and D. J. Lockwood, Silicon Photonics, Springer, 2004
- [6] G. T. Reed, Silicon Photonics the state of the art, Wiley, 2009
- [7] D. A. B. Miller, "Rationale and challenges for optical interconnects to electronic chips", Proceedings of IEEE, 99, 728, 2000
- [8] S. E. Miller, "Integrated optics: an Introduction", Bell Sys. Tech. J., Vol. 48, 2059-2069, 1969
- [9] R. A. Soref and J. P. Lorenzo, "Single-crystal silicon – a new material for 1.3 and 1.6  $\mu\text{m}$  integrated-optical components", Electronics Letters, 21, 953-954, 1985
- [10] R. A. Soref and J. P. Lorenzo, "All-silicon active and passive guided-wave components for  $\lambda = 1.3 \mu\text{m}$  and  $1.6 \mu\text{m}$ ", IEEE Journal of Quantum Electronics, QE-22, 873-879, 1986
- [11] R. A. Soref and B. R. Bennett, "Electrooptical Effect in Silicon," IEEE Journal of Quantum Electronics Vol. QE-23, 123-129, 1987
- [12] R. A. Soref, "Silicon- based optoelectronics", Proceedings of the IEEE, Vol. 81, 1687-1706, 1993
- [13] R. A. Soref, "The past, present and future of silicon photonics", IEEE Journal of Selected Topics in Quantum Electronics, Vol. 12, 1678-1687, 2006
- [14] A. W. Fang et al., "Electrically pumped hybrid AlGaInAs-silicon evanescent laser", Optics Express, Vol. 14, No. 20, 9203-9210, 2006
- [15] J. Michel et al., "High-performance Ge-on-Si photodetectors", Nature photonics, Vol.4, 527-534, 2010
- [16] C. Gunn, "CMOS photonics for high-speed interconnects", IEEE Micro, Vol. 26, 58-66, 2006
- [17] European 450mm Equipment & Materials Initiative; <http://www.eemi450.org/>

- [18] A. G. Gnauck and P. J. Winzer, "Optical Phase-Shift-Keyed Transmission", *Journal of Lightwave Technology*, Vol. 23, No. 1, 2005
- [19] M. C. Amann and W. Hofmann, "InP-based long-wavelength VCSELs and VCSEL arrays", *IEEE Journal of Selected Topics in Quantum Electronics*, Vol. 15, No.3, 861-868, 2009
- [20] K. Noguchi et al., "Millimeter-wave Ti:LiNbO<sub>3</sub> optical modulators", *IEEE Journal of Lightwave Technology*, Vol. 16, 615-619, 1998
- [21] A. Yariv and P. Yeh, *Photonics*, Sixth Edition, Oxford, 2007
- [22] D. A. B. Miller et al., "Electric field dependence of optical absorption near the band gap of quantum-well structures", *Physical review*, Vol. B32, No. 2, 1043-1060, 1985
- [23] R. A. Soref and B. R. Bennett, "Kramers-Kronig analysis of E-O switching in silicon," *SPIE integr. Opt. Circuit Eng.*, Vol. 704, 32-37, 1986
- [24] A. Liu et al., "A high-speed silicon optical modulator based on a metal-oxide-semiconductor capacitor", *Nature*, Vol. 427, 615-618, 2004
- [25] Q. Xu et al., "Micrometre-scale silicon electrooptic modulator", *Nature*, Vol. 435, 325-327, 2005
- [26] Q. Xu et al., "12.5 Gbit/s carrier-injection-based silicon micro-ring silicon modulators", *Optics Express*, Vol. 15, No.2, 430-436, 2007
- [27] A. Liu et al., "High-speed optical modulation based on carrier depletion in a silicon waveguide", *Optics Express*, Vol. 15, No. 2, 660-668, 2007
- [28] L. Liao et al., "40 Gbit/s silicon optical modulator for high-speed applications", *Electronics Letters*, Vol. 43, No. 22, 2007
- [29] W. M. Green et al., "Ultra-compact, low RF power, 10 Gb/s silicon Mach-Zehnder modulator", *Optics Express*, Vol. 15, No.25, 17106-17113, 2007
- [30] S. J. Spector et al., "CMOS-compatible dual-output silicon modulator for analog signal processing," *Opt. Express*, Vol. 16, 11027-11031, 2008.
- [31] D. Marris-Morini et al., "Low loss and high speed silicon optical modulator based on a lateral carrier depletion structure," *Opt. Express*, Vol. 16, 334-339, 2008.
- [32] M. R. Watts et al., "Ultralow power silicon microdisk modulators and switches", *Proceeding of 5<sup>th</sup> IEEE International Conference on Group IV Photonics*, 4-6, 2008
- [33] P. Dong et al., "Low  $V_{pp}$ , ultralow-energy, compact, high-speed silicon electro-optic modulator", *Optics Express*, Vol. 17, No. 25, 22484-22490, 2009
- [34] D. D'Andrea, "CMOS photonics today & tomorrow enabling technology", *Optical Fiber Communication Conference Market Watch*, 2009

- [35] M. R. Watts et al., "Low-Voltage, Compact, Depletion-Mode, Silicon Mach-Zehnder Modulator", IEEE Journal of Selected Topics in Quantum Electronics, Vol. 16, No. 1, 159-164, 2010
- [36] Y. Kuo et al., "Strong quantum-confined Stark effect in germanium quantum structures on silicon", Nature, Vol. 437, 1334-1336, 2005
- [37] J. Liu et al., "Waveguide-integrated, ultralow-energy GeSi electro-absorption modulators", Nature Photonics, Vol. 2, 443-437, 2008
- [38] H. W. Chen et al., "Forty Gb/s hybrid silicon Mach-Zehnder modulator with low chirp", Optics Express, Vol. 19, No. 2, 1455-1460, 2011
- [39] Y. Tang et al., "50 Gb/s hybrid silicon travelling-wave electroabsorption modulator", Optics Express, Vol. 19, No. 7, 5811-5816, 2011
- [40] J. E. Roth et al., "Optical modulator on silicon employing germanium quantum wells", Optics Express, Vol. 15, No. 9, 5851-5859, 2007
- [41] C. H. Cox III et al., "Limits on the performance of RF-over-fiber links and their impact on device design", IEEE Transactions on Microwave Theory and Techniques, Vol. 54, No. 2, 2006
- [42] M. K. Jackson et al., "Optically linearized modulators: chirp control for low-distortion control for low-distortion analog transmission", IEEE Journal of Lightwave Technology, Vol. 15, 1538-1646, 1997
- [43] C. Laliew et al., "A linearized optical directional-coupler modulator at 1.3 $\mu$ m", IEEE Journal of Lightwave Technology, Vol. 18, 1233-1249, 2000
- [44] P. L. Liu et al., "In search of a linear electro-optic amplitude modulator", IEEE Photonics Technology Letters, Vol.3, 144-145, 1991
- [45] X. Xie et al., "Linearized Mach-Zehnder Intensity Modulator," IEEE Photonics Technology Letters, Vol. 15, 531-533, 2003
- [46] V. Van et al., "Linearized Microring-Loaded Mach-Zehnder Modulator With RF Gain," IEEE Journal of Lightwave Technology, Vol. 24, 1850-1854, 2006
- [47] ePIXfab; <http://www.epixfab.eu/>
- [48] S. M. Lo et al., "Linearity of Carrier Depletion based Silicon Optical Modulators", in 15<sup>th</sup> OptoElectronics and Communications Conference, 8D1-3, 2010
- [49] F. Vacondio et al., "A Silicon Modulator Enabling RF Over Fiber for 802.11 OFDM Signals", Journal of Selected Topics in Quantum Electronics, Vol. 16, No. 1, pp 141-148, 2010
- [50] C. Sorace et al., "Broadband Linear Silicon Mach-Zehnder Modulators", in Integrated Photonics Research, Silicon and Nanophotonics, IWA4,2010
- [51] Athena, Atlas, SILVACO, Inc.; <http://www.silvaco.com/>



- [52] J. Yu et al., "A novel scheme to generate single-sideband millimeter-wave signals by using low-frequency local oscillator signal," *IEEE Photonic Technology Letter*, Vol. 20, No. 7, 478–480, 2008
- [53] Y. Y. Won et al., "Full colorless WDM- radio over fiber access network supporting simultaneous transmission of millimeter-wave band and baseband gigabit signals by sideband routing", *IEEE Journal Lightwave Technology*, Vol. 28, No. 16, 2213–2218, 2010
- [54] M. K. Hong et al., "Gigabit optical access link for simultaneous wired and wireless signal transmission based on dual parallel injection-locked Fabry–Pérot laser diodes", *IEEE Journal Lightwave Technology*, Vol. 26, No. 15, 2725–2731, 2008
- [55] Soitec, Inc.; <http://www.soitec.com/>
- [56] D. A. B. Miller, "Device Requirements for Optical Interconnects to Silicon Chips", *Proceedings of IEEE*, Vol. 97, No. 7, 1168–1185, 2009
- [57] G. T. Reed et al, "Silicon optical modulators", *Nature Photonics*, Vol. 4, 518–526, 2010
- [58] D. J. Thomson et al., "High speed silicon optical modulator with self aligned fabrication process", *Optics Express*, Vol. 19, No. 19, 19064–19069, 2010
- [59] S. M. Sze, *Physics of Semiconductor Devices*, third edition, Wiley-Interscience, 2007
- [60] Robert Doering and Yoshio Nishi, "Handbook of semiconductor manufacturing technology", CRC Press, 2008
- [61] S. R. Sakamoto et al., "Narrow gap coplanar slow wave electrode for travelling wave electro-optic modulators", *Electronics Letters*, Vol. 31, No. 14, 1183–1185, 1995
- [62] H. T. Chen, "Development of an 80 Gbit/s InP-base mach-zehnder modulator", PhD Thesis, Technischen Universität Berlin, Berlin, 2007
- [63] K. C. Gupta et al., "Microstrip lines and slotlines", Artech, 1979.
- [64] BeamPROB, RSoft Design Group, Inc.; <http://www.rsoftdesign.com/>
- [65] MATLAB, MathWorks, Inc.; <http://www.mathworks.com/>
- [66] L. Zhou et al., "Silicon electro-optic modulators using p-i-n diodes embedded 10 –micron-diameter microdisk resonators", *Optics Express*, Vol. 14, No. 15, 6851–6857, 2006
- [67] H. Tazawa et al., "Bandwidth of linearized ring resonator assisted Mach-Zehnder modulator", *IEEE Photonics Technology Letters*, Vol. 17, No. 9, 1851–1853, 2005
- [68] N. Ashcroft and N. Mermin, *Solid State Physics*, Holt, Rinehart and Winston, Philadelphia, USA, 1976

# Author's Address

- [1] "Long-wavelength external-cavity laser diodes fabricated with a single-substrate design supported by a 100- $\mu\text{m}$  substrate", W. Chow, C. H. Tan, Stanley M. G. Lee, C. J. Chang and H. K. Tsang, *Optics & Photonics*, Vol. 18, No. 12, 4 June 2011.
- [2] "Apodized Waveguide Coupling Schemes for Efficient Coupling to Optical Fibers", X. Chen, C. H. Tan, C. Y. Wang, Stanley M. G. Lee and H. K. Tsang, *IEEE Photonics Technology Letters*, Vol. 24, No. 11, 1 August 2010.

# Conference presentation

- [1] "Efficient External-Cavity Based Laser Diode Modulators", Stanley M. G. Lee, C. H. Tan and H. K. Tsang, *Conference on Lasers and Electro-Optics*, 2011, 16 May 2011, Anaheim, California, USA.
- [2] "Fabrication of Efficient External-Cavity Based Silicon Optical Modulators", Stanley M. G. Lee, C. H. Tan and H. K. Tsang, *13<sup>th</sup> Optoelectronics and Communications Conference*, 3-5 July 2010, Singapore, Japan.
- [3] "Efficient Waveguide Coupling Schemes with Apodized Coupling Through for External-Coupling", X. Chen, C. H. Tan, M. G. Lee, K. Y. Chang and H. K. Tsang, *13<sup>th</sup> Optoelectronics and Communications Conference*, 3-5 April 2010, Anaheim, USA.
- [4] "Millimeter-wave modulator using Four Wave Mixing in Silicon Waveguide", X. Chen, C. H. Tan, Stanley M. G. Lee and H. K. Tsang, *13<sup>th</sup> Optoelectronics and Communications Conference*, 3-5 July 2010, Singapore, Japan.
- [5] "Frequency Combing Use of Power Modulated Signals", C. H. Tan, C. J. Chang, W. Chow, X. Chen, C. Y. Wang, Stanley M. G. Lee and H. K. Tsang, *13<sup>th</sup> Optoelectronics and Communications Conference*, 3-5 July 2010, Singapore, Japan.
- [6] "Efficient Waveguide Coupling to Waveguide Devices", H. K. Tsang, X. Chen, C. H. Tan, C. Y. Wang & M. G. Lee, K. Y. Chang, C. J. Chang, *The International Conference on Nanophotonics 2011*, 20 Jan-3 Nov 2011, Fukuoka, Japan.

## Publication List

### Journal publication:

- [1] 'Long-reach radio-over-fiber signal distribution using single-sideband signal generated by a silicon-modulator', C. W. Chow, C. H. Yeh, Stanley M. G. Lo, C. Li and H. K. Tsang, *Optics Express*, Vol. 19, No. 12, 6 June 2011
- [2] 'Apodized Waveguide Grating Couplers for Efficient Coupling to Optical Fibers', Xia Chen, Chao Li, Christy K. Y. Fung, Stanley M. G. Lo, and Hon K. Tsang, *IEEE Photonics Technology Letters*, Vol. 22, No. 15, 1 August 2010

### Conference publication:

- [1] 'Carrier Depletion Based Linear Silicon Modulator', Stanley M. G. Lo, C. Li and Hon K. Tsang, *Conference on Lasers and Electro-Optics 2011*, 1-6 May 2011, Baltimore, Maryland, USA
- [2] 'Linearity of Carrier Depletion based Silicon Optical Modulators', Stanley M. G. Lo, C. Li, and H. K. Tsang, *15<sup>th</sup> OptoElectronics and Communications Conference*, 5-9 July 2010, Sapporo, Japan
- [3] 'Silicon Waveguide Grating Couplers with Engineered Coupling Strength for Optimized Coupling', X. Chen, C. Li, S. M. G. Lo, K. Y. Fung, and H. K. Tsang, *15<sup>th</sup> European Conference on Integrated Optics*, 7-9 April 2010, Cambridge, UK
- [4] 'Millimeter Wave Generation using Four Wave Mixing in Silicon Waveguide', L. Xu, C. Li, Stanley M. G. Lo and H. K. Tsang, *15<sup>th</sup> OptoElectronics and Communications Conference*, 5-9 July 2010, Sapporo, Japan
- [5] 'Frequency Quadrupling of Phase Modulated Signals', L. Xu, C. Li, C. W. Chow, X. Chen, C. Y. Wong, Stanley M. G. Lo, and H. K. Tsang, *15<sup>th</sup> OptoElectronics and Communications Conference*, 5-9 July 2010, Sapporo, Japan
- [6] (invited) 'Silicon nanophotonic waveguide devices', H. K. Tsang, X. Chen, L. Xu, C. Y. Wong, S. M. G. Lo, K. Y. Fung, C. Li, *The International Conference on Nanophotonics 2010*, 30 May-3 June 2010, Tsukuba, Japan





CUHK Libraries



004864749